UC Irvine

UC Irvine Electronic Theses and Dissertations

Title

Advancement and Application of a Non-Covalent Method for Molecular Attachment to Electrode Surfaces

Permalink

https://escholarship.org/uc/item/7jd41994

Author

Hanna, Caitlin

Publication Date

2019

Peer reviewed|Thesis/dissertation

eScholarship.org Powered by the California Digital Library
University of California

UNIVERSITY OF CALIFORNIA,
IRVINE

Advancement and Application of a Non-Covalent Method for Molecular Attachment to Electrode Surfaces

DISSERTATION

submitted in partial satisfaction of the requirements
for the degree of

DOCTOR OF PHILOSOPHY

in Chemistry

by

Caitlin Marie Hanna

Dissertation Committee:
Associate Professor Jenny Y. Yang, Chair
Associate Professor Shane Ardo
Professor Alan F. Heyduk

2019

Portions of Chapter 2 © 2018 American Chemical Society

Chapter 3 © 2019 American Chemical Society

All other materials © 2019 Caitlin Marie Hanna

DEDICATION

For Mom

TABLE OF CONTENTS

Page

LIST OF FIGURES v

LIST OF TABLES x

LIST OF SCHEMES xi

ACKNOWLEDGMENTS xii

CURRICULUM VITAE xiii

ABSTRACT OF THE DISSERTATION xvi

CHAPTER 1: Introduction 1
1.1. Chemically Modified Electrodes 2
1.2. Molecular Attachment to Electrodes Through Covalent Bonds 4
1.3. Molecular Attachment to Electrodes Through π-π Interactions 6
1.4. Hybrid Approach for Molecular Attachment to Electrodes 7
1.5. Thesis Overview 8
1.6. References 9

CHAPTER 2: Interfacial Electron Transfer of Ferrocene Immobilized onto Indium Tin Oxide Through Covalent and Non-Covalent Interactions 23
2.1 Introduction 24
2.2 Results and Discussion 25
2.2.1 Modification of ITO Surfaces 25
2.2.2 Contact Angle Measurements 26
2.2.3 Fluorescence Spectroscopy 27
2.2.4 X-Ray Photoelectron Spectroscopy (XPS) 28
2.2.5 Cyclic Voltammetry of Modified Electrodes 30
2.2.6 Electron Transfer Kinetics 33
2.2.7 Electrochemical Impedance Spectroscopy 36
2.3 Conclusions 40
2.4 Experimental Details 41
2.5 References 43

CHAPTER 3: Proton-Coupled Electron Transfer at Anthraquinone Modified Indium Tin Oxide Electrodes 50
3.1 Introduction 51
3.2 Results and Discussion 53
3.2.1 Modification of ITO and Spectroscopic Characterization 53
3.2.2 Electrochemical Analysis of Modified ITO 54

3.2.3 Electron Transfer Kinetics of Modified ITO 60
3.2.4 Comparison to a Water Soluble Anthraquinone Derivative 63
3.3 Conclusions 68
3.4 Experimental Details 69
3.5 References 71

CHAPTER 4: Immobilization of a Molecular Water Oxidation Catalyst onto Indium Tin Oxide Through π-π Interactions 80
4.1 Introduction 81
4.2 Results and Discussion 82
4.3 Conclusions 85
4.4 Experimental Details 86
4.5 References 87

CHAPTER 5: Understanding Photoelectrochemical Proton Reduction at Nanoporous Si Electrodes Modified with a Cobald Bis(benzenedithiolate) Catalyst via π-π Interactions 90
5.1 Introduction 91
5.1.1 Surface Modification and Band Bending 91
5.1.2 Intensity-Modulated High-Frequency Resistivity 93
5.1.3 Catalyst Immobilization on Nanoporous Silicon Photoelectrodes 95
5.2 Results and Discussion 97
5.2.1 Preparation and Spectroscopic Characterization of Modified b-Si Surfaces 97
5.2.2 Linear Sweep Voltammetry of Modified Electrodes 103
5.2.3 IMHFR Impedance Spectroscopy of Modified Electrodes 107
5.2.4 Photoelectrochemical Stability of Modified Electrodes 109
5.3 Conclusions 110
5.4 Experimental Details 111
5.5 References 114

APPENDIX A: Attachment of Various Aromatic Molecules to Indium Tin Oxide Through Covalent and Non-Covalent Interactions 122
A.1 Introduction 123
A.2 Results and Discussion 124
A.2.1. Covalent Attachment of PyrPA to Indium Tin Oxide 124
A.2.2 Covalent Attachment of NDI to Indium Tin Oxide 125
A.2.3 Non-Covalent Attachment of PDI to Indium Tin Oxide 127
A.3 Conclusions 130
A.4 Experimental Details 131
A.5 References 136

LIST OF FIGURES

		Page
Figure 1.1	Methods for covalent attachment to silicon electrodes. Adapted from ref. 6 under the terms of the Creative Commons Attribution Non-Commercial No Derivatives License CC BY-NC-ND.	5
Figure 1.2	Methods for covalent attachment to metal oxide electrodes. Reproduced from ref. 9 with permission from John Wiley and Sons, Inc.	6
Figure 2.1	Optical photographs of contacts between a H_2O droplet and (A) freshly cleaned, unmodified ITO and (B) ITO|Pyr.	26
Figure 2.2	Two-photon fluorescence emission spectra of ITO|Pyr (black trace) and ITO|Pyr|Pyrenylferrocene (blue trace).	28
Figure 2.3	XPS survey spectra of ITO, ITO|Pyr, ITO|Pyr|Pyrenylferrocene, and ITO|Vinylferrocene.	29
Figure 2.4	High resolution XPS spectra of the Fe 2p region of ITO, ITO|Pyr, ITO|Pyr|Pyrenylferrocene, and ITO|Vinylferrocene.	29
Figure 2.5	Cyclic voltammetry of ITO|Pyr|Pyrenylferrocene, ITO|Pyr, ITO, and ITO treated with 1-pyrenylferrocene performed in 100 mM KCl at 100 mV/s.	31
Figure 2.6	Variable scan rate cyclic voltammetry (left) and corresponding current density vs scan rate plot (right) of ITO|Pyr|Pyrenylferrocene performed in 100 mM KCl.	32
Figure 2.7	Variable scan rate cyclic voltammetry (left) and corresponding current density vs scan rate plot (right) of ITO|Vinylferrocene performed in 100 mM KCl.	33
Figure 2.8	Trumpet plots for ITO|Pyr|Pyrenylferrocene (left) and ITO|Vinylferrocene (right).	35
Figure 2.9	Equivalent circuits used to fit EIS data at (A) 0 V vs SCE and (B) 0.4 V vs SCE.	37
Figure 2.10	Nyquist plots for ITO|Pyr|Pyrenylferrocene (left) and ITO|Vinylferrocene (right). Raw EIS data are shown as solid circles and fits are represented as solid lines.	37
Figure 2.11	Cole-Cole plots for ITO|Pyr|Pyrenylferrocene (left) and ITO|Vinylferrocene (right). Raw EIS data are shown as solid circles and fits are represented as solid lines.	39
Figure 3.1	High-resolution XPS spectra of the N 1s region of ITO|Pyr|Pyr$(AQ)_2$ and ITO|Pyr.	54

Figure 3.2 Cyclic voltammetry of ITO|Pyr|Pyr(AQ)$_2$, ITO|Pyr, ITO, and ITO treated with Pyr(AQ)$_2$ performed at 50 mV/s in 100 mM pH 7 HEPES buffer with 100 mM KCl as a supporting electrolyte. 55

Figure 3.3 Variable scan rate cyclic voltammetry of ITO|Pyr|Pyr(AQ)$_2$ performed in 100 mM pH 7 HEPES buffer with 100 mM KCl as a supporting electrolyte (left) and the corresponding peak current density vs scan rate plot (right). 56

Figure 3.4 Variable scan rate cyclic voltammetry of Pyr(AQ)$_2$ performed in dimethylformamide (left) and the corresponding peak current density vs square root of scan rate plot (right). 57

Figure 3.5 Variable scan rate cyclic voltammetry of ITO|Pyr|Pyr(AQ)$_2$ performed in 100 mM pH 5 citrate buffer with 100 mM KCl as a supporting electrolyte (left) and the corresponding peak current density vs scan rate plot (right). 58

Figure 3.6 Variable scan rate cyclic voltammetry of ITO|Pyr|Pyr(AQ)$_2$ performed in 100 mM pH 6 citrate buffer with 100 mM KCl as a supporting electrolyte (left) and the corresponding peak current density vs scan rate plot (right). 58

Figure 3.7 Variable scan rate cyclic voltammetry of ITO|Pyr|Pyr(AQ)$_2$ performed in 100 mM pH 8 HEPES buffer with 100 mM KCl as a supporting electrolyte (left) and the corresponding peak current density vs scan rate plot (right). 59

Figure 3.8 Variable scan rate cyclic voltammetry of ITO|Pyr|Pyr(AQ)$_2$ performed in 100 mM pH 9 carbonate buffer with 100 mM KCl as a supporting electrolyte (left) and the corresponding peak current density vs scan rate plot (right). 59

Figure 3.9 Trumpet plots of of ITO|Pyr|Pyr(AQ)$_2$ at pH 7. 61

Figure 3.10 Trumpet plots of of ITO|Pyr|Pyr(AQ)$_2$ at pH 5, 6, 8, and 9. 62

Figure 3.11 Variable scan rate cyclic voltammetry of AQS performed in 100 mM pH 5 citrate buffer with 100 mM KCl as a supporting electrolyte (left) and the corresponding peak current density vs square root of scan rate plot (right). 64

Figure 3.12 Variable scan rate cyclic voltammetry of AQS performed in 100 mM pH 6 citrate buffer with 100 mM KCl as a supporting electrolyte (left) and the corresponding peak current density vs square root of scan rate plot (right). 64

Figure 3.13 Variable scan rate cyclic voltammetry of AQS performed in 100 mM pH 7 HEPES buffer with 100 mM KCl as a supporting electrolyte (left) and the corresponding peak current density vs square root of scan rate plot (right). 65

Figure 3.14 Variable scan rate cyclic voltammetry of AQS performed in 100 mM pH 8 HEPES buffer with 100 mM KCl as a supporting electrolyte (left) and the corresponding peak current density vs square root of scan rate plot (right). 65

Figure 3.15 Variable scan rate cyclic voltammetry of AQS performed in 100 mM pH 9 Borate buffer with 100 mM KCl as a supporting electrolyte (left) and the corresponding peak current density vs square root of scan rate plot (right). 66

Figure 3.16 $E_{1/2}$ vs pH plot (left) and Log(k_{app}) vs pH plot (right) for ITO|Pyr|Pyr(AQ)$_2$ and AQS between pH 5 and 9. 67

Figure 3.17 Plots of $E_{p,c}$ vs the log of the scan rate for AQS at varying pH. The slopes linear portions of the plots were used to determine the electron transfer coefficient, α, using Equation 3.3. The relatively fast electron transfer at pH 9 required faster scan rates to reach the irreversible region. 68

Figure 4.1 Cyclic voltammetry of ITO, ITO | Pyr, and ITO | Pyr | Ru(bda)(pypyr)$_2$ in 100 mM Na_2SO_4 performed under N_2. 83

Figure 4.2 Variable scan rate cyclic voltammetry of the $Ru^{III/II}$ couple of ITO | Pyr | Ru(bda)(pypyr)$_2$ in 100 mM Na_2SO_4 performed under N_2 (left) and the corresponding peak current vs square root of scan rate plot (right). 84

Figure 4.3 Controlled potential electrolysis of ITO | Pyr | Ru(bda)(pypyr)$_2$ performed in 100 mM Na_2SO_4 under N_2 at 0.8 V vs SCE (left) and the cyclic voltammetry before and after electrolysis. 85

Figure 5.1 Transmission mode FTIR spectra of b-Si|Aromatic samples. Samples were illuminated at 75° off of the surface normal. 99

Figure 5.2 IR spectrum of 1-vinylpyrene. 99

Figure 5.3 High-resolution Co 2p XPS spectra of all b-Si|Aromatic (red traces) and b-Si|Aromatic|[Co] (blue traces) electrodes. 100

Figure 5.4 High-resolution Si 2p XPS spectra of b-Si (black traces), b-Si|Aromatic (red traces) and b-Si|Aromatic|[Co] (blue traces). 101

Figure 5.5 The secondary electron cut-off region for XPS measurements of b-Si|Aromatic (top) (red traces) and b-Si|Aromatic|[Co] (bottom). 103

Figure 5.6 Linear sweep voltammograms of b-Si, b-Si|Aromatic, and b-Si|Aromatic|[Co] samples in 0.1 M H_2SO_4 under 100 mW/cm^2 white-light illumination (solid traces) and in the dark (dashed traces). 104

Figure 5.7 Linear sweep voltammograms of b-Si and b-Si|Aromatic samples in 0.1 M H_2SO_4 under 100 mW/cm^2 white-light illumination. The inset shows the region near the onset potential of –1 mA/cm^2. 105

Figure 5.8 Bar chart of onset potential a function of molecular layer identity for b-Si|Aromatic (red bars) and b-Si|Aromatic|[Co] samples (blue bars). 106

Figure 5.9 ΔI vs potential for all b-Si|Aromatic|[Co] electrodes. ΔI is obtained by subtracting the current densities from the linear sweep voltammograms of b-Si|Aromatic from those of b-Si|Aromatic|[Co]. 107

Figure 5.10 IMHFR plots for b-Si|Aromatic and b-Si|Aromatic|[Co]. The vertical lines represent the flatband potential which is taken as the potential where the ΔR value deviated significantly (> 4 standard deviations) from the average value of the flat region of the curve for two consecutive points. 108

Figure 5.11 Bar chart of V_{FB} as a function of molecular layer identity for b-Si|Aromatic (red bars) and b-Si|Aromatic|[Co] (blue bars). 109

Figure 5.12 Current vs time plots for photoelectrolysis of b-Si|Aromatic (left) and b-Si|Aromatic|[Co] (right) at –0.4 V vs RHE in 0.1 M H_2SO_4 under 1 sun illumination. 110

Figure A.1 P 2p XPS spectrum of ITO | PyrPA (left) and the plot of P/In ratio vs PyrPA concentration used for attachment to ITO (right). 125

Figure A.2 N 1s XPS spectrum of ITO | NDI. 127

Figure A.3 Cyclic voltammograms of ITO | NDI performed in 100 mM pH 7 phosphate buffer. 127

Figure A.4 Variable scan rate cyclic voltammetry of saturated PDI performed in 100 mM $TBAPF_6$ in CH_2Cl_2 (left) and the corresponding peak current vs square root of scan rate plot for scan rates at which the two redox events are distinguishable from one another (right). 128

Figure A.5 Variable scan rate cyclic voltammetry of ITO | Pyr | PDI performed in 100 mM pH 7 HEPES buffer with 100 mM KCl as the surrporting electrolyte (left) and the corresponding peak current vs scan rate plot (right). 130

Figure A.6 Consecutive cyclic voltammograms of ITO | Pyr | PDI performed in 100 mM $TBAPF_6$ in CH_3CN. 130

Figure A.7 ^{1}H NMR of PyrPA in DMSO-d_6. 134

Figure A.8 $^{13}C\{^1H\}$ NMR of PyrPA in DMSO-d_6. 134

Figure A.9 $^{31}P\{^{1}H\}$ NMR of PyrPA in DMSO-d_6 135

Figure A.10 ^{1}H NMR of PDI in $CDCl_3$. 136

Figure A.11 UV-visible absorption spectrum of saturated PDI in CH_2Cl_2. 136

LIST OF TABLES

		Page
Table 2.1	Resistance and constant phase element values extracted from fitting EIS data.	39
Table 3.1	Redox potentials and rates of electron transfer of ITO|Pyr|Pyr(AQ)$_2$ and AQS under varying pH conditions.	59
Table 5.1	sp^2 IR stretches for surface-bound and free aromatics	98
Table 5.2	Compositional analysis of b-Si, b-Si|Aromatic and b-Si|Aromatic|[Co].	101
Table 5.3	Summary of data extracted from XPS and voltammetric measurements.	103

LIST OF SCHEMES

		Page
Scheme 1.1	General representation of a phototelectrochemical (PEC) cell for solar fuel generation.	3
Scheme 1.2	Pictorial representation of molecular attachment to aromatic electrodes *via* π-π interactions.	7
Scheme 1.3	Pictorial representation of the hybrid approach for non-covalent attachment of molecular catalysts onto electrode surfaces.	8
Scheme 2.1	Pictorial representation of the attachment of ferrocene to indium tin oxide (ITO) through (A) non-covalent and (B) covalent interactions.	25
Scheme 3.1	Pictorial representation of the attachment of anthraquinone to indium tin oxide (ITO) electrodes through non-covalent interactions.	52
Scheme 4.1	Sun's class of water oxidation catalysts (left) and a schematic representation of the attachment of a Ru-bda catalyst to ITO|Pyr via π-π interactions.	81
Scheme 5.1	Band diagrams of a p-type semiconductor before and after equilibration with a redox couple in solution without (left) and with (right) a surface dipole.	93
Scheme 5.2	Band diagrams of a p-type semiconductor at three potential regimes (top) and the corresponding chopped-light resistivity measurements at the three potential regimes (bottom).	95
Scheme 5.3	General Representation of the Modification of b-Si Electrodes (Top) and Pictorial Representations of the Various Modified Electrodes (Bottom).	97
Scheme A.1	Pictorial representation of the covalent attachment of PyrPA to ITO.	124
Scheme A.2	Pictorial representation of the covalent attachment of NDI to ITO.	126
Scheme A.3	Pictorial representation of the non-covalent attachment of PDI to ITO | Pyr.	127

ACKNOWLEDGMENTS

To my PI, Jenny Yang – I am endlessly grateful for your encouragement and faith in me as a scientist. Thank you for granting me freedom and independence on this project. We are incredibly lucky to have you as a leader and mentor.

Shane Ardo and Alan Heyduk – thank you for your guidance and for pushing me to think about chemistry from a new perspective.

Thank you to anyone at NREL who taught me to use an instrument, offered input on data, or shared a ski lift with me. Nate Neale – thank you for your collaboration, mentorship, and willingness to jump into lab to show me the ropes. Ryan Pekarek – you pushed me to work harder and think deeper about science and I will carry that into all of my future scientific endeavors.

Charlene, Annie, Steven, Nadia, Juliet, Brian, Zach, Bianca, Alex, Drew, Jeff, Tyler, Sarah, Allie, Ian, Rebecca, Wyeth, Andrew, and Reyna – you drove me absolutely insane and I'm so grateful to have worked with a group of people who felt more like family than coworkers. Thank you for teaching me everything from how to use a glovebox to the proper definition of a sandwich.

Megan, Krista, Jared, Devon, and Dan – thank you for the laughs, the beers, and the constant encouragement. You somehow made our first year the most fun year of my life and I wouldn't have made it through the final (and much harder) years without the Big Bear trips, beach parties, and afternoons at the pub.

Steve and Austin (and Maya) – thank you for the surf days, the mountain days, and for putting up with me at my finest.

Sam, Heather, Becca, Ashley, and Emma – thank you for the 24/7, long-distance support.

Grandma, Paul, Kerrin, and Syd – moving far from you was the hardest part of grad school. Thank you for your constant love and for always welcoming me back home.

Kevin – thank you for knowing exactly how to support me, for all of the soup and ice cream, and for being my home away from home.

Mom – you got me here. You taught me to think deeply, to work hard, to be my own person, and to chase my dreams. Thank you for everything.

And lastly, to Papa and Alan – you are tangled into every page of this thesis. Thank you for believing in me, reminding me to go outside, and teaching me to not take life too seriously.

CURRICULUM VITAE

Caitlin Hanna

Education

University of California, Irvine | Irvine, CA
Doctor of Philosophy, Inorganic Chemistry, expected December 2019

University of Massachusetts Dartmouth | Dartmouth, MA
Bachelor of Science, Chemistry, May 2015

Research Experience

Graduate Student Researcher **Sept 2015-Dec 2019**
University of California, Irvine | Advisor: Prof. Jenny Yang
Understanding interfacial electron transfer properties at molecularly modified conducting electrodes.

- Optimized a novel procedure for the attachment of molecular species to conducting electrodes.
- Characterized modified electrodes using a variety of spectroscopic methods (XPS, Fluorescence, FTIR).
- Utilized electrochemical techniques (CV, EIS) to analyze electron transfer and proton coupled electron transfer of surface-attached redox-active molecules.

DOE Office of Science Graduate Student Research Fellow **Jan 2019-May 2019**
National Renewable Energy Laboratory, Golden CO | Advisor: Dr. Nathan Neale
Functionalization of high surface area silicon photoelectrodes with molecular electrocatalysts for photoelectrochemical proton reduction in water.

- Functionalized semiconductor electrodes with molecular electrocatalysts using rigorous air-free techniques (Schlenk line and glove box).
- Integrated voltammetric and impedance techniques to study thermodynamics and kinetics of photoelectrochemical proton reduction at modified silicon photoelectrodes.
- Utilized materials characterization techniques (XPS and FTIR) to characterize functionalized electrodes.

Undergraduate Student Researcher **Mar 2014- May 2015**
University of Massachusetts Dartmouth | Advisor: Prof. Emmanuel Ojadi
Analysis of the optical gas sensing properties of immobilized porphyrin dyes.

- Immobilized porphyrin dyes onto textile materials for the optical sensing of volatile organic compounds.
- Analyzed optical sensing ability with fluorescence and UV-visible spectroscopy.

Publications

1. Hanna, C. M., Luu, A., Yang, J. Y. "Proton-Coupled Electron Transfer at Anthraquinone Modified Indium Tin Oxide Electrodes" *ACS Appl. Energy Mat*. **2019**, *2*, 59-65.

2. Hanna, C. M., Sanborn, C. D., Ardo, S., Yang, J. Y. "Interfacial Electron Transfer of Ferrocene Immobilized onto Indium Tin Oxide through Covalent and Noncovalent Interactions" *ACS Appl. Mater. Interfaces,* **2018***, 10*, 13211-13217.
3. Kotyk, J. F. K., Hanna,C. M., Combs, R. L., Ziller, J. W., Yang, J. Y. "Intramolecular Hydrogen-Bonding in a Cobalt Aqua Complex and Electrochemical Water Oxidation Activity" *Chem. Sci*. **2018**, *9*, 2750 – 2755.

Awards

Graduate Dean's Dissertation Fellowship Award	2019
Department of Energy Office of Science Graduate Student Research Fellowship	2018
AVS Dorothy M. and Earl S. Hoffman Travel Grant	2018
ISF-2 Young Diversity Travel Award	2017
American Institute of Chemists Award	2015
ACS Analytical Division Award	2014
Merck Index Award	2013
CRC Freshman Chemistry Award	2012

Presentations

1. Hanna, C. M., Neale, N. R., Yang, J. Y. "Immobilization of a Molecular Proton Reduction Catalyst onto High-Surface Area Silicon Photoelectrodes" American Chemical Society National Meeting, San Diego, August 2019.
2. Hanna, C. M., Lydon, B. R., Luu, A., Yang, J. Y. "Developing a Mild and Modular Route to Chemically Modified Electrodes for Photoelectrochemical Cells" American Chemical Society National Meeting, San Diego, CA, August 2019.
3. Hanna, C. M., Yang, J. Y. "Interfacial Electron Transfer of Ferrocene Immobilized onto Indium Tin Oxide through Noncovalent Interactions" American Vacuum Society International Symposium, Long Beach, CA, October 2018.
4. Hanna, C. M., Yang, J. Y. "Interfacial Electron Transfer of Ferrocene Immobilized onto Indium Tin Oxide through Covalent and Noncovalent Interactions" [poster] Next Generation Electrochemistry Workshop, Chicago, IL, June 2018.
5. Hanna, C. M., Yang, J. Y. "Noncovalent Method for Molecular Immobilization on Photovoltaic Surfaces" [poster] International Solar Fuels Young Conference, San Diego, CA, July 2017.
6. Hanna, C. M., Lydon, B. L., Yang, J. Y. "Noncovalent Method for Molecular Immobilization on Photovoltaic Surfaces" [poster] Southern California American Vacuum Society Symposium Conference, Buena Vista, CA, October 2016.
7. Hanna, C. M., Ojadi, E. C. A. "Optical Gas Sensing Porphyrin/Indium Oxide Systems" [poster] Sigma Xi Research Conference, North Dartmouth, MA, May 2015.

Teaching Experience

Laboratory Teaching Assistant

University of California, Irvine

- Supervised and directed students in general, organic, and inorganic chemistry techniques
- Encouraged and enforced safety within the teaching laboratory

- Instructed students on proper notebook-keeping

Lecture Teaching Assistant
University of California, Irvine
- Ran discussion sessions in general and inorganic chemistry
- Organized five to ten graduate students to grade 400 exams

Leadership Experience

Graduate Mentor, Yang Group, University of California, Irvine
- Trained undergraduate and junior graduate students to safely and successfully perform scientific research.

Activities Coordinator, Iota Sigma Pi Calcium Chapter, University of California, Irvine
- Organized events for women in chemistry at UCI to facilitate networking amongst club members.

President, Chemistry Club, University of Massachusetts, Dartmouth
- Organized fundraising, outreach, and networking events for club members to get involved with the university and the neighboring communities.

ABSTRACT OF THE DISSERTATION

Advancement and Application of a Non-Covalent Method for Molecular Attachment to Electrode Surfaces

By

Caitlin Marie Hanna

Doctor of Philosophy in Chemistry

University of California, Irvine, 2019

Professor Jenny Y. Yang, Chair

Chemically modified electrodes are useful for a wide variety of applications such as catalysis, sensing, and electronics. The attachment of molecular electrocatalysts onto electrode surfaces is of particular interest for the enhancement of heterogeneous redox catalysis. This dissertation describes a synthetically versatile approach for the immobilization of molecular species to conducting and semiconducting surfaces. Indium tin oxide (ITO) and silicon surfaces are covalently modified with aromatic molecules followed by attachment of aromatic-appended molecular species via π-π interactions.

Chapter 2 describes the immobilization of ferrocene onto ITO through covalent and non-covalent interactions and compares electron transfer kinetics between the two attachment methods. Electron transfer kinetics across the non-covalently modified interface demonstrate a ten-fold increase relative to the analogous covalent attachment strategy.

Chapter 3 outlines the attachment of a pyrene-bound anthraquinone derivative to pyrene-appended ITO. Comparison of the proton-coupled electron transfer properties of the surface-bound anthraquinone to that of a water soluble anthraquinone derivative

demonstrates that the immobilized molecule retains its expected reactivity based on a similar homogeneous system.

Chapter 4 describes the attachment of a pyrene-appended molecular water oxidation catalyst to ITO via π-π interactions. Electrochemical analysis proves successful attachment of the catalyst to ITO. However, the modified electrode is unstable under electrocatalytic conditions due to loss of the catalyst from the electrode surface.

In Chapter 5, four aromatic molecules are covalently attached to nanoporous silicon electrodes followed by non-covalent attachment of a molecular proton reduction catalyst with aromatic ligands. Photoelectrochemical and impedance techniques are utilized to probe the light-assisted electrocatalytic proton reduction ability of the modified silicon electrodes.

CHAPTER 1

Introduction

1.1 Chemically Modified Electrodes

Chemical modification of electrode surfaces is a versatile approach for developing electrode materials with molecular specificity, tunable surface energetics, and high selectivity.[1-19] First introduced by Murray in the 1980s,[1-3] chemically modified electrodes (CMEs) have since been extensively studied for application in electronics, sensing, and electrocatalysis.[4-19] Chemical modification of electrodes modulates electrodes' surface energetics (e.g. work function, band energies); CMEs are therefore beneficial in electronic devices that require electronic communication between two materials.[6, 9-11, 13, 17] For example, Xie et al. demonstrated the tunability of charge transport at metal|molecule junctions by adjusting the work function of the metal and the HOMO of the molecule using a variety of alkyl thiol self-assembled monolayers (SAMs) on Au, Ag, and Pt electrodes.[20] Alternatively, the advantage of CMEs in sensing and biosensing technology is two-fold: CMEs can promote selective binding of the analyte of interest and prevent fouling caused by adsorption of adventitious species (e.g. cells, proteins).[4, 6, 15-17] Pivotal work from the Whitesides group demonstrated the ability of alkyl thiol SAMs on Au to resist protein binding to the electrode surface.[21-22] Subsequent modification of the SAM's terminal functional group enables selective binding of analyte.[4, 15-17] Mayall et al., for example, utilized nickel nitrilotriacetate acid-modified SAMs to detect human Toll-Like Receptor-4, a protein responsible for detecting lipopolysaccharide of Gram-negative bacteria, at gold electrodes.[23]

CMEs are of great interest in electrocatalysis in order to exploit the benefits of molecular electrocatalysts on an electrode surface.[7] Molecular electrocatalysts are advantageous due to their tunable reactivity (*via* ligand design) and high selectivity.[24-27] Immobilization of molecular electrocatalysts onto electrode surfaces reduces the amount of

catalyst needed, circumvents diffusion limitations, and enables use in solvents in which the free catalyst is insoluble.[7] CMEs have been utilized for a variety of electrocatalytic reactions including proton reduction,[28-45] water oxidation,[28, 46-56] oxygen reduction,[57-64] CO_2 reduction[38, 65-73], and alcohol oxidation.[74] Of particular interest is the application of CMEs to photoelectrochemical (PEC) cells for direct conversion of sunlight into chemical bonds.[75-78] While multiple PEC cell configurations exist, Scheme 1.1 depicts a PEC cell utilizing a p-type semiconductor as a photocathode and a water oxidation catalyst as the counter electrode. Briefly, the photocathode absorbs sunlight and separates charge *via* excitation of electrons into the conduction band. Electrons are then driven toward the photocathode | liquid junction where they participate in proton reduction and holes are driven to the counter electrode where they participate in water oxidation.[75-78] Unfortunately, most photocathode materials are poor catalysts for fuel-forming reactions.[76, 78-79] The use of CMEs that incorporate fuel-forming catalysts onto the surface of photocathode materials could therefore significantly improve efficiencies of PEC cells.[75-78]

Scheme 1.1. General representation of a phototelectrochemical (PEC) cell for solar fuel generation.

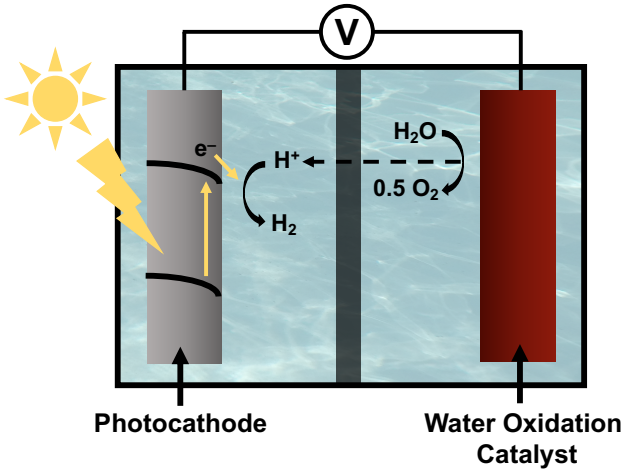

1.2 Molecular Attachment to Electrodes Through Covalent Bonds

CMEs are traditionally synthesized by forging covalent bonds between an electrode and the attached molecule. One of the most common strategies for covalent modification of electrodes utilizes thiol functional groups to generate metal-thiolate bonds at the electrode surface. Thiolate surface chemistry is applicable to a variety of metallic surfaces (Au, Ag, Cu, Pt, Pd, Ni) and generates dense and stable monolayers due to the strong metal-thiolate bond and van der Waals interactions between neighboring molecules.[4, 17, 80] CMEs prepared with metal-thiolate SAMs have been extensively utilized in electronics,[4, 17, 20, 80] sensors,[4, 14-16, 23, 81-82] and electrocatalysis.[2, 7, 56] Early work from the Murray group immobilized a cobalt porphyrin oxygen reduction electrocatalysts onto Au electrodes using Au-thiolate chemistry.[56] Thiolate functional groups, however, are less extensively studied on Si and metal oxide electrodes, both of which are commonly used in PEC cell technology.[6, 9]

Covalent modification of Si electrodes is well established.[6, 11, 19] The various routes for covalent attachment to Si surfaces are shown in Figure 1.1, all of which require initial removal of the native SiO_x layer. Subsequent reactivity with the terminal Si-H sites enables formation of SAMs at the Si surface through Si-C, Si-N, or Si-chalcogenide (O, S, Se, Te) bonds.[6] The choice of route for covalent modification of Si depends on synthetic feasibility (i.e. the ability to functionalize the molecular species of interest with the functional group necessary for attachment) and the application of the electrode. The Grignard chlorination/alkylation route described in Figure 1.1g, for example, is advantageous for use in aqueous solvents because it enables back-filling of unreacted Si-Cl sites with methyl groups which enhances the stability of the electrode in water by preventing Si oxidation.[83-86] The Lewis[85] and Rose[45] groups both developed CMEs for PEC fuel-forming reactions through direct covalent

attachment of molecular proton reduction catalysts to Si electrodes. The CMEs prepared by the Lewis group using metal bipyridal electrocatalysts were unstable under photoelectrochemical conditions, potentially due to weakening of the surface Si-C bond upon a ligand-centered reduction of the catalyst.[85] On the other hand, the Rose group immobilized a nickel bis(diphosphine) catalyst onto Si(111) and demonstrated stability of the CME throughout photoelectrochemical proton reduction in nonaqueous conditions.[45]

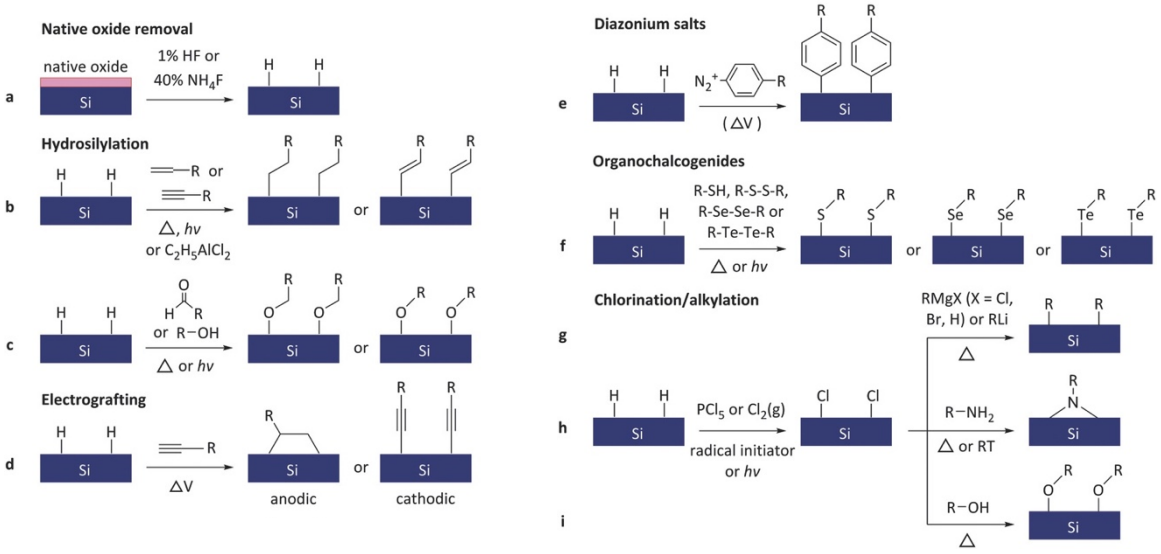

Figure 1.1. Methods for covalent attachment to silicon electrodes. Adapted from ref. 6 under the terms of the Creative Commons Attribution Non-Commercial No Derivatives License CC BY-NC-ND.

Similar to covalent modification of silicon, many functional groups are available for covalent attachment to metal oxides (Figure 1.2). The terminal hydroxyl groups at metal oxide surfaces serve as reactive sites for reactivity with silanes, phosphonates, carboxylates, catechols, alkenes, alkynes, and amines.[9-10] Again, choice of attachment strategy depends on synthetic feasibility and application. Metal oxide SAMs formed with silane functional groups, for example, readily undergo hydrolysis and are therefore unfit for applications in aqueous conditions.[9] Covalent modification of metal oxides is useful in PEC technology because metal

oxide semiconductors are commonly employed as protective layers atop Si photoelectrodes.[29, 87-92] Leung et al. utilized phosphonic acid functional groups to append a nickel bis(diphosphine) proton reduction catalyst to TiO_2-protected Si electrodes; this CME exhibited a high turnover number and remained stable for up to 24 h of sustained photoelectrolysis.[29]

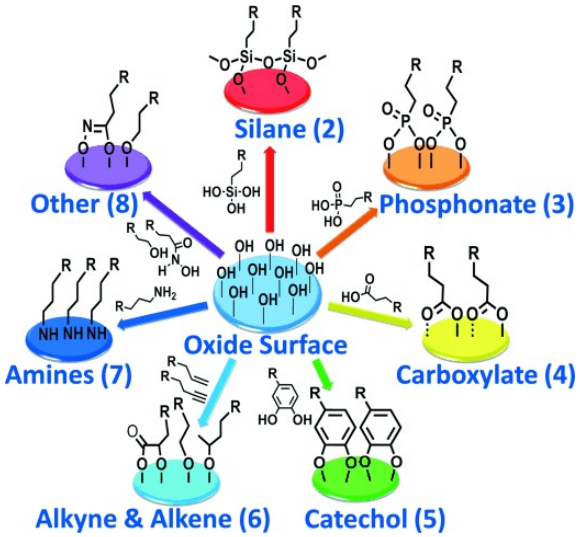

Figure 1.2. Methods for covalent attachment to metal oxide electrodes. Reproduced from ref. 9 with permission from John Wiley and Sons, Inc.

1.3 Molecular Attachment to Electrodes Through π-π Interactions

An alternative strategy for preparing CMEs utilizes π-π interactions to immobilize polycyclic aromatic-appended molecules to aromatic electrode surfaces such as graphene, HOPG, and carbon nanotubes (Scheme 1.2). The adsorption of polycyclic aromatics to graphitic electrodes was first demonstrated by Brown et al. in the late 1970s.[93] π-π interactions were later utilized to immobilize proteins onto electrode surfaces for fundamental understanding of protein electrochemistry and use in sensors.[94-95] In recent years, CMEs prepared through π-π interactions with polycyclic aromatic-appended metal complexes have been extensively studied in order to understand adsorption and electron

transfer processes at these electrodes[96-99] and for use in electrocatalysis.[31, 35, 38, 49, 57, 66-68, 73-74] For example, Tran et al. immobilized a pyrene-appended nickel bis(diphosphine) proton reduction catalyst onto carbon nanotubes via π-π interactions, demonstrating robust electrocatalytic hydrogen evolution at low pH.[31] The polycyclic aromatic linkers allow for facile electron transfer between the electrode and the attached complex without sacrificing catalytic activity. Furthermore, the π-π interactions demonstrate stability in a range of solvents and electrolytic conditions.[31, 35, 38, 49, 57, 66-68, 73-74]

Scheme 1.2. Pictorial representation of molecular attachment to aromatic electrodes *via* π-π interactions.

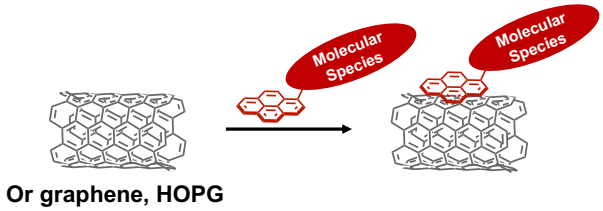

1.4 Hybrid Approach for Molecular Attachment to Electrodes

The Yang lab developed a technique for preparation of CMEs that enables attachment of pyrene-appended molecules to non-aromatic surfaces by integrating the covalent and non-covalent methods described in Sections 1.2 and 1.3. This approach, illustrated in Scheme 1.3, effectively "aromatizes" surface through covalent attachment of pyrene, which facilitates physisorption of pyrene-functionalized molecules via π-π interactions and could serve as a protective layer against corrosion at the electrode surface. This hybrid technique is synthetically advantageous due to the ease of pyrene functionalization onto both electrode surfaces and molecular electrocatalysts. Further, the hybrid attachment method is applicable to any surface onto which pyrene functionalization is feasible. Initial work on gold foil electrodes established that surface-bound pyrene can engage in π-π stacking with 1-

pyrenylferrocene, providing a novel route for the immobilization of ferrocene onto electrode surfaces with facile electron transfer between the electrode and bound ferrocene.[100]

Scheme 1.3. Pictorial representation of the hybrid approach for non-covalent attachment of molecular species onto electrode surfaces.

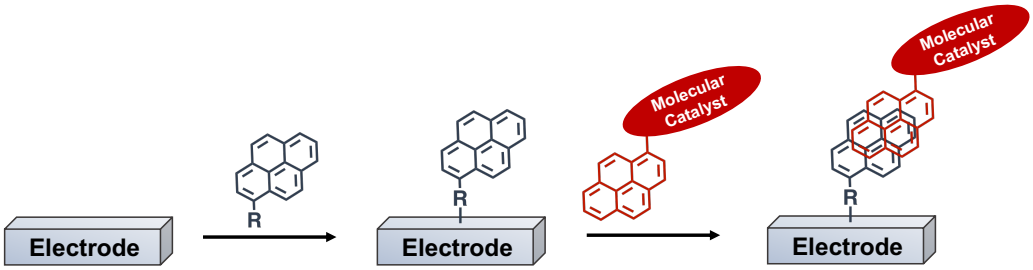

1.5 Thesis Overview

This dissertation describes the advancement of the hybrid technique for preparation of CMEs developed in the Yang lab as well as application of the hybrid attachment technique to photoelectrocatalytic proton reduction. Indium tin oxide (ITO) surfaces were covalently modified with pyrene monolayers followed by attachment of pyrene-appended molecular species via π-π interactions. Two redox probe molecules, pyrene-bound ferrocene and pyrene-bound anthraquinone, were immobilized onto pyrene-appended ITO in order to understand electron transfer kinetics and proton-coupled electron transfer at the non-covalently modified electrodes. Additionally, a pyrene-bound water oxidation catalyst was attached to pyrene-appended ITO in an attempt to prepare a CME for electrocatalytic water oxidation. Finally, a variety of aromatic molecules were covalently attached to nanoporous silicon electrodes followed by non-covalent attachment of a molecular proton reduction catalyst. Photoelectrochemical and impedance techniques were utilized to probe the light-assisted electrocatalytic proton reduction ability of the modified silicon electrodes.

These studies highlight the versatility of the hybrid procedure for the attachment of molecular species onto electrode surfaces. Spectroscopic and electrochemical studies with redox probe molecules on ITO indicate the attachment method is suitable for applications requiring facile electron transfer (Chapter 2) and selective reactivity with incoming substrates (Chapter 3). A molecular water oxidation catalyst was successfully attached to ITO but the electrode was unstable under electrocatalytic conditions (Chapter 4). Finally, a thermodynamic and kinetic analysis of proton reduction at molecular catalyst-modified silicon photoelectrodes enhances the fundamental understanding of interfacing molecular electrocatalysts with photovoltaic electrodes (Chapter 5), advancing progress toward direct sunlight-to-fuel technology.

1.6 References

1. Murray, R. W., Chemically modified electrodes. *Accounts of Chemical Research* **1980,** *13*, 135-141.

2. Murray, R. W.; Goodenough, J. B.; Albery, W. J., Modified Electrodes: Chemically Modified Electrodes for Electrocatalysis [and Discussion]. *Philosophical Transactions of the Royal Society of London. Series A, Mathematical and Physical Sciences* **1981,** *302*, 253-265.

3. Murray, R. W.; Ewing, A. G.; Durst, R. A., Chemically modified electrodes. Molecular design for electroanalysis. *Analytical Chemistry* **1987,** *59*, 379A-390A.

4. Casalini, S.; Bortolotti, C. A.; Leonardi, F.; Biscarini, F., Self-assembled monolayers in organic electronics. *Chemical Society Reviews* **2017,** *46*, 40-71.

5. Veerbeek, J.; Firet, N. J.; Vijselaar, W.; Elbersen, R.; Gardeniers, H.; Huskens, J., Molecular Monolayers for Electrical Passivation and Functionalization of Silicon-Based Solar Energy Devices. *ACS Applied Materials & Interfaces* **2017,** *9*, 413-421.

6. Veerbeek, J.; Huskens, J., Applications of Monolayer-Functionalized H-Terminated Silicon Surfaces: A Review. *Small Methods* **2017,** *1*, 1700072.

7. Bullock, M.; Das, A. K.; Appel, A. M., Surface Immobilization of Molecular Electrocatalysts for Energy Conversions. *Chemistry – A European Journal* **2017**, 7626-7641.

8. Hotchkiss, P. J.; Jones, S. C.; Paniagua, S. A.; Sharma, A.; Kippelen, B.; Armstrong, N. R.; Marder, S. R., The Modification of Indium Tin Oxide with Phosphonic Acids: Mechanism of Binding, Tuning of Surface Properties, and Potential for Use in Organic Electronic Applications. *Accounts of Chemical Research* **2012,** *45*, 337-346.

9. Pujari, S. P.; Scheres, L.; Marcelis, A. T. M.; Zuilhof, H., Covalent Surface Modification of Oxide Surfaces. *Angewandte Chemie International Edition* **2014,** *53*, 6322-6356.

10. Paniagua, S. A.; Giordano, A. J.; Smith, O. N. L.; Barlow, S.; Li, H.; Armstrong, N. R.; Pemberton, J. E.; Brédas, J.-L.; Ginger, D.; Marder, S. R., Phosphonic Acids for Interfacial Engineering of Transparent Conductive Oxides. *Chemical Reviews* **2016,** *116*, 7117-7158.

11. Vilan, A.; Cahen, D., Chemical Modification of Semiconductor Surfaces for Molecular Electronics. *Chemical Reviews* **2017,** *117*, 4624-4666.

12. Ulgut, B.; Abruña, H. D., Electron Transfer through Molecules and Assemblies at Electrode Surfaces. *Chemical Reviews* **2008,** *108*, 2721-2736.

13. Lee, H. J.; Jamison, A. C.; Lee, T. R., Surface Dipoles: A Growing Body of Evidence Supports Their Impact and Importance. *Accounts of Chemical Research* **2015,** *48*, 3007-3015.

14. Wink, T.; J. van Zuilen, S.; Bult, A.; P. van Bennekom, W., Self-assembled Monolayers for Biosensors. *Analyst* **1997,** *122*, 43R-50R.

15. Samanta, D.; Sarkar, A., Immobilization of bio-macromolecules on self-assembled monolayers: methods and sensor applications. *Chemical Society Reviews* **2011,** *40*, 2567-2592.

16. Radecka, H.; Radecki, J.; Grabowska, I.; Kurzątkowska, K., Electrochemical Sensors and Biosensors Based on Self-Assembled Monolayers: Application of Nanoparticles for Analytical Signals Amplification. In *Functional Nanoparticles for Bioanalysis, Nanomedicine, and Bioelectronic Devices Volume 1*, American Chemical Society: 2012; Vol. 1112, pp 293-312.

17. Love, J. C.; Estroff, L. A.; Kriebel, J. K.; Nuzzo, R. G.; Whitesides, G. M., Self-Assembled Monolayers of Thiolates on Metals as a Form of Nanotechnology. *Chemical Reviews* **2005,** *105*, 1103-1170.

18. Eckermann, A. L.; Feld, D. J.; Shaw, J. A.; Meade, T. J., Electrochemistry of redox-active self-assembled monolayers. *Coordination chemistry reviews* **2010,** *254*, 1769-1802.

19. Aswal, D. K.; Lenfant, S.; Guerin, D.; Yakhmi, J. V.; Vuillaume, D., Self assembled monolayers on silicon for molecular electronics. *Analytica Chimica Acta* **2006,** *568*, 84-108.

20. Xie, Z.; Bâldea, I.; Frisbie, C. D., Energy Level Alignment in Molecular Tunnel Junctions by Transport and Spectroscopy: Self-Consistency for the Case of Alkyl Thiols and Dithiols on Ag, Au, and Pt Electrodes. *Journal of the American Chemical Society* **2019**.

21. Prime, K. L.; Whitesides, G. M., Self-assembled organic monolayers: model systems for studying adsorption of proteins at surfaces. *Science* **1991,** *252*, 1164.

22. Prime, K. L.; Whitesides, G. M., Adsorption of proteins onto surfaces containing end-attached oligo(ethylene oxide): a model system using self-assembled monolayers. *Journal of the American Chemical Society* **1993,** *115*, 10714-10721.

23. Mayall, R. M.; Renaud-Young, M.; Chan, N. W. C.; Birss, V. I., An electrochemical lipopolysaccharide sensor based on an immobilized Toll-Like Receptor-4. *Biosensors and Bioelectronics* **2017,** *87*, 794-801.

24. Rakowski DuBois, M.; DuBois, D. L., The roles of the first and second coordination spheres in the design of molecular catalysts for H2 production and oxidation. *Chemical Society Reviews* **2009,** *38*, 62-72.

25. Thammavongsy, Z.; Mercer, I. P.; Yang, J. Y., Promoting proton coupled electron transfer in redox catalysts through molecular design. *Chemical Communications* **2019,** *55*, 10342-10358.

26. Barlow, J. M.; Yang, J. Y., Thermodynamic Considerations for Optimizing Selective CO2 Reduction by Molecular Catalysts. *ACS Central Science* **2019,** *5*, 580-588.

27. Blakemore, J. D.; Crabtree, R. H.; Brudvig, G. W., Molecular Catalysts for Water Oxidation. *Chemical Reviews* **2015,** *115*, 12974-13005.

28. Rosser, T. E.; Gross, M. A.; Lai, Y.-H.; Reisner, E., Precious-metal free photoelectrochemical water splitting with immobilised molecular Ni and Fe redox catalysts. *Chemical Science* **2016**.

29. Leung, J. J.; Warnan, J.; Nam, D. H.; Zhang, J. Z.; Willkomm, J.; Reisner, E., Photoelectrocatalytic H2 evolution in water with molecular catalysts immobilised on p-Si via a stabilising mesoporous TiO2 interlayer. *Chemical Science* **2017,** *8*, 5172-5180.

30. Berben, L. A.; Peters, J. C., Hydrogen evolution by cobalt tetraimine catalysts adsorbed on electrode surfaces. *Chemical Communications* **2010,** *46*, 398-400.

31. Tran, P. D.; Le Goff, A.; Heidkamp, J.; Jousselme, B.; Guillet, N.; Palacin, S.; Dau, H.; Fontecave, M.; Artero, V., Noncovalent Modification of Carbon Nanotubes with Pyrene-

Functionalized Nickel Complexes: Carbon Monoxide Tolerant Catalysts for Hydrogen Evolution and Uptake. *Angewandte Chemie International Edition* **2011,** *50*, 1371-1374.

32. Gulati, S.; Hietsoi, O.; Calvary, C. A.; Strain, J. M.; Pishgar, S.; Brun, H. C.; Grapperhaus, C. A.; Buchanan, R. M.; Spurgeon, J. M., Photocatalytic hydrogen evolution on Si photocathodes modified with bis(thiosemicarbazonato)nickel(ii)/Nafion. *Chemical Communications* **2019,** *55*, 9440-9443.

33. Beiler, A. M.; Khusnutdinova, D.; Jacob, S. I.; Moore, G. F., Solar Hydrogen Production Using Molecular Catalysts Immobilized on Gallium Phosphide (111)A and (111)B Polymer-Modified Photocathodes. *ACS Applied Materials & Interfaces* **2016,** *8*, 10038-10047.

34. Wadsworth, B. L.; Beiler, A. M.; Khusnutdinova, D.; Jacob, S. I.; Moore, G. F., Electrocatalytic and Optical Properties of Cobaloxime Catalysts Immobilized at a Surface-Grafted Polymer Interface. *ACS Catalysis* **2016,** *6*, 8048-8057.

35. Eady, S. C.; MacInnes, M. M.; Lehnert, N., Immobilized Cobalt Bis(benzenedithiolate) Complexes: Exceptionally Active Heterogeneous Electrocatalysts for Dihydrogen Production from Mildly Acidic Aqueous Solutions. *Inorganic Chemistry* **2017,** *56*, 11654-11667.

36. Beiler, A. M.; Khusnutdinova, D.; Wadsworth, B. L.; Moore, G. F., Cobalt Porphyrin–Polypyridyl Surface Coatings for Photoelectrosynthetic Hydrogen Production. *Inorganic Chemistry* **2017,** *56*, 12178-12185.

37. Khusnutdinova, D.; Beiler, A. M.; Wadsworth, B. L.; Jacob, S. I.; Moore, G. F., Metalloporphyrin-modified semiconductors for solar fuel production. *Chemical Science* **2017,** *8*, 253-259.

38. Blakemore, J. D.; Gupta, A.; Warren, J. J.; Brunschwig, B. S.; Gray, H. B., Noncovalent Immobilization of Electrocatalysts on Carbon Electrodes for Fuel Production. *Journal of the American Chemical Society* **2013,** *135*, 18288-18291.

39. Downes, C. A.; Marinescu, S. C., Efficient Electrochemical and Photoelectrochemical H2 Production from Water by a Cobalt Dithiolene One-Dimensional Metal–Organic Surface. *Journal of the American Chemical Society* **2015,** *137*, 13740-13743.

40. Clough, A. J.; Yoo, J. W.; Mecklenburg, M. H.; Marinescu, S. C., Two-Dimensional Metal–Organic Surfaces for Efficient Hydrogen Evolution from Water. *Journal of the American Chemical Society* **2015,** *137*, 118-121.

41. Downes, C. A.; Marinescu, S. C., One dimensional metal dithiolene (M = Ni, Fe, Zn) coordination polymers for the hydrogen evolution reaction. *Dalton Transactions* **2016,** *45*, 19311-19321.

42. Downes, C. A.; Marinescu, S. C., Bioinspired Metal Selenolate Polymers with Tunable Mechanistic Pathways for Efficient H2 Evolution. *ACS Catalysis* **2017,** *7*, 848-854.

43. Downes, C. A.; Yoo, J. W.; Orchanian, N. M.; Haiges, R.; Marinescu, S. C., H2 evolution by a cobalt selenolate electrocatalyst and related mechanistic studies. *Chemical Communications* **2017,** *53*, 7306-7309.

44. Downes, C. A.; Marinescu, S. C., Understanding Variability in the Hydrogen Evolution Activity of a Cobalt Anthracenetetrathiolate Coordination Polymer. *ACS Catalysis* **2017,** *7*, 8605-8612.

45. Seo, J.; Pekarek, R. T.; Rose, M. J., Photoelectrochemical operation of a surface-bound, nickel-phosphine H2 evolution catalyst on p-Si(111): a molecular semiconductor|catalyst construct. *Chemical Communications* **2015,** *51*, 13264-13267.

46. Liu, F.; Cardolaccia, T.; Hornstein, B. J.; Schoonover, J. R.; Meyer, T. J., Electrochemical Oxidation of Water by an Adsorbed μ-Oxo-Bridged Ru Complex. *Journal of the American Chemical Society* **2007,** *129*, 2446-2447.

47. Jurss, J. W.; Concepcion, J. C.; Norris, M. R.; Templeton, J. L.; Meyer, T. J., Surface Catalysis of Water Oxidation by the Blue Ruthenium Dimer. *Inorganic Chemistry* **2010,** *49*, 3980-3982.

48. Chen, Z.; Concepcion, J. J.; Hull, J. F.; Hoertz, P. G.; Meyer, T. J., Catalytic water oxidation on derivatized nanoITO. *Dalton Transactions* **2010,** *39*, 6950-6952.

49. Li, F.; Zhang, B.; Li, X.; Jiang, Y.; Chen, L.; Li, Y.; Sun, L., Highly Efficient Oxidation of Water by a Molecular Catalyst Immobilized on Carbon Nanotubes. *Angewandte Chemie International Edition* **2011,** *50*, 12276-12279.

50. Sheehan, S. W.; Thomsen, J. M.; Hintermair, U.; Crabtree, R. H.; Brudvig, G. W.; Schmuttenmaer, C. A., A molecular catalyst for water oxidation that binds to metal oxide surfaces. *Nature Communications* **2015,** *6*, 6469.

51. Creus, J.; Matheu, R.; Peñafiel, I.; Moonshiram, D.; Blondeau, P.; Benet-Buchholz, J.; García-Antón, J.; Sala, X.; Godard, C.; Llobet, A., A Million Turnover Molecular Anode for Catalytic Water Oxidation. *Angewandte Chemie International Edition* **2016,** *55*, 15382-15386.

52. Matheu, R.; Moreno-Hernandez, I. A.; Sala, X.; Gray, H. B.; Brunschwig, B. S.; Llobet, A.; Lewis, N. S., Photoelectrochemical Behavior of a Molecular Ru-Based Water-Oxidation Catalyst Bound to TiO2-Protected Si Photoanodes. *Journal of the American Chemical Society* **2017,** *139*, 11345-11348.

53. Demeter, E. L.; Hilburg, S. L.; Washburn, N. R.; Collins, T. J.; Kitchin, J. R., Electrocatalytic Oxygen Evolution with an Immobilized TAML Activator. *Journal of the American Chemical Society* **2014,** *136*, 5603-5606.

54. Joya, K. S.; Morlanés, N.; Maloney, E.; Rodionov, V.; Takanabe, K., Immobilization of a molecular cobalt electrocatalyst by hydrophobic interaction with a hematite photoanode for highly stable oxygen evolution. *Chemical Communications* **2015,** *51*, 13481-13484.

55. Öztaş, B.; Akyüz, D.; Koca, A., Immobilization of alkynyl functionalized manganese phthalocyanine via click electrochemistry for electrocatalytic oxygen evolution reaction. *Physical Chemistry Chemical Physics* **2017,** *19*, 26121-26131.

56. Hutchison, J. E.; Postlethwaite, T. A.; Murray, R. W., Molecular films of thiol-derivatized tetraphenylporphyrins on gold: film formation and electrocatalytic dioxygen reduction. *Langmuir* **1993,** *9*, 3277-3283.

57. Lei, H.; Liu, C.; Wang, Z.; Zhang, Z.; Zhang, M.; Chang, X.; Zhang, W.; Cao, R., Noncovalent Immobilization of a Pyrene-Modified Cobalt Corrole on Carbon Supports for Enhanced Electrocatalytic Oxygen Reduction and Oxygen Evolution in Aqueous Solutions. *ACS Catalysis* **2016,** *6*, 6429-6437.

58. Cai, C. X.; Xue, K. H.; Xu, X. Y.; Luo, Q. H., Electrocatalysis for the reduction of O2 and H2O2 based on complex of copper(II) with the tris(3-aminopropyl)amine and imidazole ligands. *Journal of Applied Electrochemistry* **1997,** *27*, 793-798.

59. Collman, J. P.; Marrocco, M.; Denisevich, P.; Koval, C.; Anson, F. C., Potent catalysis of the electroreduction of oxygen to water by dicobalt porphyrin dimers adsorbed on graphite electrodes. *Journal of Electroanalytical Chemistry and Interfacial Electrochemistry* **1979,** *101*, 117-122.

60. Lei, Y.; Anson, F. C., Mechanistic aspects of the electroreduction of dioxygen as catalyzed by copper-phenanthroline complexes adsorbed on graphite electrodes. *Inorganic Chemistry* **1994,** *33*, 5003-5009.

61. McCrory, C. C. L.; Devadoss, A.; Ottenwaelder, X.; Lowe, R. D.; Stack, T. D. P.; Chidsey, C. E. D., Electrocatalytic O2 Reduction by Covalently Immobilized Mononuclear Copper(I) Complexes: Evidence for a Binuclear Cu2O2 Intermediate. *Journal of the American Chemical Society* **2011,** *133*, 3696-3699.

62. Xi, Y.-T.; Wei, P.-J.; Wang, R.-C.; Liu, J.-G., Bio-inspired multinuclear copper complexes covalently immobilized on reduced graphene oxide as efficient electrocatalysts for the oxygen reduction reaction. *Chemical Communications* **2015,** *51*, 7455-7458.

63. Mukherjee, S.; Mukherjee, A.; Bhagi-Damodaran, A.; Mukherjee, M.; Lu, Y.; Dey, A., A biosynthetic model of cytochrome c oxidase as an electrocatalyst for oxygen reduction. *Nature Communications* **2015,** *6*, 8467.

64. Wang, R.-C.; Yin, T.-L.; Wei, P.-J.; Liu, J.-G., A copper complex covalently grafted on carbon nanotubes and reduced graphene oxide promotes oxygen reduction reaction activity and catalyst stability. *RSC Advances* **2015,** *5*, 66487-66493.

65. Rosser, T. E.; Windle, C. D.; Reisner, E., Electrocatalytic and Solar-Driven CO2 Reduction to CO with a Molecular Manganese Catalyst Immobilized on Mesoporous TiO2. *Angewandte Chemie International Edition* **2016,** *55*, 7388-7392.

66. Reuillard, B.; Ly, K. H.; Rosser, T. E.; Kuehnel, M. F.; Zebger, I.; Reisner, E., Tuning Product Selectivity for Aqueous CO2 Reduction with a Mn(bipyridine)-pyrene Catalyst Immobilized on a Carbon Nanotube Electrode. *Journal of the American Chemical Society* **2017,** *139*, 14425-14435.

67. Zhanaidarova, A.; Jones, S. C.; Despagnet-Ayoub, E.; Pimentel, B. R.; Kubiak, C. P., Re(tBu-bpy)(CO)3Cl Supported on Multi-Walled Carbon Nanotubes Selectively Reduces CO2 in Water. *Journal of the American Chemical Society* **2019**.

68. Maurin, A.; Robert, M., Noncovalent Immobilization of a Molecular Iron-Based Electrocatalyst on Carbon Electrodes for Selective, Efficient CO2-to-CO Conversion in Water. *Journal of the American Chemical Society* **2016,** *138*, 2492-2495.

69. Orchanian, N. M.; Hong, L. E.; Marinescu, S. C., Immobilized Molecular Wires on Carbon-Cloth Electrodes Facilitate CO2 Electrolysis. *ACS Catalysis* **2019,** *9*, 9393-9397.

70. Orchanian, N. M.; Hong, L. E.; Skrainka, J. A.; Esterhuizen, J. A.; Popov, D. A.; Marinescu, S. C., Surface-Immobilized Conjugated Polymers Incorporating Rhenium Bipyridine Motifs for Electrocatalytic and Photocatalytic CO2 Reduction. *ACS Applied Energy Materials* **2019,** *2*, 110-123.

71. Popov, D. A.; Luna, J. M.; Orchanian, N. M.; Haiges, R.; Downes, C. A.; Marinescu, S. C., A 2,2′-bipyridine-containing covalent organic framework bearing rhenium(i) tricarbonyl moieties for CO2 reduction. *Dalton Transactions* **2018,** *47*, 17450-17460.

72. Johnson, E. M.; Haiges, R.; Marinescu, S. C., Covalent-Organic Frameworks Composed of Rhenium Bipyridine and Metal Porphyrins: Designing Heterobimetallic Frameworks with Two Distinct Metal Sites. *ACS Applied Materials & Interfaces* **2018,** *10*, 37919-37927.

73. Kang, P.; Zhang, S.; Meyer, T. J.; Brookhart, M., Rapid Selective Electrocatalytic Reduction of Carbon Dioxide to Formate by an Iridium Pincer Catalyst Immobilized on Carbon Nanotube Electrodes. *Angewandte Chemie International Edition* **2014,** *53*, 8709-8713.

74. Das, A.; Stahl, S. S., Noncovalent Immobilization of Molecular Electrocatalysts for Chemical Synthesis: Efficient Electrochemical Alcohol Oxidation with a Pyrene–TEMPO Conjugate. *Angewandte Chemie International Edition* **2017,** *56*, 8892-8897.

75. Gratzel, M., Photoelectrochemical cells. *Nature* **2001,** *414*, 338-344.

76. Li, Z.; Luo, W.; Zhang, M.; Feng, J.; Zou, Z., Photoelectrochemical cells for solar hydrogen production: current state of promising photoelectrodes, methods to improve their properties, and outlook. *Energy & Environmental Science* **2013,** *6*, 347-370.

77. Jacobsson, T. J.; Fjällström, V.; Edoff, M.; Edvinsson, T., Sustainable solar hydrogen production: from photoelectrochemical cells to PV-electrolyzers and back again. *Energy & Environmental Science* **2014,** *7*, 2056-2070.

78. Li, J.; Wu, N., Semiconductor-based photocatalysts and photoelectrochemical cells for solar fuel generation: a review. *Catalysis Science & Technology* **2015,** *5*, 1360-1384.

79. Walter, M. G.; Warren, E. L.; McKone, J. R.; Boettcher, S. W.; Mi, Q.; Santori, E. A.; Lewis, N. S., Solar Water Splitting Cells. *Chemical Reviews* **2010,** *110*, 6446-6473.

80. Vericat, C.; Vela, M. E.; Corthey, G.; Pensa, E.; Cortes, E.; Fonticelli, M. H.; Ibanez, F.; Benitez, G. E.; Carro, P.; Salvarezza, R. C., Self-assembled monolayers of thiolates on metals: a review article on sulfur-metal chemistry and surface structures. *RSC Advances* **2014,** *4*, 27730-27754.

81. Chaki, N. K.; Vijayamohanan, K., Self-assembled monolayers as a tunable platform for biosensor applications. *Biosensors and Bioelectronics* **2002,** *17*, 1-12.

82. Wang, Y.; Zhou, Y.; Sokolov, J.; Rigas, B.; Levon, K.; Rafailovich, M., A potentiometric protein sensor built with surface molecular imprinting method. *Biosensors and Bioelectronics* **2008,** *24*, 162-166.

83. O'Leary, L. E.; Johansson, E.; Brunschwig, B. S.; Lewis, N. S., Synthesis and Characterization of Mixed Methyl/Allyl Monolayers on Si(111). *The Journal of Physical Chemistry B* **2010,** *114*, 14298-14302.

84. Lattimer, J. R. C.; Brunschwig, B. S.; Lewis, N. S.; Gray, H. B., Redox Properties of Mixed Methyl/Vinylferrocenyl Monolayers on Si(111) Surfaces. *The Journal of Physical Chemistry C* **2013,** *117*, 27012-27022.

85. Lattimer, J. R. C.; Blakemore, J. D.; Sattler, W.; Gul, S.; Chatterjee, R.; Yachandra, V. K.; Yano, J.; Brunschwig, B. S.; Lewis, N. S.; Gray, H. B., Assembly, characterization, and electrochemical properties of immobilized metal bipyridyl complexes on silicon(111) surfaces. *Dalton Transactions* **2014,** *43*, 15004-15012.

86. Johansson, E.; Boettcher, S. W.; O'Leary, L. E.; Poletayev, A. D.; Maldonado, S.; Brunschwig, B. S.; Lewis, N. S., Control of the pH-Dependence of the Band Edges of Si(111) Surfaces Using Mixed Methyl/Allyl Monolayers. *The Journal of Physical Chemistry C* **2011,** *115*, 8594-8601.

87. Seo, J.; Kim, H. J.; Pekarek, R. T.; Rose, M. J., Hybrid Organic/Inorganic Band-Edge Modulation of p-Si(111) Photoelectrodes: Effects of R, Metal Oxide, and Pt on H2 Generation. *Journal of the American Chemical Society* **2015,** *137*, 3173-3176.

88. Zhao, Y.; Anderson, N. C.; Zhu, K.; Aguiar, J. A.; Seabold, J. A.; Lagemaat, J. v. d.; Branz, H. M.; Neale, N. R.; Oh, J., Oxidatively Stable Nanoporous Silicon Photocathodes with Enhanced Onset Voltage for Photoelectrochemical Proton Reduction. *Nano Letters* **2015,** *15*, 2517-2525.

89. Gu, J.; Yan, Y.; Young, J. L.; Steirer, K. X.; Neale, N. R.; Turner, J. A., Water reduction by a p-GaInP2 photoelectrode stabilized by an amorphous TiO2 coating and a molecular cobalt catalyst. *Nature Materials* **2015,** *15*, 456-460.

90. Aguiar, J. A.; Anderson, N. C.; Neale, N. R., Revealing the semiconductor–catalyst interface in buried platinum black silicon photocathodes. *Journal of Materials Chemistry A* **2016,** *4*, 8123-8129.

91. Anderson, N. C.; Carroll, G. M.; Pekarek, R. T.; Christensen, S. T.; van de Lagemaat, J.; Neale, N. R., Silicon Photoelectrode Thermodynamics and Hydrogen Evolution Kinetics Measured by Intensity-Modulated High-Frequency Resistivity Impedance Spectroscopy. *The Journal of Physical Chemistry Letters* **2017,** *8*, 5253-5258.

92. Sun, K.; Shen, S.; Liang, Y.; Burrows, P. E.; Mao, S. S.; Wang, D., Enabling Silicon for Solar-Fuel Production. *Chemical Reviews* **2014,** *114*, 8662-8719.

93. Brown, A. P.; Koval, C.; Anson, F. C., Illustrative electrochemical behavior of reactants irreversibly adsorbed on graphite electrode surfaces. *Journal of Electroanalytical Chemistry and Interfacial Electrochemistry* **1976,** *72*, 379-387.

94. Chen, R. J.; Zhang, Y.; Wang, D.; Dai, H., Noncovalent Sidewall Functionalization of Single-Walled Carbon Nanotubes for Protein Immobilization. *Journal of the American Chemical Society* **2001,** *123*, 3838-3839.

95. Katz, E., Application of bifunctional reagents for immobilization of proteins on a carbon electrode surface: Oriented immobilization of photosynthetic reaction centers. *Journal of Electroanalytical Chemistry* **1994,** *365*, 157-164.

96. Mann, J. A.; Rodríguez-López, J.; Abruña, H. D.; Dichtel, W. R., Multivalent Binding Motifs for the Noncovalent Functionalization of Graphene. *Journal of the American Chemical Society* **2011,** *133*, 17614-17617.

97. Rodríguez-López, J.; Ritzert, N. L.; Mann, J. A.; Tan, C.; Dichtel, W. R.; Abruña, H. D., Quantification of the Surface Diffusion of Tripodal Binding Motifs on Graphene Using Scanning Electrochemical Microscopy. *Journal of the American Chemical Society* **2012,** *134*, 6224-6236.

98. Kohmoto, M.; Ozawa, H.; Yang, L.; Hagio, T.; Matsunaga, M.; Haga, M.-a., Controlling the Adsorption of Ruthenium Complexes on Carbon Surfaces through Noncovalent Bonding with Pyrene Anchors: An Electrochemical Study. *Langmuir* **2016,** *32*, 4141-4152.

99. Ozawa, H.; Katori, N.; Kita, T.; Oka, S.; Haga, M.-a., Controlling the Molecular Direction of Dinuclear Ruthenium Complexes on HOPG Surface through Noncovalent Bonding. *Langmuir* **2017,** *33*, 11901-11910.

100. Lydon, B. R.; Germann, A.; Yang, J. Y., Chemical modification of gold electrodes via non-covalent interactions. *Inorg. Chem. Front.* **2016,** *3*, 836-841.

CHAPTER 2

Interfacial Electron Transfer of Ferrocene Immobilized onto Indium Tin Oxide Through Covalent and Non-Covalent Interactions

Portions of this chapter have been published:

Hanna. C. M.; Sanborn, C. D.; Ardo, S.; Yang, J. Y. *ACS Appl. Mater. Interfaces,* **2018**, *10*, 13211.

2.1 Introduction

The attachment of molecular species to electrode surfaces is a route to the synthesis of materials with atomic specificity. Two different methods are traditionally used to attach molecules to electrodes: covalent and non-covalent attachment. The first utilizes covalent bonds between the molecule and the electrode.[1-2] This method requires that the molecular species is compatible with the functional groups (e.g. Grignard,[3-4] thiol,[5-6] diamine,[7-9] or vinyl)[5, 10-11] used to forge covalent bonds to the surface. The second approach is to functionalize the molecular species with inert pyrene functionalities and utilize π-π interactions for physisorption onto graphitic electrodes such as highly-oriented pyrolytic graphite (HOPG), carbon nanotubes, or graphene.[7, 12-17] Covalent attachment limits the scope of molecular species that can be immobilized onto surfaces while non-covalent attachment through π-π interactions is restricted to electrodes with graphitic character.

The Yang group recently developed a synthetically facile approach to molecular immobilization onto electrode surfaces that broadens the scope of molecularly modified electrodes. Pyrene molecules, which are easily functionalized and stable to a large range of reactive functional groups, are covalently attached to non-graphitic surfaces. Pyrene-appended redox-active molecules are then physisorbed onto these surfaces through non-covalent interactions. This method was previously applied in the Yang lab towards the non-covalent immobilization of 1-pyrenylferrocene to gold and exhibited facile electron transfer between the gold electrode and immobilized ferrocene.[18] To demonstrate the generality of this non-covalent attachment technique, 1-pyrenylferrocene is physisorbed onto pyrene-appended indium tin oxide (ITO) and characterized both spectroscopically and electrochemically (Scheme 2.1A). The electrochemical properties of

ITO|Pyr|Pyrenylferrocene is then compared to an analogous covalent system where ferrocene is covalently attached to ITO (ITO|Vinylferrocene, Scheme 2.1B).

Scheme 2.1. Pictorial representation of the attachment of ferrocene to indium tin oxide (ITO) through (A) non-covalent and (B) covalent interactions.

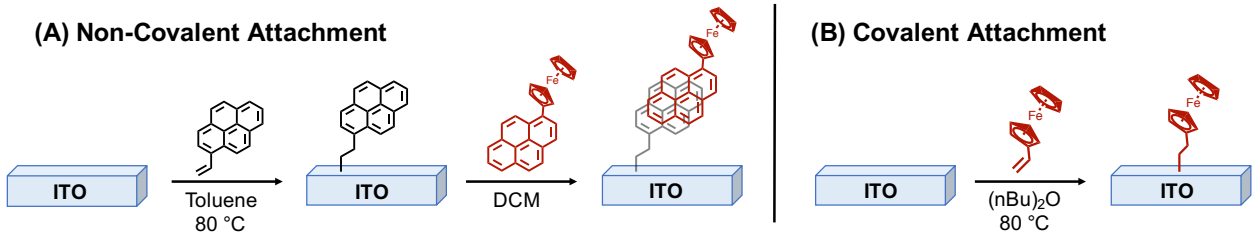

2.2 Results and Discussion

2.2.1 Modification of ITO Surfaces

1-Vinylpyrene[19] and 1-pyrenylferrocene[18] were prepared using previously published procedures. Covalent attachment of pyrene and ferrocene to ITO was achieved by immersing freshly cleaned, unmodified ITO samples in toluene solutions of 1-vinylpyrene or $(nBu)_2O$ solutions of vinylferrocene at 80 °C for 24 hours to yield pyrene-modified ITO (ITO|Pyr) and ferrocene-modified ITO (ITO|Vinylferrocene). Recent studies on the attachment of alkenes and alkynes to hydroxyl-terminated metal oxide surfaces using heat found that a thermal approach leads to covalently bound monolayers as opposed to polymerized multilayers.[20] 1-vinylpyrene and vinylferrocene are therefore expected to be bound to the surface in a covalently bound monolayer or sub-monolayer as opposed to a thick polymer. Finally, 1-pyrenylferrocene was physisorbed to the ITO|Pyr surface by soaking ITO|Pyr samples in a 1 mM CH_2Cl_2 solution of the metal complex for 12 hours followed by rinsing with CH_3CN, a solvent in which the free complex is soluble, resulting in ITO|Pyr non-covalently modified with 1-pyrenylferrocene (ITO|Pyr|Pyrenylferrocene).

2.2.2 Contact Angle Measurements

Static contact angles were measured between unmodified ITO and ITO|Pyr and a droplet of deionized H_2O in order to probe changes in hydrophobicity upon covalent modification of ITO with pyrene. Optical photographs of the contacts between a H_2O droplet and freshly cleaned, unmodified ITO and ITO|Pyr are shown in Figure 2.1. Unmodified ITO displays hydrophilic character with a wetting contact angle (θ_c) of 19°. Covalent functionalization of ITO with 1-vinylpyrene results in a significant increase in θ_c to 44°. The increase in θ_c upon modification of ITO indicates an increase in hydrophobicity consistent with the attachment of pyrene to the surface. Several studies on the preparation of alkyl self-assembled monolayers (SAMs) on metal oxide surfaces using vinyl functionalities report contact angles greater than 85° upon SAM formation at the electrode.[20-22] Comparison of θ_c of ITO|Pyr to the previously reported contact angles suggest the pyrene monolayer on ITO is less dense than the alkyl monolayers that have θ_c greater than 85°. This discrepancy in monolayer density is likely due to the large size of pyrene (relative to alkyl chains) which hinders close-packed monolayer formation.

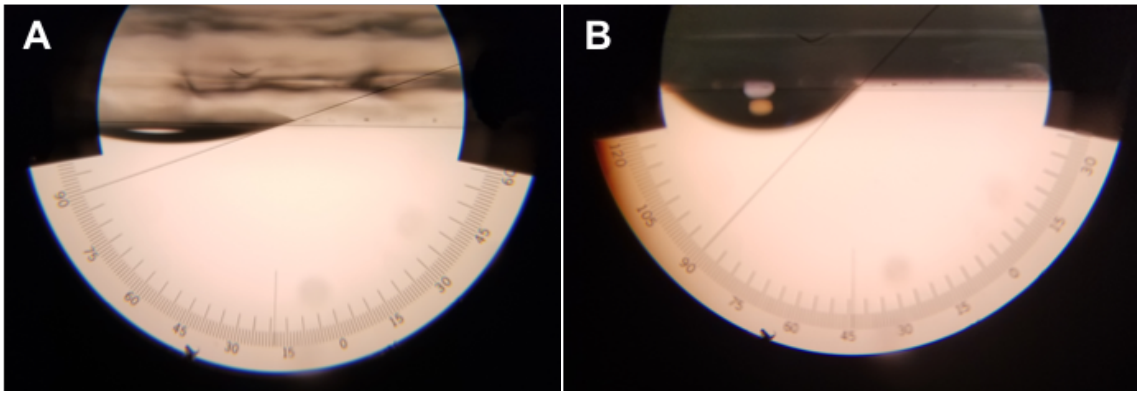

Figure 2.1 Optical photographs of contacts between a H_2O droplet and (A) freshly cleaned, unmodified ITO and (B) ITO|Pyr.

2.2.3 Fluorescence Spectroscopy

Fluorescence emission spectroscopy was used to further confirm the attachment of 1-vinylpyrene to the ITO surface and provide evidence for the non-covalent interactions between pyrene molecules on the surface. The fluorescence emission spectrum of ITO|Pyr, displayed in black in Figure 2.2, exhibits a broad emission band with a maximum at 440 nm. This broad feature is attributed to the emission of the face-to-face excimer of pyrene which is commonly observed in the emission spectra of bipyrenyl compounds and highly concentrated pyrene solutions.[23-24] The spectrum agrees with literature reports of the fluorescence of pyrene and 1-vinylpyrene adsorbed on oxide supports,[25-26] confirming the presence of pyrene on the surface and indicating that the pyrene molecules are oriented on the surface in a way that promotes face-to-face excimer formation upon excitation. The fluorescence emission spectrum of ITO|Pyr|Pyrenylferrocene is shown in blue in Figure 2.2. There are no significant differences between the emission spectrum of ITO|Pyr and ITO|Pyr|Pyrenylferrocene suggesting that the pyrene molecules are still oriented in a face-to-face manner but failing to provide further information about the π-π interactions at the surface.

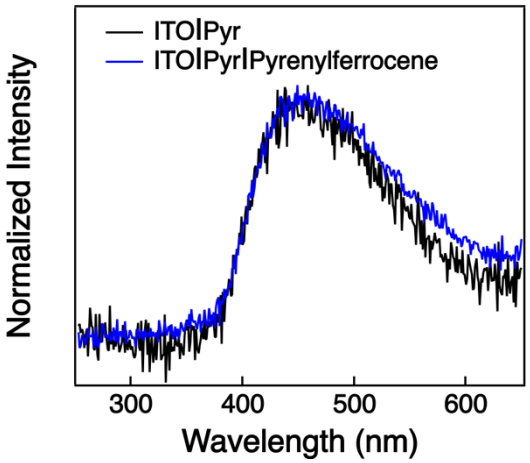

Figure 2.2 Two-photon fluorescence emission spectra of ITO|Pyr (black trace) and ITO|Pyr|Pyrenylferrocene (blue trace).

2.2.4 X-Ray Photoelectron Spectroscopy (XPS)

The XPS survey spectra of unmodified ITO, ITO|Pyr, ITO|Pyr|Pyrenylferrocene, and ITO|Vinylferrocene are shown in Figure 2.3. All four spectra exhibit the expected peaks from indium, tin, oxygen, and carbon. Upon functionalization of ITO with 1-vinylpyrene, there are no changes to the XPS spectrum other than an increase in the C 1s signal. This is expected due to the lack of XPS signatures present in 1-vinylpyrene. Physisorption of 1-pyrenylferrocene onto the ITO|Pyr surface or covalent attachment of vinylferrocene onto ITO results in the appearance of Fe $2p_{3/2}$ peaks at 708 eV and Fe $2p_{1/2}$ peaks at 721 eV (high resolution spectra shown in Figure 2.4), confirming the presence of ferrocene on the covalently modified and non-covalently modified surfaces. In both high-resolution spectra, the Fe 2p peaks exhibit a 2:1 branching ratio expected for Fe 2p photoelectrons. The peaks at 704 eV and 717 eV are attributed to In $3p_{1/2}$ and Sn $3p_{3/2}$, respectively. The high-resolution XPS spectra of the Fe 2p region of unmodified ITO and ITO|Pyr exhibit peaks attributed to In

$3p_{1/2}$ and Sn $3p_{3/2}$, but do not display any Fe 2p features (Figure 2.4). These results confirm the presence of 1-pyrenylferrocene on the ITO|Pyr|Pyrenylferrocene surface.

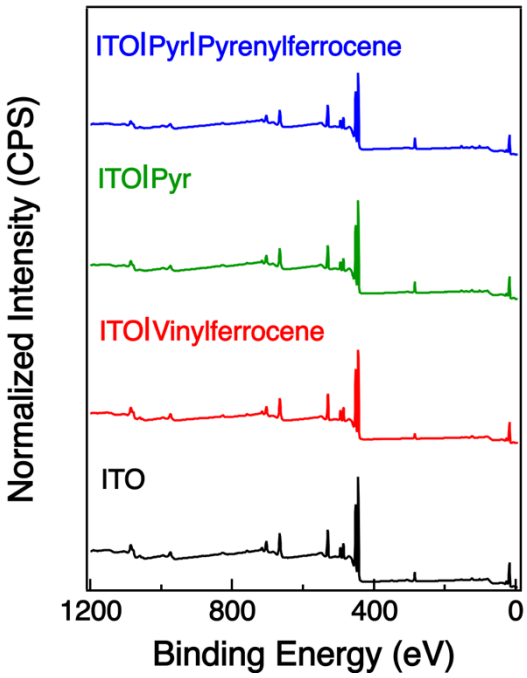

Figure 2.3. XPS survey spectra of ITO, ITO|Pyr, ITO|Pyr|Pyrenylferrocene, and ITO|Vinylferrocene.

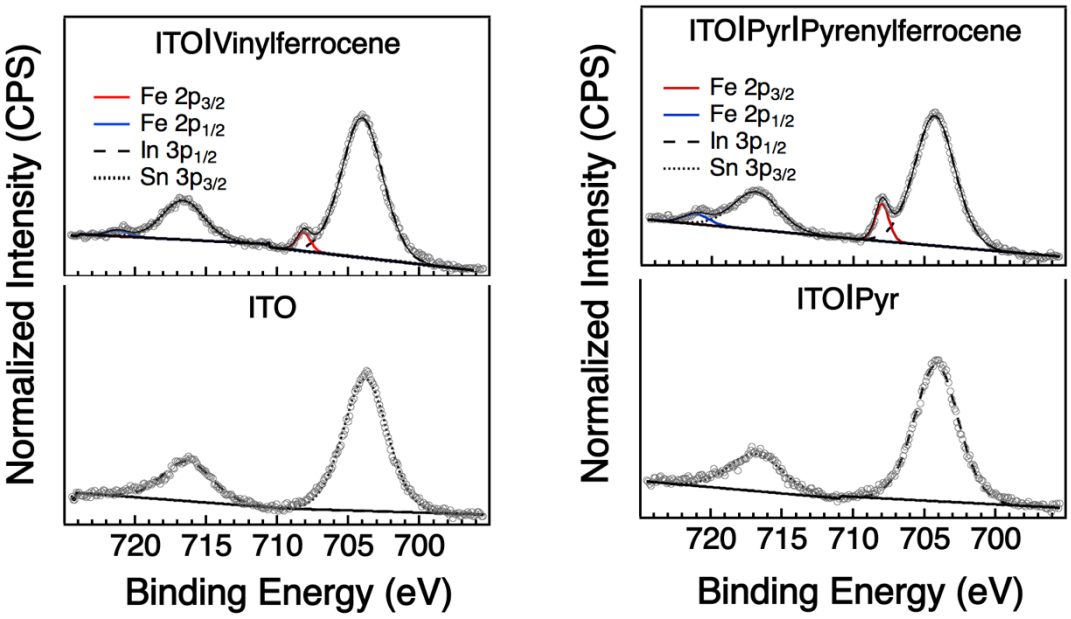

Figure 2.4. High resolution XPS spectra of the Fe 2p region of ITO, ITO|Pyr, ITO|Pyr|Pyrenylferrocene, and ITO|Vinylferrocene.

2.2.5 Cyclic Voltammetry of Modified Electrodes

Cyclic voltammetry of ITO|Pyr|Pyrenylferrocene was performed to probe electron transfer between the ITO electrode and surface-bound ferrocene. The cyclic voltammogram (CV) of ITO|Pyr|Pyrenylferrocene in 100 mM aqueous solution of KCl displays a reversible redox couple at 0.46 V vs SCE with a full width at half maximum (FWHM) of 0.16 V and peak separation of 0.04 V (Figure 2.5, blue trace). The FWHM is greater than the ideal value of 0.09 V, suggesting electrostatic interaction between neighboring ferrocene complexes.[27-28] The cathodic to anodic peak separation also deviates from an ideal value of 0 V, which is likely due to both the electrostatic interaction between neighboring ferrocene molecules and slow electron transfer kinetics.[28-29] The $E_{1/2}$ value observed is consistent with literature reports of surface-bound ferrocene.[18, 29]

In order to understand the importance of the surface-bound pyrene in immobilization of 1-pyrenylferrocene, an unmodified ITO sample was soaked in 1-pyrenylferrocene under the same conditions as 1-pyrenylferrocene attachment to ITO|Pyr. The CV of this sample does not display the $Cp_2Fe^{+/0}$ (Cp = cyclopentadienyl) couple, indicating that the pyrene layer is necessary for successful attachment of 1-pyrenylferrocene to the surface. Furthermore, no redox events are observed between 0.00 and 0.70 V vs SCE for unmodified ITO or ITO|Pyr (Figure 2.5), confirming that the redox event at 0.46 V vs SCE in the CV of ITO|Pyr|Pyrenylferrocene is correctly assigned as $Cp_2Fe^{+/0}$.

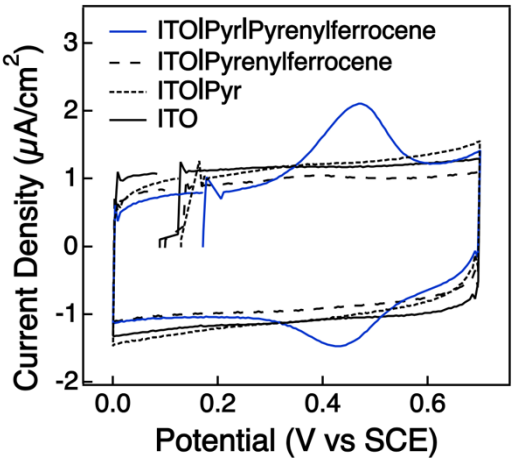

Figure 2.5. Cyclic voltammetry of ITO|Pyr|Pyrenylferrocene, ITO|Pyr, ITO, and ITO treated with 1-pyrenylferrocene performed in 100 mM KCl at 100 mV/s.

Variable scan rate CVs for ITO|Pyr|Pyrenylferrocene and the corresponding peak current density vs scan rate plot is shown in Figure 2.6. Peak current densities vary linearly with scan rate, diagnostic of a surface-bound redox species. Integration of the anodic faradaic current was used to calculate the electrochemically-active coverage of 1-pyrenylferrocene on the ITO|Pyr surface. The average electrochemically-active surface coverage across all samples was calculated to be 5 pmol/cm^2. Attempts to increase the coverage by extending sample immersion time and using highly concentrated solutions of 1-pyrenylferrocene during sample preparation were unsuccessful.

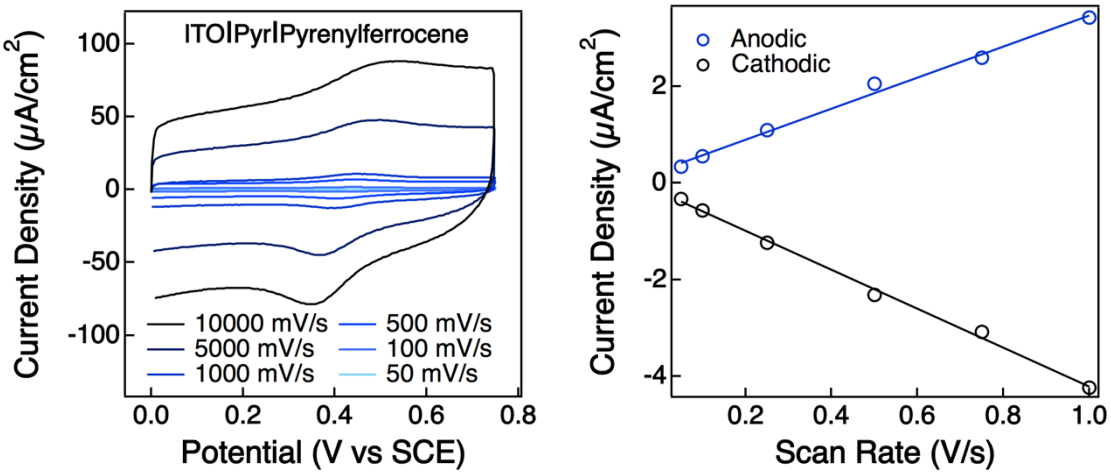

Figure 2.6. Variable scan rate cyclic voltammetry (left) and corresponding current density vs scan rate plot (right) of ITO|Pyr|Pyrenylferrocene performed in 100 mM KCl.

Finally, the CVs of ITO|Vinylferrocene display a reversible redox couple at 0.34 V vs SCE with a FWHM of 0.32 V (Figure 2.7). As exhibited in the CV of non-covalently bound ferrocene, the FWHM is greater than the ideal value of 0.09 V, suggesting electrostatic interaction between neighboring ferrocene groups.[27-28] The deviation of the FWHM of the ITO|Vinylferrocene system from ideality is greater than that of the ITO|Pyr|Pyrenylferrocene system, indicating greater interaction between the ferrocene centers in the covalent attachment system.[30] Integration of the anodic faradaic current was used to calculate the electrochemically-active coverage of vinylferrocene on the ITO surface. The average electrochemically-active surface coverage across all samples was calculated to be 30 pmol/cm^2, six times greater than that of non-covalently bound 1-pyrenylferrocene. The variable scan rate CVs of this system and the corresponding current density vs scan rate plot (Figure 2.7) display a linear relationship between current density and scan rate, confirming ferrocene is bound to the surface.

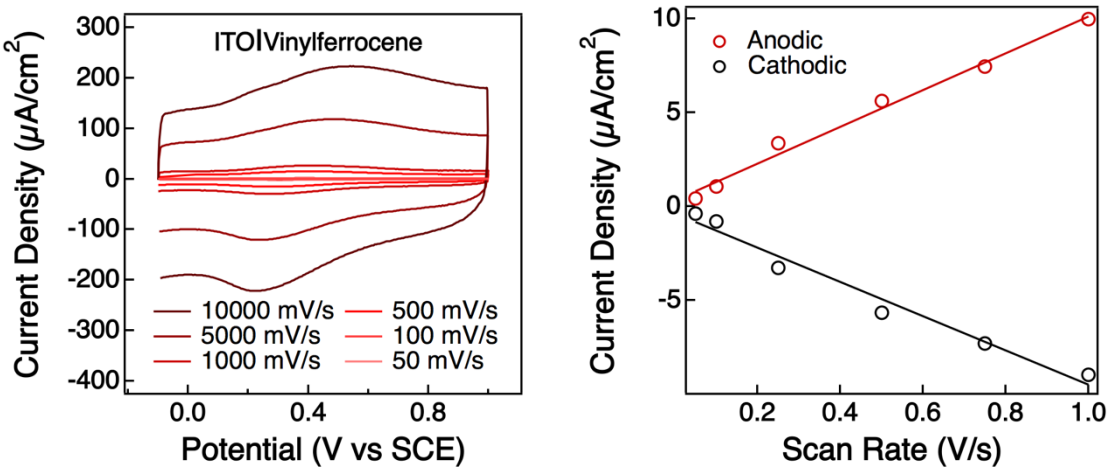

Figure 2.7. Variable scan rate cyclic voltammetry (left) and corresponding current density vs scan rate plot (right) of ITO|Vinylferrocene performed in 100 mM KCl.

2.2.6 Electron Transfer Kinetics

The rate of electron transfer between the electrode and immobilized ferrocene was determined using the Butler-Volmer approach.[30] The separation of anodic and cathodic peaks with increasing scan rate observed in Figure 2.6 and Figure 2.7 can be used to calculate the apparent rate constant of the system according to the Laviron Formalism[30] using the following set of equations:

$$E_{p,c} = E^{\circ\prime} - \frac{2.3\mathrm{RT}}{\alpha nF}\log\left[\frac{\alpha nF v_c}{RTk_{app}}\right] \qquad (2.1)$$

$$E_{p,a} = E^{\circ\prime} - \frac{2.3\mathrm{RT}}{(1-\alpha)nF}\log\left[\frac{(1-\alpha)nF v_a}{RTk_{app}}\right] \qquad (2.2)$$

where $E_{p,a}$ is the potential of the anodic peak, $E_{p,c}$ is the potential of the cathodic peak, E°' is the formal potential calculated by averaging the anodic and cathodic potentials at slow scan rates, v_a and v_c are the critical scan rates, α is the electron transfer coefficient, k_{app} is the apparent rate constant, R is the ideal gas constant, T is the absolute temperature, F is the Faraday constant, and n is the number of electrons transferred. Electron transfer parameters

(v_a, v_c, α, and k_{app}) are determined by plotting $E_p - E°'$ against the log of the scan rate (trumpet plot). v_a and v_c are determined by extrapolating the linear portions of the plot where ($E_p - E°'$) > 100 mV to 0 and α is obtained from the slopes of the linear fits. k_{app} is calculated using v_a, v_c, and α and is reported as the average of $k_{app,c}$ and $k_{app,a}$ across three individually prepared samples.

The trumpet plot for ITO|Pyr|Pyrenylferrocene is displayed in Figure 2.8 (left). Using the slopes of the linear portions of the trumpet plot, the electron transfer coefficients, α and (1–α), were calculated to be 0.44 and 0.26, respectively. The transfer coefficients calculated for the ITO|Pyr|Pyrenylferrocene system deviate from 0.5 and do not have a unity sum, both of which are expected for a one electron redox process. Similar deviations are exhibited in literature reports of surface-bound ferrocene, where α and (1–α) are 0.23 and 0.24, respectively.[31] These low transfer coefficients with a non-unity sum suggest a film structure with exposed ITO sites.[31-32] k_{app} for the ITO|Pyr|Pyrenylferrocene system was determined to be 100 ± 8 s^{-1}. This rate constant is two orders of magnitude greater than the electron transfer rate constant reported for ferrocene dicarboxylic acid adsorbed on ITO surfaces (0.2–0.8 s^{-1})[33] but is very similar to the electron transfer rate constant for pyrene-appended ruthenium complexes immobilized on HOPG through π-π interactions (64–110 s^{-1}).[34] These results suggest that the electrochemical behavior of ITO|Pyr|Pyrenylferrocene is similar to that of analogous π-π stacking interfaces on aromatic electrodes.

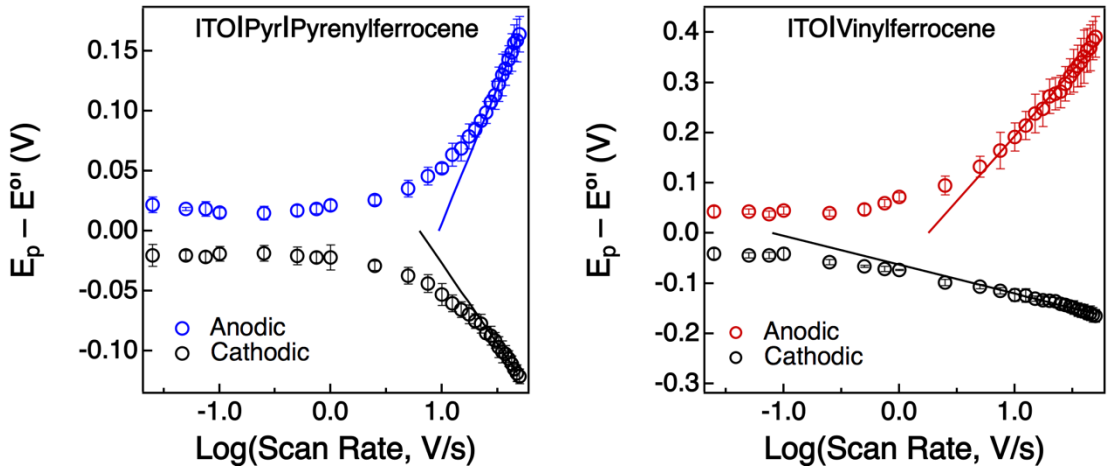

Figure 2.8. Trumpet plots for ITO|Pyr|Pyrenylferrocene (left) and ITO|Vinylferrocene (right).

The trumpet plot for the ITO|Vinylferrocene system is displayed in Figure 2.8 (right). The transfer coefficients, α and (1–α), were calculated to be 0.71 and 0.23, respectively. The increase in transfer coefficient values and their near-unity sum compared to those of ITO|Pyr|Pyrenylferrocene suggest a film structure with fewer exposed ITO sites in the ITO|Vinylferrocene system, consistent with the increased electrochemically-active ferrocene coverage exhibited in ITO|Vinylferrocene.[31] The rate constant, k_{app}, was calculated to be 9 ± 2 s^{-1}. These results indicate that the apparent rate of electron transfer of the non-covalent ITO|Pyr|Pyrenylferrocene system is about ten times greater than that of the covalent ITO|Vinylferrocene system. In order to ensure that the slow electron transfer across the ITO|Vinylferrocene interface relative to ITO|Pyr|Pyrenylferrocene was not a consequence of higher surface coverage, low-coverage ITO|Vinylferrocene samples were prepared with an average electrochemically-active ferrocene coverage of 7 pmol/cm^2. The k_{app} for low-coverage ITO|Vinylferrocene was calculated using the Laviron formalism to be 10 ± 2 s^{-1}, identical to the electron-transfer rate constant for high-coverage ITO|Vinylferrocene. This

result confirms that surface coverage is not the source of slow electron transfer for ITO|Vinylferrocene.

A notable difference between the trumpet plots of ITO|Pyr|Pyrenylferrocene and ITO|Vinylferrocene is the symmetry of the anodic and cathodic portions of the plots (present for both high and low coverage ITO|Vinylferrocene). According to initial theoretical investigations by Laviron, the asymmetry exhibited in the trumpet plot of ITO|Vinylferrocene is a consequence of transfer coefficient values exceeding 0.5.[30] In reports of 2-aza[3]ferrocenophane covalently attached to gold, similar asymmetry is seen when electrochemistry is performed in acidic media, which is attributed to an imbalance of mass transport in the anodic and cathodic processes.[35] Thus, there is likely a greater imbalance of mass transport in the anodic and cathodic processes for ITO|Vinylferrocene than ITO|Pyr|Pyrenylferrocene.

2.2.7 Electrochemical Impedance Spectroscopy

Electrochemical impedance spectroscopy (EIS) was used to further understand charge-transfer processes at the modified ITO interfaces. EIS was performed at both 0 and 0.4 V vs SCE to deconvolute impedance arising from non-faradaic (0 V vs SCE) and faradaic (0.4 V vs SCE) processes. The equivalent circuit used to fit data at 0 V vs SCE consists of R_s (solution resistance), $R_{CT,\,nf}$ (non-faradaic charge-transfer resistance), and a constant phase element, $CPE_{CT,\,nf}$ (non-faradaic charge-transfer capacitance). At 0.4 V vs SCE, an additional resistor and constant phase element, $R_{CT,\,f}$ (faradaic charge-transfer resistance) and $CPE_{CT,\,f}$ (faradaic charge-transfer capacitance) are introduced to the equivalent circuit used for fitting. Constant phase elements are used instead of pure capacitors to obtain better fits.

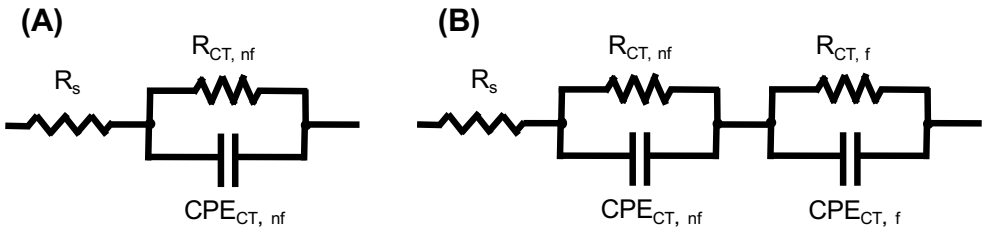

Figure 2.9. Equivalent circuits used to fit EIS data at (A) 0 V vs SCE and (B) 0.4 V vs SCE.

Nyquist plots for ITO|Pyr|Pyrenylferrocene and ITO|Vinylferrocene are displayed in Figure 2.10. When an electrode contains redox-active species adsorbed to their surface and redox pairs are not present in solution, the electrode behaves primarily as a capacitor due to the inability of the electrode to support steady-state current.[36-41] Consequently, the Nyquist plots for ITO|Pyr|Pyrenylferrocene and ITO|Vinylferrocene at both 0 and 0.4 V vs SCE display nearly vertical lines parallel to the y-axis. At 0.4 V vs SCE, the Nyquist plots for both ITO|Pyr|Pyrenylferrocene and ITO|Vinylferrocene shift closer toward linearity and are more parallel with the y-axis, indicating greater capacitor-like behavior relative to 0 V vs SCE.

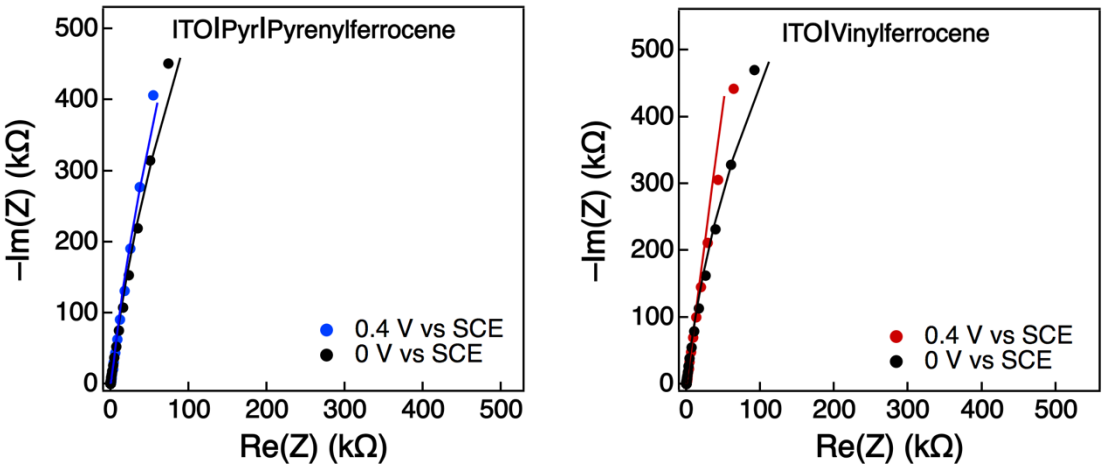

Figure 2.10. Nyquist plots for ITO|Pyr|Pyrenylferrocene (left) and ITO|Vinylferrocene (right). Raw EIS data are shown as solid circles and fits are represented as solid lines.

EIS data for surface-confined redox-active species are better represented in Cole-Cole plots where the imaginary complex capacitance (C") is plotted against the real complex capacitance (C'). C' and C" are obtained using the following equations:[36-41]

$$C' = \frac{Z_{Im}}{\omega(Z_{Re}^2+Z_{Im}^2)} \qquad (2.3)$$

$$C'' = \frac{Z_{Re}}{\omega(Z_{Re}^2+Z_{Im}^2)} \qquad (2.4)$$

where Z_{Re} and Z_{Im} are the real and imaginary components of impedance, respectively, and ω is the angular frequency. The Cole-Cole plots for ITO|Pyr|Pyrenylferrocene and ITO|Vinylferrocene are displayed in Figure 2.11. At both 0 and 0.4 V vs SCE, the Cole-Cole plots for ITO|Pyr|Pyrenylferrocene and ITO|Vinylferrocene exhibit large semicircles at high frequencies, attributed to the complex capacitance of non-faradaic electrochemical processes across the interface. A second semicircle at low frequencies is only present in the Cole-Cole plots for ITO|Pyr|Pyrenylferrocene and ITO|Vinylferrocene at 0.4 V vs SCE. The semicircle at low frequencies in the plots at 0.4 V vs SCE is due to complex capacitance arising from faradaic charge-transfer processes (oxidation of ferrocene on the surface). The frequency at the peak of the faradaic semicircle can be to calculate the rate constant for electron transfer using the following equation:[37, 39]

$$k_{ET} = \pi f_0 \qquad (2.5)$$

where k_{ET} is the rate constant for electron transfer and f_0 is the frequency at the peak of the faradaic semicircle. The rate constants for electron transfer through ITO|Pyr|Pyrenylferrocene and ITO|Vinylferrocene were calculated to be 117 and 35.8 s^{-1}, respectively. These rate constants are slightly higher than those obtained from the Laviron formalism (100 and 9 s^{-1}) but confirm the significant improvement in the rate of electron

transfer for the non-covalent attachment system relative to traditional covalent attachment approaches.

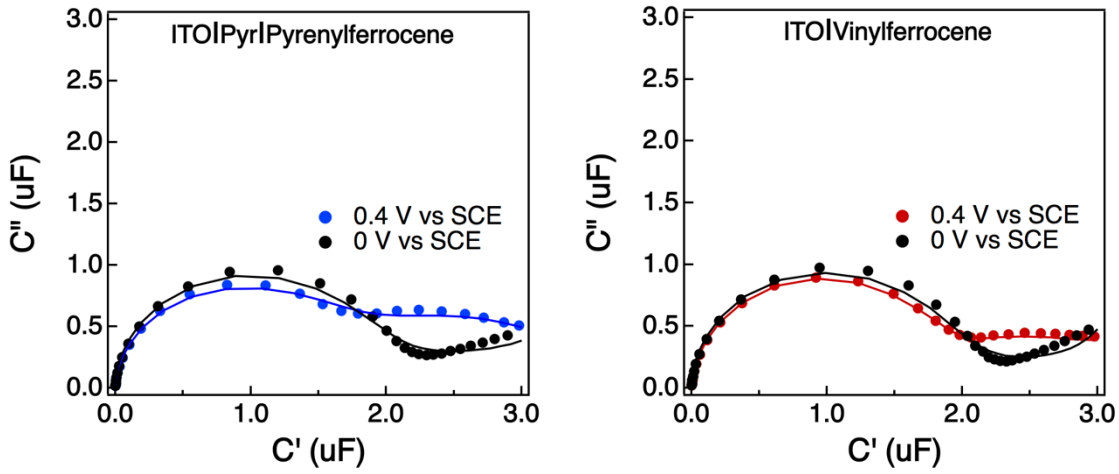

Figure 2.11. Cole-Cole plots for ITO|Pyr|Pyrenylferrocene (left) and ITO|Vinylferrocene (right). Raw EIS data are shown as solid circles and fits are represented as solid lines.

Finally, the resistance and constant phase element values obtained from fitting the EIS data for ITO|Pyr|Pyrenylferrocene and ITO|Vinylferrocene is displayed in Table 2.1. R_s, $CPE_{CT,\,nf}$, and $CPE_{CF,\,f}$ are consistent for both electrodes at 0 and 0.4 V vs SCE. $R_{CT,\,nf}$ is greater for ITO|Pyr|Pyrenylferrocene than ITO|Vinylferrocene and, for both electrodes, $R_{CT,\,nf}$ increases at 0.4 V vs SCE relative to 0 V vs SCE. Notably, $R_{CT,\,f}$ is approximately four times larger for ITO|Vinylferrocene than ITO|Pyr|Pyrenylferrocene. The significant increase in resistance of faradaic charge-transfer (ferrocene oxidation) for ITO|Vinylferrocene aligns with the slow electron-transfer across the ITO|Vinylferrocene relative to ITO|Pyr|Pyrenylferrocene.

Table 2.1. Resistance and constant phase element values extracted from fitting EIS data.

	V (vs SCE)	R_s (Ω cm^2)	$R_{CT,\,nf}$ (kΩ cm^2)	$CPE_{CT,\,nf}$ (μF cm^{-2})	$R_{CT,\,f}$ (Ω cm^2)	$CPE_{CT,\,f}$ (μF cm^{-2})
ITO|Pyr|Pyrenylferrocene	0	20.1	1210	12.8	-	-
	0.4	19.8	1620	14.4	174	146
ITO|Vinylferrocene	0	19.9	870	14.8	-	-
	0.4	19.6	1210	17.5	728	149

2.3 Conclusions

Indium tin oxide (ITO) was modified with ferrocene through both covalent (ITO|Vinylferrocene) and non-covalent interactions (ITO|Pyr|Pyrenylferrocene). In the presented non-covalent attachment approach, 1-pyrenylferrocene is physisorbed onto pyrene-appended ITO through π-π interactions; the covalently-bound pyrene layer is imperative for subsequent ferrocene immobilization. Modified electrodes were characterized using contact angle measurements and fluorescence and X-ray photoelectron spectroscopies, confirming the presence of pyrene, vinylferrocene, and 1-pyrenylferrocene on the surface.

Cyclic voltammetry of both ITO|Pyr|Pyrenylferrocene and ITO|Vinylferrocene exhibits a one-electron, reversible couple attributed to the $Cp_2Fe^{+/0}$ couple. Electron transfer rate constants for ITO|Pyr|Pyrenylferrocene and ITO|Vinylferrocene were calculated to be 100 and 9 s^{-1}, respectively, from the Laviron formalism and 117 and 35.8 s^{-1}, respectively, from EIS. The discrepancy in electron transfer rate constants between the two methods may be due to shortcomings associated with the Laviron formalism. The Laviron formalism assumes a potential-independent electron transfer coefficient;[30] theory and experiment have demonstrated potential-dependence of the electron transfer coefficient (α) which can result in error when calculating electron transfer rate constants using this method.[42-44] Despite this discrepancy between the two methods, electron transfer through the ITO|Pyr|Pyrenylferrocene interface is at least three times faster than electron transfer through the ITO|Vinylferrocene interface. Further EIS studies suggest that the fast electron transfer for ITO|Pyr|Pyrenylferrocene is due to a decrease in charge-transfer resistance for faradaic electrochemical processes at the electrode.

These results establish that the presented non-covalent attachment method not only provides a route for robust attachment to electrode surfaces, but also enhances the rate of electron transfer between the electrode and the immobilized species compared to conventional attachment methods. Notably, the rate of electron transfer through the ITO|Pyr|Pyrenylferrocene interface is fast enough to keep up with solar flux (minimum k_{app} for 10% catalyst coverage = 10 s^{-1}). [45] Thus, non-covalent attachment of molecular species to electrode surfaces using the presented technique is kinetically viable for solar driven photoelectrochemical applications.

2.4 Experimental Details

General Procedures

All reactions and manipulations were performed under an atmosphere of N_2 unless otherwise specified. Solvents were dried and degassed by sparging with argon and dried by passing through columns of neutral alumina or molecular sieves in an inert atmosphere. ITO on boro-aluminosilicate glass with a thickness of 0.5 mm and a sheet resistance of 5–15 Ω/sq was purchased from Delta Technologies. 1-Pyrenylferrocene[18] and 1-vinylpyrene[19] were prepared using previously published procedures. All other materials and reagents were purchased from commercial suppliers and used without purification (Aldrich and Fisher).

Physical Methods

X-ray photoelectron spectra were acquired with a Kratos Analytical AXIS Supra spectrometer utilizing monochromatic Al Kα radiation (1486.7 eV, 250 W) under ultra-high vacuum (UHV) conditions (~10−9 Torr). Survey spectra were collected with a pass energy of 160 eV and high-resolution scans were performed with a pass energy of 20 eV. The binding energies were referred to the C 1s signal at 285 eV. Spectral data was analyzed using

Computer Aided Surface Analysis for X-ray Photoelectron Spectroscopy (CasaXPS). Shirley or linear backgrounds and Gaussian-Lorentzian lineshapes were used to model peaks.

Two-photon fluorescence spectral images of the functionalized ITO surface were obtained using a modified Olympus FV1000 with an IX81 (Olympus Corporation) confocal laser scanning microscope and a water objective with a 1.2 numerical aperture. Samples were illuminated with a titanium:sapphire laser (Coherent Inc.) operating at a wavelength of 714 nm. For fluorescence spectral image acquisition, the emission signal was delivered to a Shamrock SR-303i spectrograph (Andor Technology) equipped with 512-channel ultrafast iXon Ultra EMCCD (Andor Technology). Spectra were acquired with an exposure time of 37 μs and corrected with a spectral response curve of the system calibrated using a tungsten lamp. For a detailed description of the setup and experimental conditions see ref. 46.[46]

Static contact angles were determined using the standard sessile drop technique. A 2.0 μL droplet of deionized water was carefully dropped onto the surface of the ITO electrodes and a Rame-Hart goniometer (Model 100) was used to measure contact angles.

Electrochemical Experiments

Cyclic voltammetry experiments were carried out in 100 mM aqueous KCl solutions. An SCE reference electrode and a glassy carbon rod auxiliary electrode were used in all electrochemical experiments. All voltammetric experiments were performed with a Pine Wavedriver 10 potentiostat and Aftermath software and reported peak current densities are corrected for capacitive currents using Aftermath software.

Electrochemical impedance spectroscopy was performed using a Biologic SP-300 potentiostat and EC-Lab software with AC amplitude of 10 mV and frequency scanning from 10^6 and 0.1 Hz. EIS experiments were carried out in 100 mM aqueous KCl using an SCE

reference electrode and a glassy carbon rod auxiliary electrode. The distance between electrodes was held constant throughout all measurements.

Substrate Modification

ITO electrodes were cleaned by immersing samples in a series of solvents at 50 °C for 10 minutes each. The order of solvents was as follows: trichloroethylene, acetone, and methanol. The electrodes were rinsed with H_2O and dried under a stream of N_2 after each solvent. Electrodes were functionalized immediately after cleaning. Clean ITO samples were placed in vial, ITO side facing up, and immersed in a 1 mM solution of 1-vinylpyrene in anhydrous toluene. The solution was heated to 80 °C for 24 hours. The samples were removed from the vial, rinsed with anhydrous toluene and CH_2Cl_2, and dried under a stream of N_2. ITO|Pyr samples were placed in a 1 mM solution of 1-pyrenylferrocene in anhydrous CH_2Cl_2 for 12 hours. The samples were removed from the solution, rinsed with anhydrous CH_3CN to remove loosely bound species, and dried to give ITO|Pyr|Pyrenylferrocene. ITO|Vinylferrocene samples were prepared by immersing a clean ITO sample in a 1 mM solution of vinylferrocene in $(nBu)_2O$ at 80 °C for 24 hours. The samples were then rinsed with $(nBu)_2O$ and dried under N_2.

2.5 References

1. Vericat, C.; Vela, M. E.; Corthey, G.; Pensa, E.; Cortes, E.; Fonticelli, M. H.; Ibanez, F.; Benitez, G. E.; Carro, P.; Salvarezza, R. C., Self-assembled monolayers of thiolates on metals: a review article on sulfur-metal chemistry and surface structures. *RSC Adv.* **2014,** *4*, 27730-27754.

2. Casalini, S.; Bortolotti, C. A.; Leonardi, F.; Biscarini, F., Self-assembled monolayers in organic electronics. *Chem. Soc. Rev.* **2017,** *46*, 40-71.

3. Brown, E. S.; Peczonczyk, S. L.; Wang, Z.; Maldonado, S., Photoelectrochemical Properties of CH3-Terminated p-Type GaP(111)A. *J. Phys. Chem. C* **2014,** *118*, 11593-11600.

4. Mukherjee, J.; Peczonczyk, S.; Maldonado, S., Wet Chemical Functionalization of III–V Semiconductor Surfaces: Alkylation of Gallium Phosphide Using a Grignard Reaction Sequence. *Langmuir* **2010,** *26*, 10890-10896.

5. Richards, D.; Zemlyanov, D.; Ivanisevic, A., Assessment of the Passivation Capabilities of Two Different Covalent Chemical Modifications on GaP(100). *Langmuir* **2010,** *26*, 8141-8146.

6. Cuypers, D.; Fleischmann, C.; van Dorp, D. H.; Brizzi, S.; Tallarida, M.; Müller, M.; Hönicke, P.; Billen, A.; Chintala, R.; Conard, T.; Schmeißer, D.; Vandervorst, W.; Van Elshocht, S.; Armini, S.; De Gendt, S.; Adelmann, C., Sacrificial Self-Assembled Monolayers for the Passivation of GaAs (100) Surfaces and Interfaces. *Chem. Mater.* **2016,** *28*, 5689-5701.

7. Oh, S.; Gallagher, J. R.; Miller, J. T.; Surendranath, Y., Graphite-Conjugated Rhenium Catalysts for Carbon Dioxide Reduction. *J. Am. Chem. Soc.* **2016,** *138*, 1820-1823.

8. Jackson, M. N.; Oh, S.; Kaminsky, C. J.; Chu, S. B.; Zhang, G.; Miller, J. T.; Surendranath, Y., Strong Electronic Coupling of Molecular Sites to Graphitic Electrodes via Pyrazine Conjugation. *J. Am. Chem. Soc.* **2018,** *140*, 1004-1010.

9. Fukushima, T.; Drisdell, W.; Yano, J.; Surendranath, Y., Graphite-Conjugated Pyrazines as Molecularly Tunable Heterogeneous Electrocatalysts. *J. Am. Chem. Soc.* **2015,** *137*, 10926-10929.

10. Beiler, A. M.; Khusnutdinova, D.; Jacob, S. I.; Moore, G. F., Solar Hydrogen Production Using Molecular Catalysts Immobilized on Gallium Phosphide (111)A and (111)B Polymer-Modified Photocathodes. *ACS Appl. Mater. Interfaces* **2016,** *8*, 10038-10047.

11. Wadsworth, B. L.; Beiler, A. M.; Khusnutdinova, D.; Jacob, S. I.; Moore, G. F., Electrocatalytic and Optical Properties of Cobaloxime Catalysts Immobilized at a Surface-Grafted Polymer Interface. *ACS Catal.* **2016,** *6*, 8048-8057.

12. Lei, H.; Liu, C.; Wang, Z.; Zhang, Z.; Zhang, M.; Chang, X.; Zhang, W.; Cao, R., Noncovalent Immobilization of a Pyrene-Modified Cobalt Corrole on Carbon Supports for Enhanced Electrocatalytic Oxygen Reduction and Oxygen Evolution in Aqueous Solutions. *ACS Catal.* **2016,** *6*, 6429-6437.

13. Creus, J.; Matheu, R.; Peñafiel, I.; Moonshiram, D.; Blondeau, P.; Benet-Buchholz, J.; García-Antón, J.; Sala, X.; Godard, C.; Llobet, A., A Million Turnover Molecular Anode for Catalytic Water Oxidation. *Angew. Chem. Int. Ed.* **2016,** *55*, 15382-15386.

14. Li, F.; Zhang, B.; Li, X.; Jiang, Y.; Chen, L.; Li, Y.; Sun, L., Highly Efficient Oxidation of Water by a Molecular Catalyst Immobilized on Carbon Nanotubes. *Angew. Chem. Int. Ed.* **2011,** *50*, 12276-12279.

15. Tran, P. D.; Le Goff, A.; Heidkamp, J.; Jousselme, B.; Guillet, N.; Palacin, S.; Dau, H.; Fontecave, M.; Artero, V., Noncovalent Modification of Carbon Nanotubes with Pyrene-Functionalized Nickel Complexes: Carbon Monoxide Tolerant Catalysts for Hydrogen Evolution and Uptake. *Angew. Chem. Int. Ed.* **2011,** *50*, 1371-1374.

16. Blakemore, J. D.; Gupta, A.; Warren, J. J.; Brunschwig, B. S.; Gray, H. B., Noncovalent Immobilization of Electrocatalysts on Carbon Electrodes for Fuel Production. *J. Am. Chem. Soc.* **2013,** *135*, 18288-18291.

17. Maurin, A.; Robert, M., Noncovalent Immobilization of a Molecular Iron-Based Electrocatalyst on Carbon Electrodes for Selective, Efficient CO2-to-CO Conversion in Water. *J. Am. Chem. Soc.* **2016,** *138*, 2492-2495.

18. Lydon, B. R.; Germann, A.; Yang, J. Y., Chemical modification of gold electrodes via non-covalent interactions. *Inorg. Chem. Front.* **2016,** *3*, 836-841.

19. Albagli, D.; Bazan, G. C.; Schrock, R. R.; Wrighton, M. S., New functional polymers prepared by ring-opening metathesis polymerization: study of the quenching of luminescence of pyrene end groups by ferrocene or phenothiazine centers in the polymers. *J. Phys. Chem.* **1993,** *97*, 10211-10216.

20. Pujari, S. P.; Scheres, L.; van Lagen, B.; Zuilhof, H., Organic Monolayers from 1-Alkynes Covalently Attached to Chromium Nitride: Alkyl and Fluoroalkyl Termination. *Langmuir* **2013,** *29*, 10393-10404.

21. Rosso, M.; Arafat, A.; Schroën, K.; Giesbers, M.; Roper, C. S.; Maboudian, R.; Zuilhof, H., Covalent Attachment of Organic Monolayers to Silicon Carbide Surfaces. *Langmuir* **2008,** *24*, 4007-4012.

22. Mischki, T. K.; Donkers, R. L.; Eves, B. J.; Lopinski, G. P.; Wayner, D. D. M., Reaction of Alkenes with Hydrogen-Terminated and Photooxidized Silicon Surfaces. A Comparison of Thermal and Photochemical Processes. *Langmuir* **2006,** *22*, 8359-8365.

23. Zachariasse, K. A.; Duveneck, G.; Busse, R., Intramolecular excimer formation with 1,3-di(1-pyrenyl)propane. Decay parameters and influence of viscosity. *J. Am. Chem. Soc.* **1984,** *106*, 1045-1051.

24. Nakagawa, K.; Numata, Y.; Ishino, H.; Tanaka, D.; Kobayashi, T.; Tokunaga, E., Excimer Luminescence From Nonresonantly Excited Pyrene and Perylene Molecules in Solution. *J. Phys. Chem. A* **2013,** *117*, 11449-11455.

25. Kamat, P. V.; Basheer, R.; Fox, M. A., Polymer-modified electrodes. Electrochemical and photoelectrochemical polymerization of 1-vinylpyrene. *Macromolecules* **1985,** *18*, 1366-1371.

26. Francis, C.; Lin, J.; Singer, L. A., Photophysical studies of pyrene on oxide supports. The effect of surface modification on probe dispersion and mobility. *Chem. Phys. Lett.* **1983,** *94*, 162-167.

27. Eckermann, A. L.; Feld, D. J.; Shaw, J. A.; Meade, T. J., Electrochemistry of redox-active self-assembled monolayers. *Coord. Chem. Rev.* **2010,** *254*, 1769-1802.

28. Faulkner, A. J. B. a. L. R., *Electrochemical Methods*. Second ed.; John Wiley & Sons, Inc.: 2001.

29. Chidsey, C. E. D.; Bertozzi, C. R.; Putvinski, T. M.; Mujsce, A. M., Coadsorption of ferrocene-terminated and unsubstituted alkanethiols on gold: electroactive self-assembled monolayers. *J. Am. Chem. Soc.* **1990,** *112*, 4301-4306.

30. Laviron, E., The use of linear potential sweep voltammetry and of a.c. voltammetry for the study of the surface electrochemical reaction of strongly adsorbed systems and of redox modified electrodes. *J. Electroanal. Chem. Interf. Electrochem.* **1979,** *100*, 263-270.

31. Hong, H. G.; Mallouk, T. E., Electrochemical measurements of electron transfer rates through zirconium 1,2-ethanediylbis(phosphonate) multilayer films on gold electrodes. *Langmuir* **1991,** *7*, 2362-2369.

32. Finklea, H. O.; Avery, S.; Lynch, M.; Furtsch, T., Blocking oriented monolayers of alkyl mercaptans on gold electrodes. *Langmuir* **1987,** *3*, 409-413.

33. Donley, C.; Dunphy, D.; Paine, D.; Carter, C.; Nebesny, K.; Lee, P.; Alloway, D.; Armstrong, N. R., Characterization of Indium−Tin Oxide Interfaces Using X-ray Photoelectron

Spectroscopy and Redox Processes of a Chemisorbed Probe Molecule: Effect of Surface Pretreatment Conditions. *Langmuir* **2002,** *18*, 450-457.

34. Kohmoto, M.; Ozawa, H.; Yang, L.; Hagio, T.; Matsunaga, M.; Haga, M.-a., Controlling the Adsorption of Ruthenium Complexes on Carbon Surfaces through Noncovalent Bonding with Pyrene Anchors: An Electrochemical Study. *Langmuir* **2016,** *32*, 4141-4152.

35. Horie, M.; Sakano, T.; Osakada, K., Preparation and electrochemical properties of SAM of alkanethiols functionalized with 2-aza[3]ferrocenophane on gold electrode. *J. Organomet. Chem.* **2006,** *691*, 5935-5945.

36. Nahir, T. M.; Bowden, E. F., Measurement of the Rate of Adsorption of Electroactive Cytochrome c to Modified Gold Electrodes by Electrochemical Impedance Spectroscopy. *Langmuir* **2002,** *18*, 5283-5286.

37. Silva, B. P. G.; de Florio, D. Z.; Brochsztain, S., Characterization of a Perylenediimide Self-Assembled Monolayer on Indium Tin Oxide Electrodes Using Electrochemical Impedance Spectroscopy. *J. Phys. Chem. C* **2014,** *118*, 4103-4112.

38. Bueno, P. R.; Fabregat-Santiago, F.; Davis, J. J., Elucidating Capacitance and Resistance Terms in Confined Electroactive Molecular Layers. *Anal. Chem.* **2013,** *85*, 411-417.

39. Katz, E.; Lioubashevsky, O.; Willner, I., Electromechanics of a Redox-Active Rotaxane in a Monolayer Assembly on an Electrode. *J. Am. Chem. Soc.* **2004,** *126*, 15520-15532.

40. Ruther, R. E.; Cui, Q.; Hamers, R. J., Conformational Disorder Enhances Electron Transfer Through Alkyl Monolayers: Ferrocene on Conductive Diamond. *J. Am. Chem. Soc.* **2013,** *135*, 5751-5761.

41. Wang, Q.; Zhi, F.; Wang, W.; Xia, X.; Liu, X.; Meng, F.; Song, Y.; Yang, C.; Lu, X., Direct Electron Transfer of Thiol-Derivatized Tetraphenylporphyrin Assembled on Gold Electrodes in an Aqueous Solution. *J. Phys. Chem. C* **2009,** *113*, 9359-9367.

42. Weaver, M. J.; Anson, F. C., Potential dependence of the electrochemical transfer coefficient. Further studies of the reduction of chromium(III) at mercury electrodes. *J. Phys. Chem.* **1976,** *80*, 1861-1866.

43. Corrigan, D. A.; Evans, D. H., Cyclic voltammetric study of tert-nitrobutane reduction in acetonitrile at mercury and platinum electrodes: Observation of a potential dependent electrochemical transfer coefficient and the influence of the electrolyte cation on the rate constant. *J. Electroanal. Chem. Interf. Electrochem.* **1980,** *106*, 287-304.

44. Finklea, H. O.; Ravenscroft, M. S.; Snider, D. A., Electrolyte and temperature effects on long range electron transfer across self-assembled monolayers. *Langmuir* **1993,** *9*, 223-227.

45. Li, F.; Basile, V. M.; Rose, M. J., Electron Transfer through Surface-Grown, Ferrocene-Capped Oligophenylene Molecular Wires (5–50 Å) on n-Si(111) Photoelectrodes. *Langmuir* **2015,** *31*, 7712-7716.

46. Chen, H.; Gratton, E.; Digman, M. A., Spectral properties and dynamics of gold nanorods revealed by EMCCD-based spectral phasor method. *Microsc. Res. Tech.* **2015,** *78*, 283-293.

CHAPTER 3

Proton-Coupled Electron Transfer at Anthraquinone Modified Indium Tin Oxide Electrodes

Portions of this chapter have been published:

Hanna. C. M.; Luu, A.; Yang, J. Y. *ACS Appl. Energy Mat.* **2019**, *2*, 59.

3.1 Introduction

Molecular modification of conducting and semiconducting electrodes has been utilized to produce functional materials for a wide variety of applications such as catalysis, sensing, electronics, and optics.[1-4] Tailoring electrode surfaces with molecular species enables atomic-level control of surface properties, including selective reactivity with incoming substrates.[5-9] The attachment of molecular electrocatalysts onto electrode surfaces is also of significant interest for the enhancement of heterogeneous redox catalysis.[5-7, 10-30] Integrating molecular electrocatalysts with electrodes can exploit the high selectivity of the former to fabricate heterogeneous catalysts more suitable for use in conventional electrolytic or fuel cells. Additionally, immobilization of catalysts for electrolytic fuel forming reactions onto light absorbing materials can be used directly in monolithic photoelectrochemical cells, enabling direct sunlight driven electrolysis.[31-38]

Catalytic reactions of interest include the production and utilization of chemical fuels[5-7, 10-26, 28-29, 31-38] and atom-efficient organic synthesis.[27, 30] Nearly all of these targeted redox reactions require both proton and electron transfer. In order to achieve optimal efficiency, electrocatalysts often utilize proton-coupled electron transfer (PCET) steps to avoid high energy catalytic pathways. Traditional methods of immobilizing molecular species onto electrode surfaces can significantly affect the molecules' reactivity due to changes in solvation and electron density after adsorption and lateral interactions between attached molecules.[16-18, 39-40]

The Yang lab's approach for attaching molecular species to electrode surfaces involves appending both the molecule and the electrode with pyrene molecules which enables immobilization through π-π interactions between the two pyrene moieties.

Extension of this attachment system to redox catalysts that utilize PCET requires the retention of solution-phase behavior upon immobilization onto the surface. Anthraquinones are an ideal molecular species to compare proton-coupled electron transfer properties before and after immobilization. Quinones and their derivatives are biologically prevalent organic compounds with redox chemistry that plays a vital role in energy storage and transduction.[41] The biological importance of quinones has prompted numerous studies analyzing their electrochemical properties both in solution and immobilized onto surfaces.[42-49] Quinones undergo a two-electron reduction to give the quinone dianion, the dihydroquinone, or the hydrogen-bonded quinone dianion depending on the nature of the solvent.[42] In buffered solution with a pH lower than the pK_a of the phenolic protons, the two-electron reduction is coupled with two protonation steps to form the dihydroquinone.[42, 45]

To analyze the PCET behavior of molecular species immobilized using the Yang lab's hybrid attachment method, a pyrene-appended anthraquinone ($Pyr(AQ)_2$) is attached to pyrene-bound indium tin oxide (ITO) electrodes as depicted in Scheme 3.1. The pH-dependent electrochemistry of $Pyr(AQ)_2$ immobilized on pyrene-bound ITO and comparison to that of a water-soluble anthraquinone derivative, sodium anthraquinone-2-sulfonate (AQS), is described.

Scheme 3.1. Pictorial representation of the attachment of anthraquinone to indium tin oxide (ITO) electrodes through non-covalent interactions.

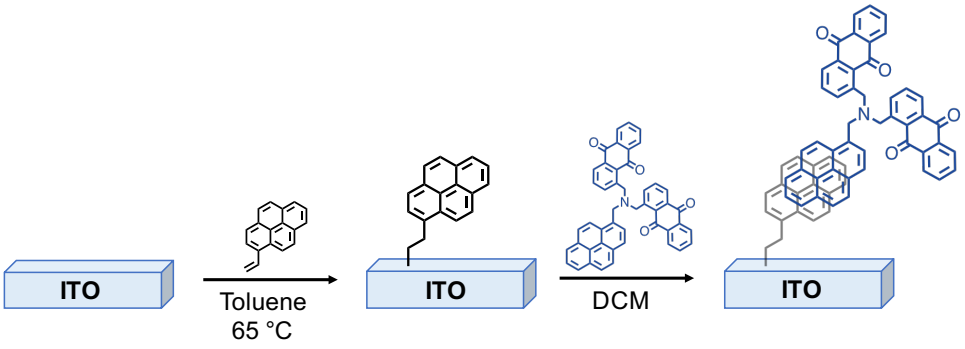

3.2 Results and Discussion

3.2.1 Modification of ITO and Spectroscopic Characterization

1-Vinylpyrene[50] and 1-[bis(2-anthraquinonyl)aminomethyl]pyrene ($Pyr(AQ)_2$)[51] were prepared using reported procedures. Indium tin oxide (ITO) was covalently modified with 1-vinylpyrene by immersing clean ITO samples in toluene solutions of 1-vinylpyrene at 65 °C for 24 h to yield pyrene-modified ITO (ITO|Pyr). Subsequent attachment of $Pyr(AQ)_2$ was achieved by immersing ITO|Pyr in CH_2Cl_2 solutions of $Pyr(AQ)_2$ for 12 h, yielding non-covalently modified ITO|Pyr|$Pyr(AQ)_2$. $Pyr(AQ)_2$ coverage, calculated by integrating the cathodic peak of the cyclic voltammograms (CVs) of ITO|Pyr|$Pyr(AQ)_2$, ranged from 40 pmol/cm^2 to 80 pmol/cm^2. These coverage values are an order of magnitude greater than those of 1-pyrenylferrocene immobilized onto ITO|Pyr. The increase in coverage is attributed to the ability of $Pyr(AQ)_2$ to hydrogen bond to the terminal hydroxyl groups on the ITO surface[52] and the possibility of π-π interactions between anthraquinone and the surface-bound pyrene.

X-ray photoelectron spectroscopy (XPS) was used to characterize the anthraquinone-modified ITO electrodes. Non-covalent attachment of $Pyr(AQ)_2$ onto ITO|Pyr results in the appearance of a N 1s peak in the XPS spectrum. The high-resolution XPS spectra of the N 1s region of ITO|Pyr|$Pyr(AQ)_2$ and ITO|Pyr are displayed in Figure 3.1. The peak at 400 eV, attributed to the tertiary amine of $Pyr(AQ)_2$, is consistent with literature reports of alkyl amines deposited on carbon electrodes.[53] The high-resolution XPS spectrum of the N 1s region of ITO|Pyr does not exhibit any peaks. These results confirm the presence of $Pyr(AQ)_2$ on the modified electrode surface.

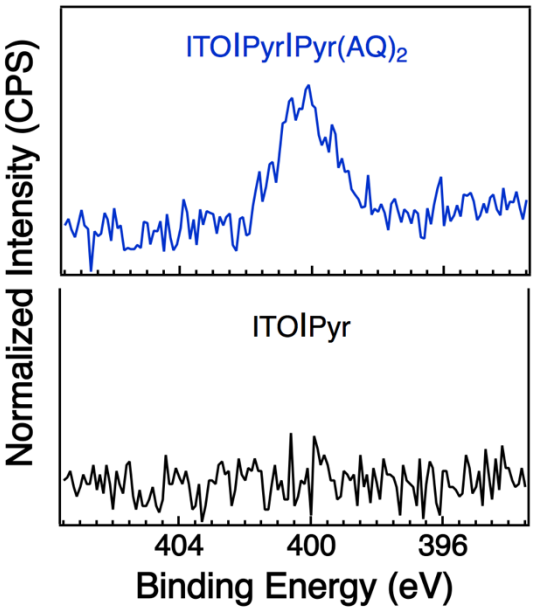

Figure 3.1. High-resolution XPS spectra of the N 1s region of ITO|Pyr|Pyr(AQ)$_2$ and ITO|Pyr.

3.2.2 Electrochemical Analysis of Modified ITO

The cyclic voltammogram (CV) of ITO|Pyr|Pyr(AQ)$_2$ in pH 7 HEPES buffer is displayed in Figure 3.2 (green trace). The CV exhibits a redox couple with an $E_{1/2}$ of –0.52 V vs SCE attributed to the two-electron reduction of anthraquinone to dihydroanthraquinone. The $E_{1/2}$ of the two-electron reduction agrees well with reported literature values of the reduction of immobilized anthraquinone on gold and carbon nanotubes at pH 7.[44, 46]

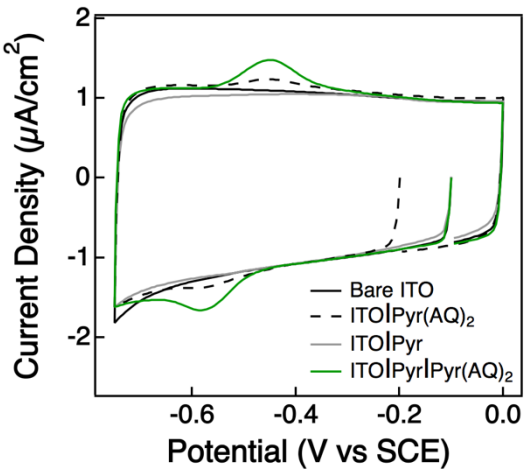

Figure 3.2. Cyclic voltammetry of ITO|Pyr|Pyr(AQ)$_2$, ITO|Pyr, ITO, and ITO treated with Pyr(AQ)$_2$ performed at 50 mV/s in 100 mM pH 7 HEPES buffer with 100 mM KCl as a supporting electrolyte.

In addition to the CV of ITO|Pyr|Pyr(AQ)$_2$, Figure 2 displays the CVs of bare ITO, ITO|Pyr, and a bare ITO electrode soaked in a solution of Pyr(AQ)$_2$ (denoted as ITO|Pyr(AQ)$_2$) in pH 7 HEPES buffer. The CVs of bare ITO (black trace) and ITO|Pyr (gray trace) do not display notable features, ensuring the couple exhibited in the CV of ITO|Pyr|Pyr(AQ)$_2$ is attributed to Pyr(AQ)$_2$. The CV of ITO|Pyr(AQ)$_2$ (black dashed trace), which has no pyrene monolayer, also exhibits a redox couple at the same potential observed for ITO|Pyr|Pyr(AQ)$_2$ (green trace). Pyr(AQ)$_2$ likely hydrogen bonds to the terminal hydroxyl groups on the ITO surface, enabling adsorption without the presence of the pyrene monolayer.[52] Integration of the cathodic peak of the CV of ITO|Pyr(AQ)$_2$ yields an electrochemically active coverage of 20 pmol/cm^2. Thus, the pyrene monolayer allows for two to four times the Pyr(AQ)$_2$ coverage compared to physisorption without a pyrene monolayer. Finally, the variable scan rate cyclic voltammetry of ITO|Pyr|Pyr(AQ)$_2$ at pH 7 and the corresponding peak current density vs scan rate plot is shown in Figure 3.3. Peak currents vary linearly with scan rate, confirming that Pyr(AQ)$_2$ is bound to the surface.

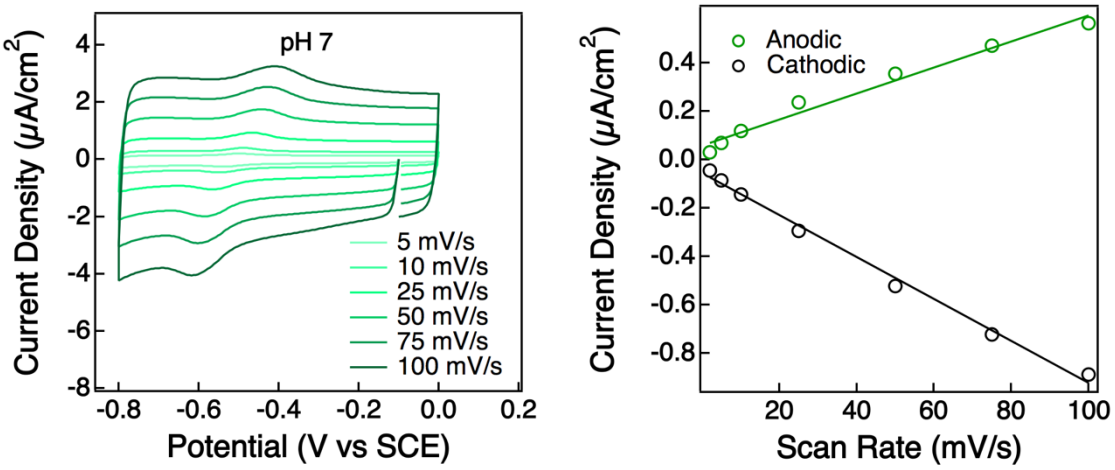

Figure 3.3. Variable scan rate cyclic voltammetry of ITO|Pyr|Pyr(AQ)$_2$ performed in 100 mM pH 7 HEPES buffer with 100 mM KCl as a supporting electrolyte (left) and the corresponding peak current density vs scan rate plot (right).

Due to the insolubility of Pyr(AQ)$_2$ in water, the variable scan rate CVs and the corresponding peak current vs square root of scan rate plot of Pyr(AQ)$_2$ was measured in dimethylformamide (DMF) (Figure 3.4). In DMF solution, the anthraquinone moieties of Pyr(AQ)$_2$ undergo two quasi-reversible one-electron reductions at –1.33 and –2.00 V vs Fe(C$_5$H$_5$)$_2^{+/0}$ and a third irreversible reduction at –2.56 V vs Fe(C$_5$H$_5$)$_2^{+/0}$. The two one-electron events align with previous reports wherein quinones and their derivatives undergo two one-electron reductions in aprotic solvents and a single two-electron reduction in protic solvents.[42] Peak currents of the reductions at –1.33 and –2.00 V vs Fe(C$_5$H$_5$)$_2^{+/0}$ vary linearly with the square root of scan rate, indicating a diffusion-limited electrochemical process.

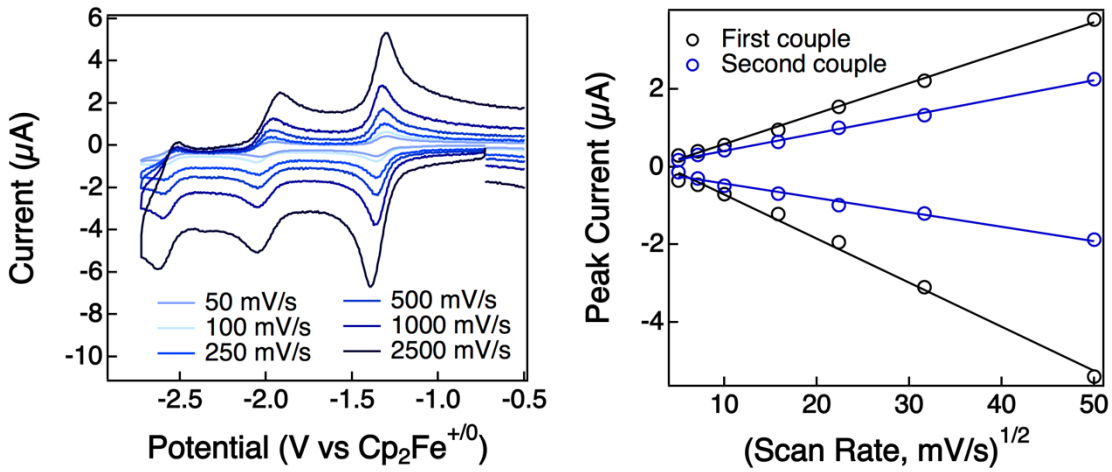

Figure 3.4. Variable scan rate cyclic voltammetry of $Pyr(AQ)_2$ performed in dimethylformamide (left) and the corresponding peak current density vs square root of scan rate plot (right).

In order to probe the dependence of ITO|Pyr|$Pyr(AQ)_2$ reduction on pH, CVs were recorded in buffered solutions between pH 5 and 9. The variable scan rate CVs and corresponding peak current density vs scan rate plots of ITO|Pyr|$Pyr(AQ)_2$ at pH 5, 6, 8, and 9 are displayed in Figures 3.5–3.8. The CVs at each pH display the two-electron redox couple corresponding to the reduction of anthraquinone to dihydroquinone. At all pH values, peak current varies linearly with scan rate, ensuring the attachment of $Pyr(AQ)_2$ on the ITO|Pyr surface across all pH conditions. The $E_{1/2}$ at each pH is listed in Table 3.1. As the pH increases, the $E_{1/2}$ decreases linearly by 60 mV per pH unit. This linear dependence is consistent with a two-electron/two-proton process, confirming the formation of the dihydroanthraquinone upon reduction within the tested pH range.[43, 54] Above pH 9, a more shallow slope is expected due to deprotonation of the phenolic protons. However, the instability of ITO above pH 9 prevents electrochemical analysis of ITO|Pyr|$Pyr(AQ)_2$ under these conditions.[55]

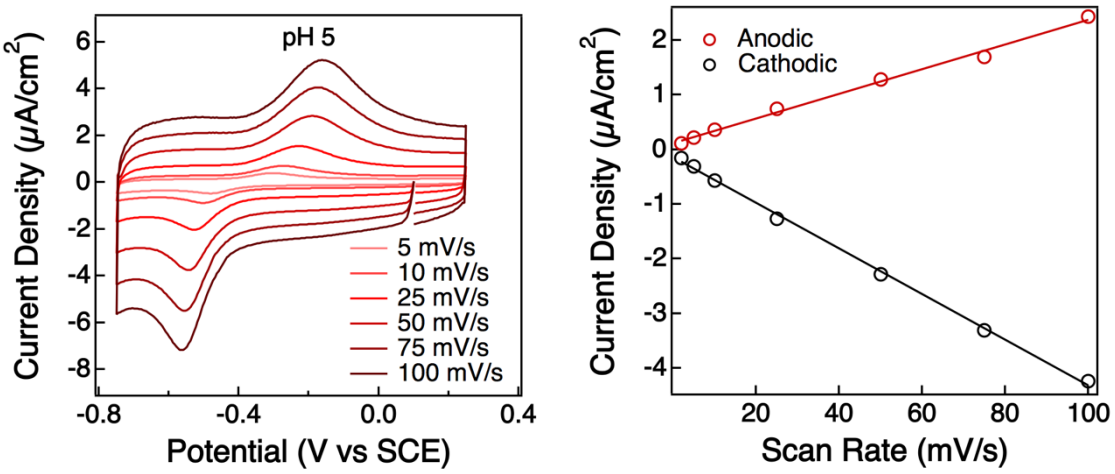

Figure 3.5. Variable scan rate cyclic voltammetry of ITO|Pyr|Pyr(AQ)$_2$ performed in 100 mM pH 5 citrate buffer with 100 mM KCl as a supporting electrolyte (left) and the corresponding peak current density vs scan rate plot (right).

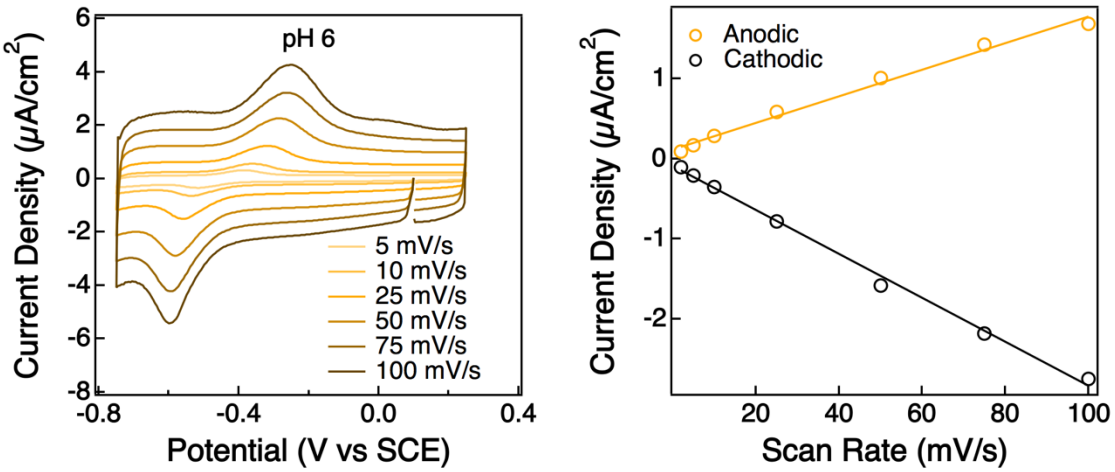

Figure 3.6. Variable scan rate cyclic voltammetry of ITO|Pyr|Pyr(AQ)$_2$ performed in 100 mM pH 6 citrate buffer with 100 mM KCl as a supporting electrolyte (left) and the corresponding peak current density vs scan rate plot (right).

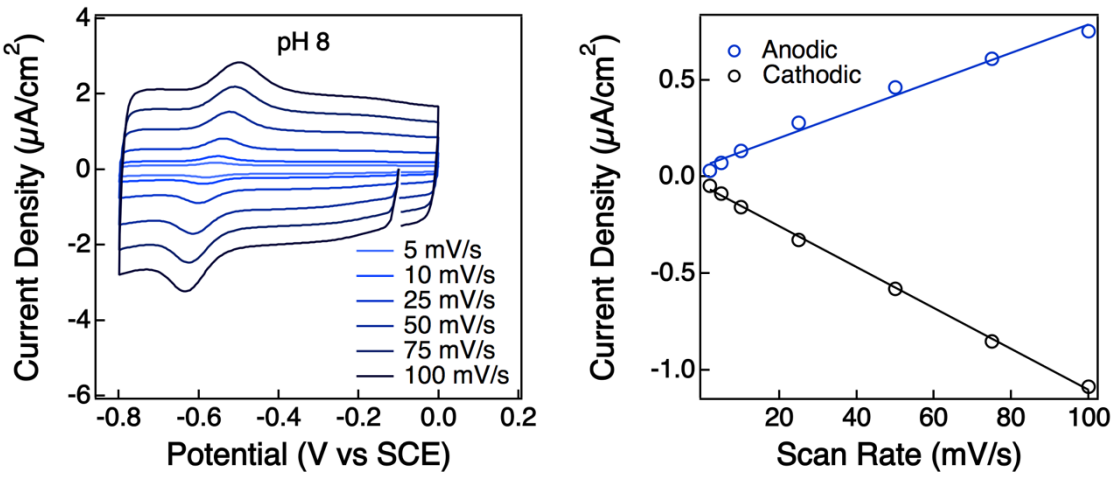

Figure 3.7. Variable scan rate cyclic voltammetry of ITO|Pyr|Pyr(AQ)$_2$ performed in 100 mM pH 8 HEPES buffer with 100 mM KCl as a supporting electrolyte (left) and the corresponding peak current density vs scan rate plot (right).

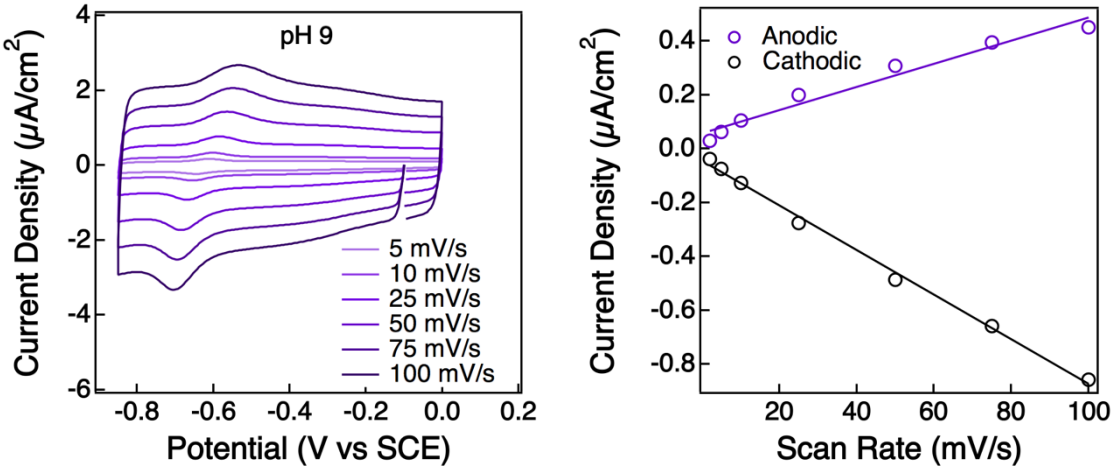

Figure 3.8. Variable scan rate cyclic voltammetry of ITO|Pyr|Pyr(AQ)$_2$ performed in 100 mM pH 9 borate buffer with 100 mM KCl as a supporting electrolyte (left) and the corresponding peak current density vs scan rate plot (right).

Table 3.1. Redox potentials and rates of electron transfer of ITO|Pyr|Pyr(AQ)$_2$ and AQS under varying pH conditions.

	ITO|Pyr|Pyr(AQ)$_2$		Anthraquinone Sulfonate (AQS)	
pH (Buffer)	**$E_{1/2}$ (V vs SCE)**	**k_{app} (s^{-1})**	**$E_{1/2}$ (V vs SCE)**	**k_{app} (cm/s)**
5 (Citrate)	−0.39	0.01 ± 0.01	−0.34	0.003 ± 0.001
6 (Citrate)	−0.45	0.02 ± 0.01	−0.40	0.01 ± 0.01
7 (HEPES)	−0.52	0.2 ± 0.1	−0.46	0.03 ± 0.01
8 (HEPES)	−0.57	0.4 ± 0.1	−0.51	0.04 ± 0.01
9 (Borate)	−0.63	0.4 ± 0.1	−0.55	0.8 ± 0.3

3.2.3 Electron Transfer Kinetics of Modified ITO

In the variable scan rate cyclic voltammograms (CVs) of ITO|Pyr|Pyr(AQ)$_2$ in Figures 3.3 and 3.5–3.8, the difference between the cathodic and anodic peak potentials increases with increasing scan rate. Under ideal reversible conditions, the peak-to-peak separation of immobilized redox-active species is expected to be 0 mV.[54] The increase in peak-to-peak separation with faster scan rate suggests slow electron transfer between ITO and Pyr(AQ)$_2$. Electron transfer kinetics can be analyzed using the following Laviron equations:[56]

$$E_{p,c} = E^{\circ\prime} - \frac{2.3\mathrm{RT}}{\alpha nF}\log\left[\frac{\alpha nFv_c}{RTk_{app}}\right] \qquad (3.1)$$

$$E_{p,a} = E^{\circ\prime} - \frac{2.3\mathrm{RT}}{(1-\alpha)nF}\log\left[\frac{(1-\alpha)nFv_a}{RTk_{app}}\right] \qquad (3.2)$$

where $E_{p,a}$ is the potential of the anodic peak, $E_{p,c}$ is the potential of the cathodic peak, E°' is the formal potential calculated by averaging the anodic and cathodic potentials at slow scan rates, v_a and v_c are the critical scan rates, α is the electron transfer coefficient, k_{app} is the apparent rate constant, R is the ideal gas constant, T is the absolute temperature, F is the Faraday constant, and n is the number of electrons transferred. Electron transfer parameters (v_a, v_c, α, and k_{app}) are determined by plotting E_p – E°' against the log of the scan rate (trumpet plot). v_a and v_c are determined by extrapolating the linear portions of the plot where (E_p – E°') > 100 mV/n to 0 and α is obtained from the slopes of the linear fits. k_{app} is calculated using v_a, v_c, and α and is reported as the average of $k_{app,c}$ and $k_{app,a}$ across three individually prepared samples.

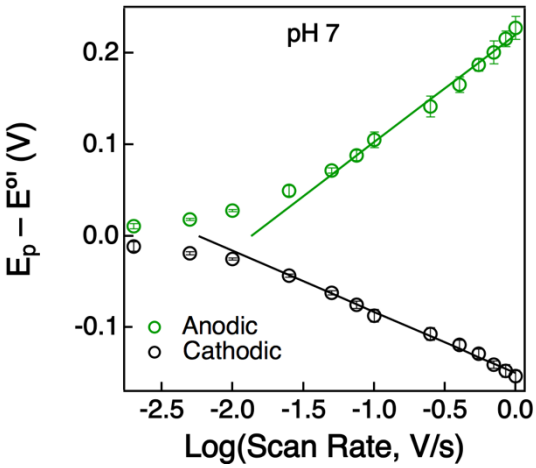

Figure 3.9. Trumpet plots of of ITO|Pyr|Pyr(AQ)$_2$ at pH 7.

The trumpet plot for ITO|Pyr|Pyr(AQ)$_2$ at pH 7 is shown in Figure 3.9. Using Equations 3.1 and 3.2, k_{app} for ITO|Pyr|Pyr(AQ)$_2$ at pH 7 was calculated to be 0.2 ± 0.1 s^{-1}. This rate is significantly slower than the electron transfer rate constant for 1-pyrenylferrocene immobilized on ITO|Pyr (100 s^{-1}). It is possible that the distance between the redox active anthraquinone moieties of Pyr(AQ)$_2$ and ITO is greater than the distance between ferrocene and ITO, which would result in slower electron transfer.[57] However, k_{app} for ITO|Pyr|Pyr(AQ)$_2$ is consistent with literature reports of anthraquinone attached to gold electrodes at pH 7.[43, 46] The slow electron transfer relative to 1-pyrenylferrocene on ITO|Pyr may therefore be due to intrinsically slow electron transfer between an electrode and anthraquinone derivatives. The trumpet plots for ITO|Pyr|Pyr(AQ)$_2$ at pH 5, 6, 8, and 9 are displayed in Figure 3.10 and k_{app} at each pH is listed in Table 3.1. It should be noted that while the Pyr(AQ)$_2$ coverage varies between 40 and 80 pmol/cm^2, there is no coverage dependence on k_{app}. Within the pH range explored in this study, electron transfer between ITO and immobilized Pyr(AQ)$_2$ increases in rate as pH increases. Similar increases were observed in monolayers of 1,4-hydroxynapthaquinone and galvinol on gold.[49, 58] However, it

is difficult to draw firm conclusions from the k_{app} dependence on pH because the buffer composition changes across the studied pH range. The identity of the buffer can impact proton transfer processes, leading to changes in mechanism or variable proton transfer rates.[58-59] These variations may contribute to the inconsistent k_{app} vs pH relationships for immobilized quinone species in literature.[43, 48] The limited pH range of citrate, HEPES, and borate buffers prevents exploration of the kinetics of electron transfer using a single buffer across the entire pH range studied.

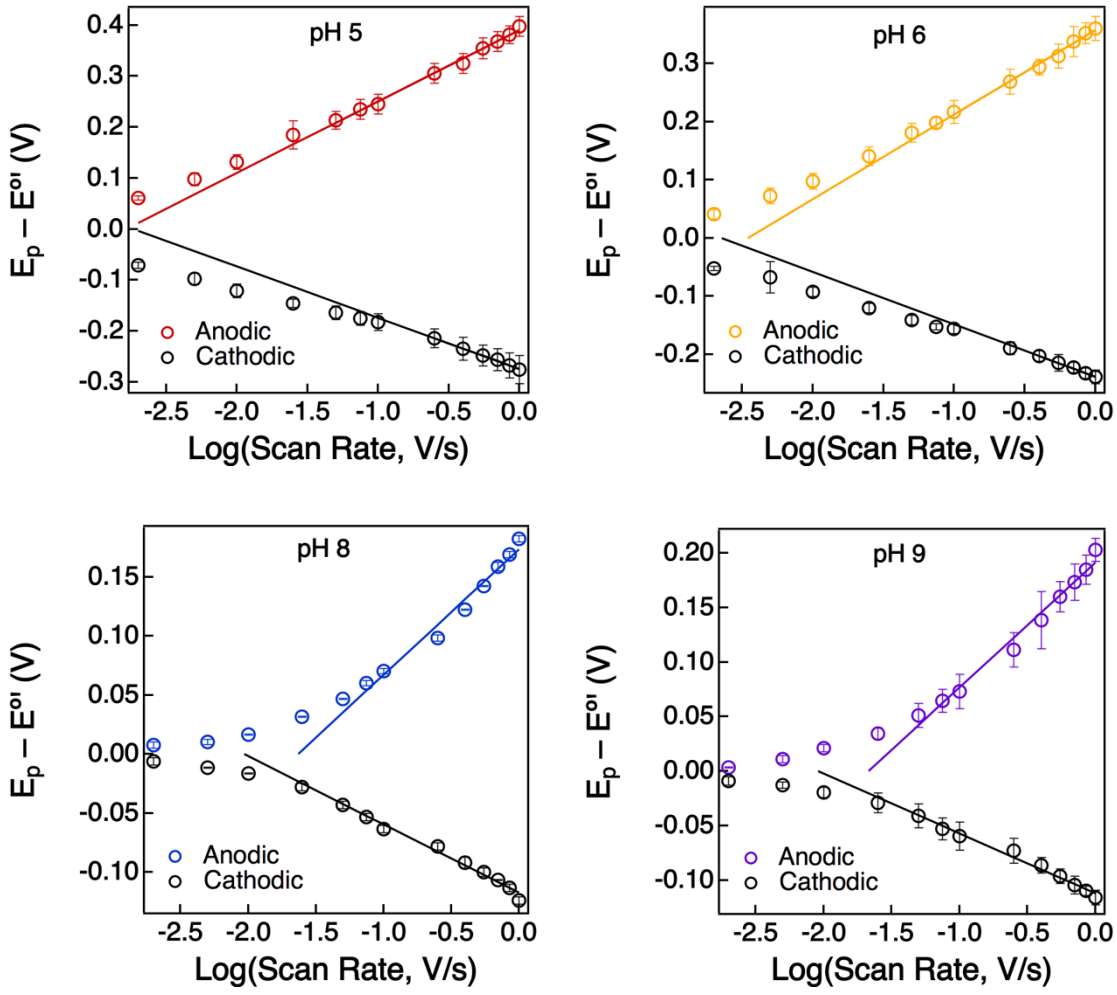

Figure 3.10. Trumpet plots of of ITO|Pyr|Pyr(AQ)$_2$ at pH 5, 6, 8, and 9.

3.2.4 Comparison to a Water Soluble Anthraquinone Derivative

Cyclic voltammetry of sodium 2-anthraquinonesulfonate (AQS), a water-soluble anthraquinone derivative, was performed to compare the electrochemical behavior of anthraquinone on the ITO surface and diffusing in solution. The variable scan rate cyclic voltammetry of AQS at pH 5–9 is displayed in Figures 3.11–3.15. As seen in the CVs of ITO|Pyr|Pyr(AQ)$_2$, AQS exhibits a two-electron reduction in all pH conditions studied, corresponding to reduction to the dihydroanthraquinone species. The peak currents of AQS vary linearly with the square root of scan rate, indicative of a diffusion-limited electrochemical process. The $E_{1/2}$ value for the reduction of AQS at each pH is listed in Table 3.1. The reduction potential of AQS in solution is about 50 mV more positive than that of ITO|Pyr|Pyr(AQ)$_2$. This shift in reduction potential is expected based on the strong electron-withdrawing character of the sulfonate group on AQS, enabling reduction at milder potentials. As seen in the reduction of ITO|Pyr|Pyr(AQ)$_2$, the $E_{1/2}$ of AQS decreases linearly with pH by 50 mV/pH unit (Figure 3.16), indicating a coupled two-electron/two-proton process. These results highlight the retention of proton-coupled electron transfer in anthraquinone upon non-covalent attachment to ITO surfaces.

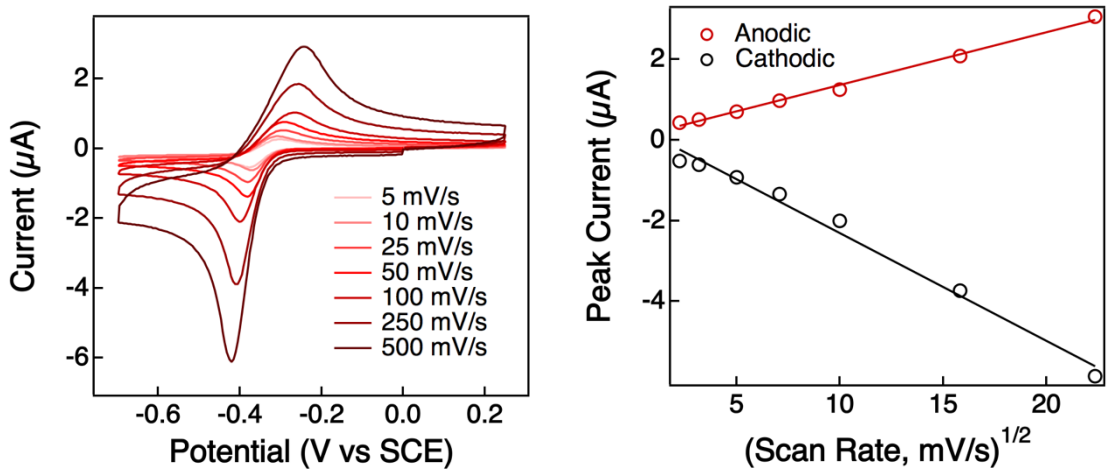

Figure 3.11. Variable scan rate cyclic voltammetry of AQS performed in 100 mM pH 5 citrate buffer with 100 mM KCl as a supporting electrolyte (left) and the corresponding peak current density vs square root of scan rate plot (right).

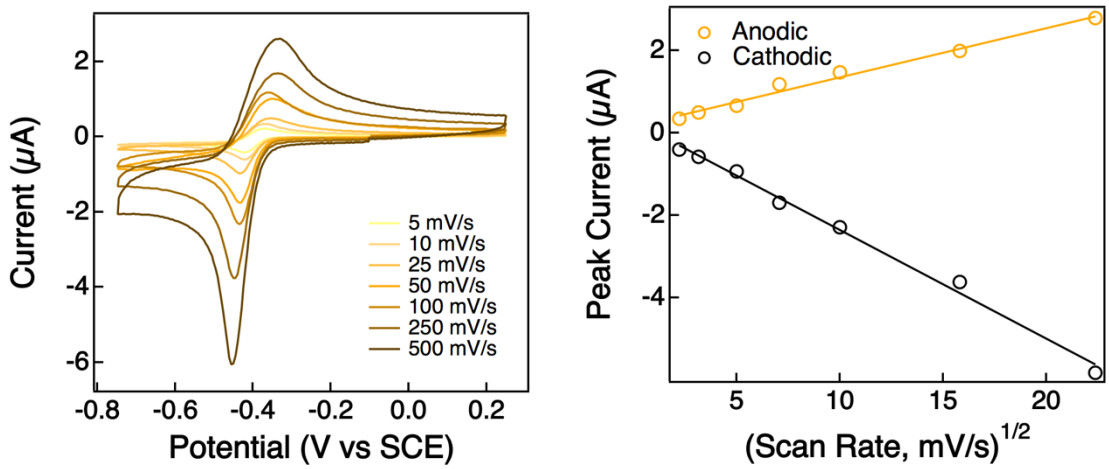

Figure 3.12. Variable scan rate cyclic voltammetry of AQS performed in 100 mM pH 6 citrate buffer with 100 mM KCl as a supporting electrolyte (left) and the corresponding peak current density vs square root of scan rate plot (right).

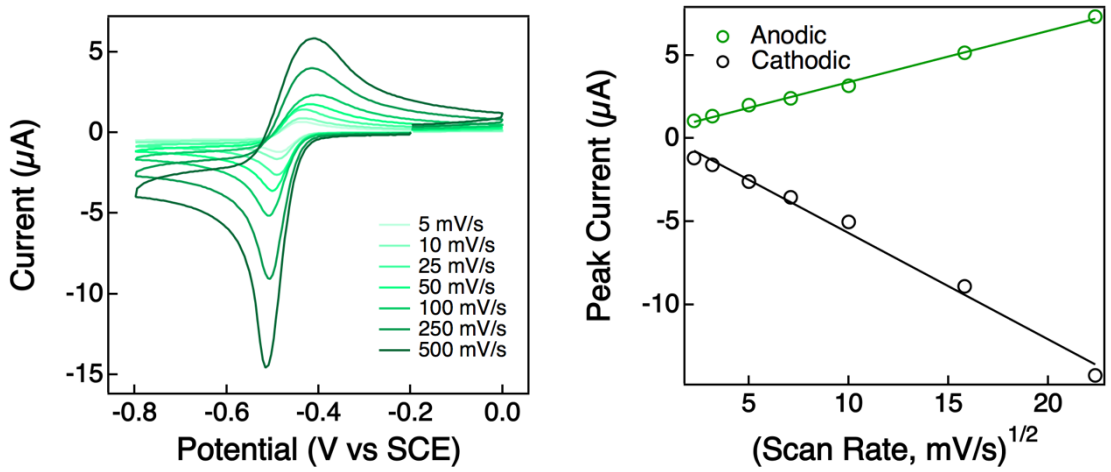

Figure 3.13. Variable scan rate cyclic voltammetry of AQS performed in 100 mM pH 7 HEPES buffer with 100 mM KCl as a supporting electrolyte (left) and the corresponding peak current density vs square root of scan rate plot (right).

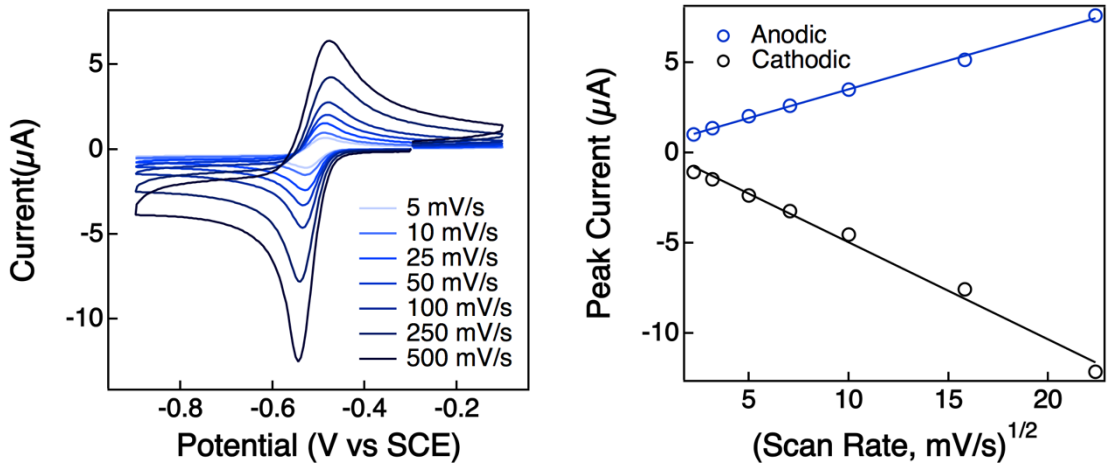

Figure 3.14. Variable scan rate cyclic voltammetry of AQS performed in 100 mM pH 8 HEPES buffer with 100 mM KCl as a supporting electrolyte (left) and the corresponding peak current density vs square root of scan rate plot (right).

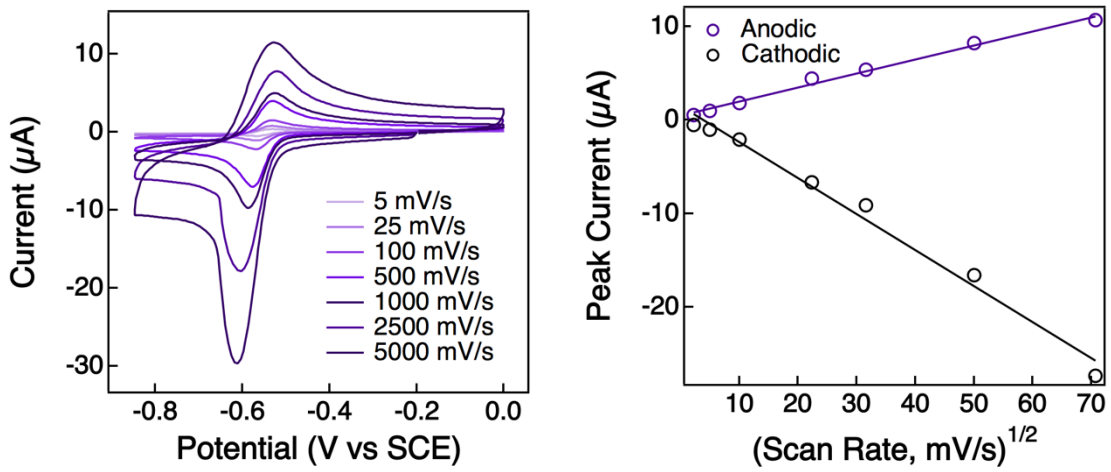

Figure 3.15. Variable scan rate cyclic voltammetry of AQS performed in 100 mM pH 9 Borate buffer with 100 mM KCl as a supporting electrolyte (left) and the corresponding peak current density vs square root of scan rate plot (right).

Similar to the CVs of ITO|Pyr|Pyr(AQ)$_2$, the CVs of AQS exhibit greater peak separation with increasing scan rate. Electron transfer rate constants for AQS were determined by applying the Kochi method to the experimentally determined peak separation.[60] Briefly, the potential of the cathodic peak ($E_{p,c}$) is plotted against the log of the scan rate (Figure 3.17) and the slope of the linear portion (irreversible region) of the plot is used to determine the electron transfer coefficient, α, using the following equation:

$$\alpha = \left[\frac{1}{slope}\right]\left[\frac{2.3RT}{2nF}\right] \qquad (3.3)$$

k_{app} is then calculated at multiple scan rates in the irreversible region and reported as an average across all scan rates using Equation 3.4:

$$k_{app} = 2.18\left[\frac{\alpha DnFv}{RT}\right]^{1/2} exp\left[\frac{-\alpha^2 nF(E_{p,a}-E_{p,c})}{RT}\right] \qquad (3.4)$$

Where $E_{p,a}$ is the potential of the anodic peak, $E_{p,c}$ is the potential of the cathodic peak, v is the scan rate, k_{app} is the apparent rate constant, D is the diffusion coefficient calculated using the Randles-Sevcik equation, R is the ideal gas constant, T is the absolute temperature, F is the Faraday constant, and n is the number of electrons transferred. Electron transfer rate

constants for AQS across the pH range studied are listed in Table 3.1. k_{app} is plotted logarithmically against pH for both AQS and ITO|Pyr|Pyr(AQ)$_2$ in Figure 3.16. Similar to the k_{app} dependence on pH exhibited by ITO|Pyr|Pyr(AQ)$_2$, the electron transfer rate constant for AQS increases with increasing pH. As discussed in section 3.2.3, the increase in k_{app} may not reflect the change in proton activity across the pH range, but instead may be due to the variation in buffer composition.[59] Nevertheless, it is evident that both the kinetic and thermodynamic properties of proton-coupled electron transfer of anthraquinone are retained upon immobilization to an ITO electrode though non-covalent π-π interactions.

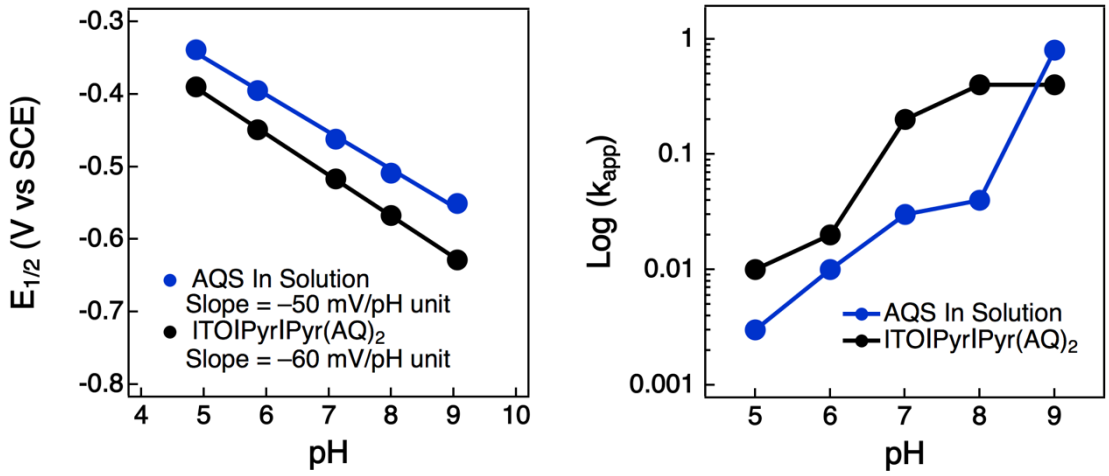

Figure 3.16. $E_{1/2}$ vs pH plot (left) and Log(k_{app}) vs pH plot (right) for ITO|Pyr|Pyr(AQ)$_2$ and AQS between pH 5 and 9.

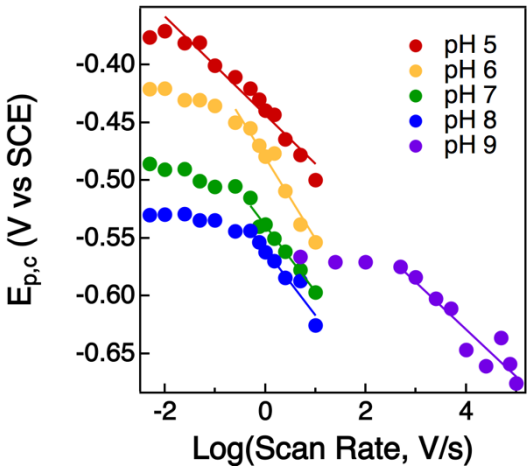

Figure 3.17. Plots of $E_{p,c}$ vs the log of the scan rate for AQS at varying pH. The slopes linear portions of the plots were used to determine the electron transfer coefficient, α, using Equation 3.3. The relatively fast electron transfer at pH 9 required faster scan rates to reach the irreversible region.

3.3 Conclusions

Pyrene-appended Pyr(AQ)$_2$ was successfully immobilized onto pyrene-bound indium tin oxide (ITO) electrodes using a versatile non-covalent attachment method. X-ray photoelectron spectroscopy and cyclic voltammetry confirmed the attachment of Pyr(AQ)$_2$ on the surface. Facile electron transfer between the ITO electrode and immobilized Pyr(AQ)$_2$ is observed across a range of pH conditions. In the pH range studied, the two-electron reduction of anthraquinone is coupled with two proton transfers to form dihydroanthraquinone. The electrochemical behavior of immobilized Pyr(AQ)$_2$ aligns with the pH-dependent cyclic voltammetry of AQS dissolved in buffered solution. These results highlight the thermodynamic similarities between proton-coupled electron transfer of anthraquinone in solution and on the ITO surface. Kinetic analysis of the electron transfer for both ITO|Pyr|Pyr(AQ)$_2$ and AQS in solution exhibits an increase in electron transfer rate constant with increasing pH, suggesting faster electron transfer at higher pH. The retention of molecular character and proton-coupled electron transfer processes using this

attachment method is a critical component of its applicability for heterogenizing redox catalysts onto electrodes.

3.4 Experimental Details

General Procedures

All reactions and manipulations were performed under an atmosphere of N_2 unless otherwise specified. Solvents were degassed by sparging with argon. Non-aqueous solvents were dried by passing through columns of neutral alumina or molecular sieves in an inert atmosphere. ITO on boro-aluminosilicate glass with a thickness of 0.5 mm and a sheet resistance of 5–15 Ω/sq was purchased from Delta Technologies. 1-Vinylpyrene[50] and 1-[bis(2-anthraquinonyl)aminomethyl]pyrene[51] were prepared using previously published procedures. All other materials and reagents were purchased from commercial suppliers and used without purification (Aldrich and Fisher). All buffers were prepared with water purified by a Barnstead NANOpure ultrapure water system. The pH of buffered solutions was measured using a Thermo Scientific Orion Star A216 pH meter.

Physical Methods

X-ray photoelectron spectra were acquired with a Kratos Analytical AXIS Supra spectrometer utilizing monochromatic Al Kα radiation (1486.7 eV, 250 W) under ultra-high vacuum (UHV) conditions (~10−9 Torr). Survey spectra were collected with a pass energy of 160 eV and high-resolution scans were performed with a pass energy of 20 eV. The binding energies were referred to the C 1s signal at 285 eV. Spectral data was analyzed using Computer Aided Surface Analysis for X-ray Photoelectron Spectroscopy (CasaXPS). Shirley or linear backgrounds and Gaussian-Lorentzian lineshapes were used to model peaks.

Electrochemical Experiments

Three-electrode cyclic voltammetry experiments were performed with a Pine Wavedriver 10 potentiostat and Aftermath software (Version 1.4.7881). Modified ITO electrodes were cycled between 0 and –0.75 V vs SCE (saturated calomel electrode) prior to analysis to ensure retention of immobilized species throughout electrochemical experiments. Aqueous experiments were performed in 100 mM buffered solutions (pH 5 and 6: citrate buffer, pH 7 and 8: 4-(2-hydroxyethyl)-1-piperazineethanesulfonic acid (4-(2-hydroxyethyl)-1-piperazineethanesulfonic acid , (HEPES) buffer, pH 9: borate buffer) with 100 mM KCl as the supporting electrolyte and non-aqueous experiments were performed in 100 mM NBu_4PF_6 in anhydrous dimethylformamide (DMF). Solution-phase experiments were performed using a 1 mm diameter glassy carbon disk working electrode. A glassy carbon rod was used as the counter electrode in all electrochemical experiments. Aqueous potentials are referenced to SCE and non-aqueous potentials are referenced to $Fe(C_5H_5)_2^{+/0}$. Chronoamperometry was performed on a 1 mM $Fe(C_5H_5)_2$ solution in CH_3CN with 100 mM NBu_4PF_6 as electrolyte in order to determine the electroactive surface area of the glassy carbon disk working electrode. After a 15 second induction period at –0.51 V vs $Fe(C_5H_5)_2^{+/0}$, the potential was stepped to 0.49 V vs $Fe(C_5H_5)_2^{+/0}$ and the current decay was recorded. The electroactive surface area was then calculated using the Cottrell equation, the literature value for the diffusion constant of $Fe(C_5H_5)_2$ in CH_3CN (2.4×10^{-5} cm^2/s),[61] and the slope of the plot of the current vs $(time)^{1/2}$ for $0.01\ s \leq time \leq 0.2\ s$. All reported peak current densities are corrected for capacitive currents using the Regression baseline mode in Aftermath software.

Substrate Modification

ITO electrodes were cleaned by immersing samples in a series of solvents at 50 °C for 10 minutes each. The order of solvents was as follows: trichloroethylene, acetone, and methanol. The electrodes were rinsed with H_2O and dried under a stream of air after each solvent. Electrodes were functionalized immediately after cleaning. Clean ITO samples were placed in vial, ITO side facing up, and immersed in a 1 mM solution of 1-vinylpyrene in anhydrous toluene. The solution was heated to 65 °C for 24 h. The samples were removed from the vial and rinsed with anhydrous toluene and CH_2Cl_2 to yield pyrene-modified ITO (ITO|Pyr). ITO|Pyr samples were placed in a 2.5 mM solution of 1-[bis(2-anthraquinonyl)aminomethyl]pyrene ($Pyr(AQ)_2$) in anhydrous CH_2Cl_2 for 12 h. The samples were removed from the solution, rinsed with anhydrous CH_3CN to remove loosely bound species, and dried to give non-covalently modified ITO|Pyr|$Pyr(AQ)_2$.

3.5 References

1. Veerbeek, J.; Huskens, J., Applications of Monolayer-Functionalized H-Terminated Silicon Surfaces: A Review. *Small Methods* **2017,** *1*, 1700072.

2. Pujari, S. P.; Scheres, L.; Marcelis, A. T. M.; Zuilhof, H., Covalent Surface Modification of Oxide Surfaces. *Angew. Chem. Int. Ed.* **2014,** *53*, 6322-6356.

3. Vericat, C.; Vela, M. E.; Corthey, G.; Pensa, E.; Cortes, E.; Fonticelli, M. H.; Ibanez, F.; Benitez, G. E.; Carro, P.; Salvarezza, R. C., Self-assembled monolayers of thiolates on metals: a review article on sulfur-metal chemistry and surface structures. *RSC Adv.* **2014,** *4*, 27730-27754.

4. Murray, R. W.; Goodenough, J. B.; Albery, W. J., Modified Electrodes: Chemically Modified Electrodes for Electrocatalysis [and Discussion]. *Philos. Trans. Royal Soc. A* **1981,** *302*, 253-265.

5. Reuillard, B.; Ly, K. H.; Rosser, T. E.; Kuehnel, M. F.; Zebger, I.; Reisner, E., Tuning Product Selectivity for Aqueous CO2 Reduction with a Mn(bipyridine)-pyrene Catalyst Immobilized on a Carbon Nanotube Electrode. *J. Am. Chem. Soc.* **2017,** *139*, 14425-14435.

6. Kang, P.; Zhang, S.; Meyer, T. J.; Brookhart, M., Rapid Selective Electrocatalytic Reduction of Carbon Dioxide to Formate by an Iridium Pincer Catalyst Immobilized on Carbon Nanotube Electrodes. *Angew. Chem. Int. Ed.* **2014,** *53*, 8709-8713.

7. Rosser, T. E.; Windle, C. D.; Reisner, E., Electrocatalytic and Solar-Driven CO2 Reduction to CO with a Molecular Manganese Catalyst Immobilized on Mesoporous TiO2. *Angew. Chem. Int. Ed.* **2016,** *55*, 7388-7392.

8. Chaki, N. K.; Vijayamohanan, K., Self-assembled monolayers as a tunable platform for biosensor applications. *Biosens. Bioelectron.* **2002,** *17*, 1-12.

9. Wang, Y.; Zhou, Y.; Sokolov, J.; Rigas, B.; Levon, K.; Rafailovich, M., A potentiometric protein sensor built with surface molecular imprinting method. *Biosens. Bioelectron.* **2008,** *24*, 162-166.

10. Bullock, M.; Das, A. K.; Appel, A. M., Surface Immobilization of Molecular Electrocatalysts for Energy Conversions. *Chem.: Eur. J.* **2017**, n/a-n/a.

11. Tran, P. D.; Le Goff, A.; Heidkamp, J.; Jousselme, B.; Guillet, N.; Palacin, S.; Dau, H.; Fontecave, M.; Artero, V., Noncovalent Modification of Carbon Nanotubes with Pyrene-Functionalized Nickel Complexes: Carbon Monoxide Tolerant Catalysts for Hydrogen Evolution and Uptake. *Angew. Chem. Int. Ed.* **2011,** *50*, 1371-1374.

12. Wadsworth, B. L.; Beiler, A. M.; Khusnutdinova, D.; Jacob, S. I.; Moore, G. F., Electrocatalytic and Optical Properties of Cobaloxime Catalysts Immobilized at a Surface-Grafted Polymer Interface. *ACS Catal.* **2016,** *6*, 8048-8057.

13. Blakemore, J. D.; Gupta, A.; Warren, J. J.; Brunschwig, B. S.; Gray, H. B., Noncovalent Immobilization of Electrocatalysts on Carbon Electrodes for Fuel Production. *J. Am. Chem. Soc.* **2013,** *135*, 18288-18291.

14. Li, F.; Zhang, B.; Li, X.; Jiang, Y.; Chen, L.; Li, Y.; Sun, L., Highly Efficient Oxidation of Water by a Molecular Catalyst Immobilized on Carbon Nanotubes. *Angew. Chem. Int. Ed.* **2011,** *50*, 12276-12279.

15. Jurss, J. W.; Concepcion, J. C.; Norris, M. R.; Templeton, J. L.; Meyer, T. J., Surface Catalysis of Water Oxidation by the Blue Ruthenium Dimer. *Inorg. Chem.* **2010,** *49*, 3980-3982.

16. Fukushima, T.; Drisdell, W.; Yano, J.; Surendranath, Y., Graphite-Conjugated Pyrazines as Molecularly Tunable Heterogeneous Electrocatalysts. *J. Am. Chem. Soc.* **2015,** *137*, 10926-10929.

17. Oh, S.; Gallagher, J. R.; Miller, J. T.; Surendranath, Y., Graphite-Conjugated Rhenium Catalysts for Carbon Dioxide Reduction. *J. Am. Chem. Soc.* **2016,** *138*, 1820-1823.

18. Jackson, M. N.; Oh, S.; Kaminsky, C. J.; Chu, S. B.; Zhang, G.; Miller, J. T.; Surendranath, Y., Strong Electronic Coupling of Molecular Sites to Graphitic Electrodes via Pyrazine Conjugation. *J. Am. Chem. Soc.* **2018,** *140*, 1004-1010.

19. Chen, Z.; Concepcion, J. J.; Hull, J. F.; Hoertz, P. G.; Meyer, T. J., Catalytic water oxidation on derivatized nanoITO. *Dalton Trans.* **2010,** *39*, 6950-6952.

20. Rosser, T. E.; Gross, M. A.; Lai, Y.-H.; Reisner, E., Precious-metal free photoelectrochemical water splitting with immobilised molecular Ni and Fe redox catalysts. *Chem. Sci.* **2016**.

21. Maurin, A.; Robert, M., Noncovalent Immobilization of a Molecular Iron-Based Electrocatalyst on Carbon Electrodes for Selective, Efficient CO2-to-CO Conversion in Water. *J. Am. Chem. Soc.* **2016,** *138*, 2492-2495.

22. Das, A. K.; Engelhard, M. H.; Lense, S.; Roberts, J. A. S.; Bullock, R. M., Covalent attachment of diphosphine ligands to glassy carbon electrodes via Cu-catalyzed alkyne-azide cycloaddition. Metallation with Ni(ii). *Dalton Trans.* **2015,** *44*, 12225-12233.

23. Mukherjee, S.; Mukherjee, A.; Bhagi-Damodaran, A.; Mukherjee, M.; Lu, Y.; Dey, A., A biosynthetic model of cytochrome c oxidase as an electrocatalyst for oxygen reduction. *Nat. Commun.* **2015,** *6*, 8467.

24. Öztaş, B.; Akyüz, D.; Koca, A., Immobilization of alkynyl functionalized manganese phthalocyanine via click electrochemistry for electrocatalytic oxygen evolution reaction. *Phys. Chem. Chem. Phys.* **2017,** *19*, 26121-26131.

25. Lei, H.; Liu, C.; Wang, Z.; Zhang, Z.; Zhang, M.; Chang, X.; Zhang, W.; Cao, R., Noncovalent Immobilization of a Pyrene-Modified Cobalt Corrole on Carbon Supports for Enhanced Electrocatalytic Oxygen Reduction and Oxygen Evolution in Aqueous Solutions. *ACS Catal.* **2016,** *6*, 6429-6437.

26. McCrory, C. C. L.; Devadoss, A.; Ottenwaelder, X.; Lowe, R. D.; Stack, T. D. P.; Chidsey, C. E. D., Electrocatalytic O2 Reduction by Covalently Immobilized Mononuclear Copper(I) Complexes: Evidence for a Binuclear Cu2O2 Intermediate. *J. Am. Chem. Soc.* **2011,** *133*, 3696-3699.

27. Joglekar, M.; Nguyen, V.; Pylypenko, S.; Ngo, C.; Li, Q.; O'Reilly, M. E.; Gray, T. S.; Hubbard, W. A.; Gunnoe, T. B.; Herring, A. M.; Trewyn, B. G., Organometallic Complexes Anchored to Conductive Carbon for Electrocatalytic Oxidation of Methane at Low Temperature. *J. Am. Chem. Soc.* **2016,** *138*, 116-125.

28. Demeter, E. L.; Hilburg, S. L.; Washburn, N. R.; Collins, T. J.; Kitchin, J. R., Electrocatalytic Oxygen Evolution with an Immobilized TAML Activator. *J. Am. Chem. Soc.* **2014,** *136*, 5603-5606.

29. Berben, L. A.; Peters, J. C., Hydrogen evolution by cobalt tetraimine catalysts adsorbed on electrode surfaces. *Chem. Comm.* **2010,** *46*, 398-400.

30. Das, A.; Stahl, S. S., Noncovalent Immobilization of Molecular Electrocatalysts for Chemical Synthesis: Efficient Electrochemical Alcohol Oxidation with a Pyrene–TEMPO Conjugate. *Angew. Chem. Int. Ed.* **2017,** *56*, 8892-8897.

31. Beiler, A. M.; Khusnutdinova, D.; Jacob, S. I.; Moore, G. F., Solar Hydrogen Production Using Molecular Catalysts Immobilized on Gallium Phosphide (111)A and (111)B Polymer-Modified Photocathodes. *ACS Appl. Mater. Interfaces* **2016,** *8*, 10038-10047.

32. Beiler, A. M.; Khusnutdinova, D.; Wadsworth, B. L.; Moore, G. F., Cobalt Porphyrin–Polypyridyl Surface Coatings for Photoelectrosynthetic Hydrogen Production. *Inorg. Chem.* **2017,** *56*, 12178-12185.

33. Khusnutdinova, D.; Beiler, A. M.; Wadsworth, B. L.; Jacob, S. I.; Moore, G. F., Metalloporphyrin-modified semiconductors for solar fuel production. *Chem. Sci.* **2017,** *8*, 253-259.

34. Lattimer, J. R. C.; Blakemore, J. D.; Sattler, W.; Gul, S.; Chatterjee, R.; Yachandra, V. K.; Yano, J.; Brunschwig, B. S.; Lewis, N. S.; Gray, H. B., Assembly, characterization, and

electrochemical properties of immobilized metal bipyridyl complexes on silicon(111) surfaces. *Dalton Trans.* **2014,** *43*, 15004-15012.

35. Leung, J. J.; Warnan, J.; Nam, D. H.; Zhang, J. Z.; Willkomm, J.; Reisner, E., Photoelectrocatalytic H2 evolution in water with molecular catalysts immobilised on p-Si via a stabilising mesoporous TiO2 interlayer. *Chem. Sci.* **2017,** *8*, 5172-5180.

36. Seo, J.; Pekarek, R. T.; Rose, M. J., Photoelectrochemical operation of a surface-bound, nickel-phosphine H2 evolution catalyst on p-Si(111): a molecular semiconductor|catalyst construct. *Chem. Comm.* **2015,** *51*, 13264-13267.

37. Joya, K. S.; Morlanés, N.; Maloney, E.; Rodionov, V.; Takanabe, K., Immobilization of a molecular cobalt electrocatalyst by hydrophobic interaction with a hematite photoanode for highly stable oxygen evolution. *Chem. Comm.* **2015,** *51*, 13481-13484.

38. Downes, C. A.; Marinescu, S. C., Efficient Electrochemical and Photoelectrochemical H2 Production from Water by a Cobalt Dithiolene One-Dimensional Metal–Organic Surface. *J. Am. Chem. Soc.* **2015,** *137*, 13740-13743.

39. Forster, R. J.; O'Kelly, J. P., Protonation reactions of anthraquinone-2,7-disulphonic acid in solution and within monolayers. *J. Electroanal. Chem.* **2001,** *498*.

40. Jackson, M. N.; Pegis, M. L.; Surendranath, Y., Graphite-Conjugated Acids Reveal a Molecular Framework for Proton-Coupled Electron Transfer at Electrode Surfaces. *ACS Cent. Sci.* **2019,** *5*, 831-841.

41. Son, E. J.; Kim, J. H.; Kim, K.; Park, C. B., Quinone and its derivatives for energy harvesting and storage materials. *J. Mater. Chem. A* **2016,** *4*, 11179-11202.

42. Quan, M.; Sanchez, D.; Wasylkiw, M. F.; Smith, D. K., Voltammetry of Quinones in Unbuffered Aqueous Solution: Reassessing the Roles of Proton Transfer and Hydrogen

Bonding in the Aqueous Electrochemistry of Quinones. *J. Am. Chem. Soc.* **2007,** *129*, 12847-12856.

43. Abhayawardhana, A. D.; Sutherland, T. C., Heterogeneous proton-coupled electron transfer of a hydroxy-anthraquinone self-assembled monolayer. *J. Electroanal. Chem.* **2011,** *653*, 50-55.

44. Ghanem, M. A.; Kocak, I.; Al-Mayouf, A.; AlHoshan, M.; Bartlett, P. N., Covalent modification of carbon nanotubes with anthraquinone by electrochemical grafting and solid phase synthesis. *Electrochim. Acta* **2012,** *68*, 74-80.

45. Abhayawardhana, A. D.; Sutherland, T. C., Heterogeneous Proton-Coupled Electron Transfer of an Aminoanthraquinone Self-Assembled Monolayer. *J. Phys. Chem. C* **2009,** *113*, 4915-4924.

46. Nagata, M.; Kondo, M.; Suemori, Y.; Ochiai, T.; Dewa, T.; Ohtsuka, T.; Nango, M., Electron transfer of quinone self-assembled monolayers on a gold electrode. *Colloids Surf. B* **2008,** *64*, 16-21.

47. Batchelor-McAuley, C.; Kozub, B. R.; Menshykau, D.; Compton, R. G., Voltammetric Responses of Surface-Bound and Solution-Phase Anthraquinone Moieties in the Presence of Unbuffered Aqueous Media. *J. Phys. Chem. C* **2011,** *115*, 714-718.

48. Zhang, W.; Rosendahl, S. M.; Burgess, I. J., Coupled Electron/Proton Transfer Studies of Benzoquinone-Modified Monolayers. *J. Phys. Chem. C* **2010,** *114*, 2738-2745.

49. March, G.; Reisberg, S.; Piro, B.; Pham, M. C.; Delamar, M.; Noel, V.; Odenthal, K.; Hibbert, D. B.; Gooding, J. J., Electrochemical kinetic analysis of a 1,4-hydroxynaphthoquinone self-assembled monolayer. *J. Electroanal. Chem.* **2008,** *622*, 37-43.

50. Albagli, D.; Bazan, G. C.; Schrock, R. R.; Wrighton, M. S., New functional polymers prepared by ring-opening metathesis polymerization: study of the quenching of luminescence of pyrene end groups by ferrocene or phenothiazine centers in the polymers. *J. Phys. Chem.* **1993,** *97*, 10211-10216.

51. Bourourou, M.; Elouarzaki, K.; Lalaoui, N.; Agnès, C.; Le Goff, A.; Holzinger, M.; Maaref, A.; Cosnier, S., Supramolecular Immobilization of Laccase on Carbon Nanotube Electrodes Functionalized with (Methylpyrenylaminomethyl)anthraquinone for Direct Electron Reduction of Oxygen. *Chem.: Eur. J.* **2013,** *19*, 9371-9375.

52. Hotchkiss, P. J.; Jones, S. C.; Paniagua, S. A.; Sharma, A.; Kippelen, B.; Armstrong, N. R.; Marder, S. R., The Modification of Indium Tin Oxide with Phosphonic Acids: Mechanism of Binding, Tuning of Surface Properties, and Potential for Use in Organic Electronic Applications. *Acc. Chem. Res.* **2012,** *45*, 337-346.

53. Jansen, R. J. J.; van Bekkum, H., XPS of nitrogen-containing functional groups on activated carbon. *Carbon* **1995,** *33*, 1021-1027.

54. Faulkner, A. J. B. a. L. R., *Electrochemical Methods*. Second ed.; John Wiley & Sons, Inc.: 2001.

55. Stotter, J.; Show, Y.; Wang, S.; Swain, G., Comparison of the Electrical, Optical, and Electrochemical Properties of Diamond and Indium Tin Oxide Thin-Film Electrodes. *Chem. Mater.* **2005,** *17*, 4880-4888.

56. Laviron, E., The use of linear potential sweep voltammetry and of a.c. voltammetry for the study of the surface electrochemical reaction of strongly adsorbed systems and of redox modified electrodes. *J. Electroanal. Chem. Interf. Electrochem.* **1979,** *100*, 263-270.

57. Smalley, J. F.; Feldberg, S. W.; Chidsey, C. E. D.; Linford, M. R.; Newton, M. D.; Liu, Y.-P., The Kinetics of Electron Transfer Through Ferrocene-Terminated Alkanethiol Monolayers on Gold. *J. Phys. Chem.* **1995,** *99*, 13141-13149.

58. Finklea, H. O.; Haddox, R. M., Coupled electron/proton transfer of galvinol attached to SAMs on gold electrodes. *Phys. Chem. Chem. Phys.* **2001,** *3*, 3431-3436.

59. Costentin, C., Electrochemical Approach to the Mechanistic Study of Proton-Coupled Electron Transfer. *Chem. Rev.* **2008,** *108*, 2145-2179.

60. Klingler, R. J.; Kochi, J. K., Electron-transfer kinetics from cyclic voltammetry. Quantitative description of electrochemical reversibility. *J. Phys. Chem.* **1981,** *85*, 1731-1741.

61. Kadish, K. M.; Ding, J. Q.; Malinski, T., Resistance of nonaqueous solvent systems containing tetraalkylammonium salts. Evaluation of heterogeneous electron transfer rate constants for the ferrocene/ferrocenium couple. *Anal. Chem.* **1984,** *56*, 1741-1744.

CHAPTER 4

Immobilization of a Molecular Water Oxidation Catalyst onto Indium Tin Oxide Through π-π Interactions

4.1 Introduction

The $4e^-/4H^+$ oxidation of H_2O to produce O_2 and H^+ is of great interest for the generation of renewable fuels.[1] The selectivity of molecular catalysts is particularly advantageous for electrocatalytic water oxidation in order to mitigate the formation of the $2e^-/2H^+$ oxidized product, H_2O_2.[1] Exceptional progress has been made in the last 40 years developing efficient and robust molecular electrocatalysts for water oxidation.[1] Licheng Sun developed a class of highly stable molecular ruthenium complexes containing tetradentate 2,2-bipyridine-6,6-dicarboxylic acid (bda) ligands that exhibit turnover numbers of up to 2000 and turn over frequencies of up to 41 s^{-1} (Scheme 4.1, left).[2-6] The bda ligands result in a distorted octahedral coordination environment that is hypothesized to enable generation of a seven-coordinate Ru(V)=O intermediate.[2-6] These complexes have since been immobilized onto carbon supports in order to generate chemically modified electrodes (CMEs) for catalytic water oxidation.[7-8] In an attempt to prepare CMEs for catalytic water oxidation utilizing the hybrid attachment approach developed in the Yang lab, a derivative of Sun's Ru-bda catalysts containing axial pyrene-bound pyridine ligands is immobilized onto ITO|Pyr (Scheme 4.1, right).

Scheme 4.1. Sun's class of water oxidation catalysts (left) and a schematic representation of the attachment of a Ru-bda catalyst to ITO|Pyr via π-π interactions (right).

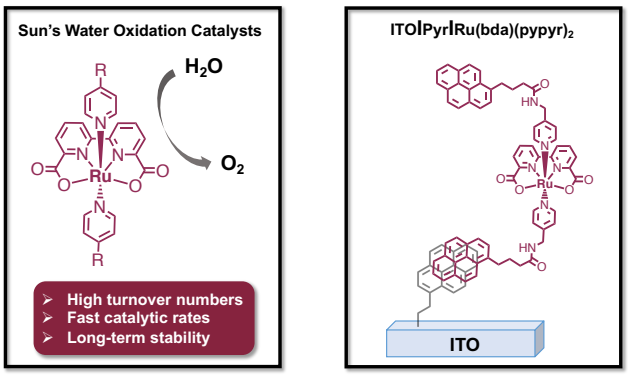

4.2 Results and Discussion

1-Vinylpyrene[9] and Ru(bda)(pypyr)$_2$ (pypyr = 4-(pyren-1-yl)-N-(pyridine-4-ylmethyl)butanamide)[7] were prepared using reported procedures. Indium tin oxide (ITO) was covalently modified with 1-vinylpyrene by immersing clean ITO samples in toluene solutions of 1-vinylpyrene at 65 °C for 24 h to yield pyrene-modified ITO (ITO|Pyr). Subsequent attachment of Ru(bda)(pypyr)$_2$ was achieved by immersing ITO|Pyr in CH_3OH solutions of Ru(bda)(pypyr)$_2$ for 12 h, yielding non-covalently modified ITO|Pyr|Ru(bda)(pypyr)$_2$. The average Ru(bda)(pypyr)$_2$ coverage, calculated by integrating the anodic peak of the cyclic voltammograms (CVs) of ITO|Pyr|Ru(bda)(pypyr)$_2$ at slow scan rates, was determined to be 2 pmol/cm^2.

The cyclic voltammetry of ITO|Pyr|Ru(bda)(pypyr)$_2$ in 100 mM Na_2SO_4 is displayed in the red trace in Figure 4.1. The CV exhibits a redox couple with an $E_{1/2}$ of 0.32 V vs SCE, assigned as the $Ru^{III/II}$ couple of Ru(bda)(pypyr)$_2$,[7-8] and a large increase in current with an onset potential of 0.65 V vs SCE attributed to catalytic water oxidation by Ru(bda)(pypyr)$_2$. Figure 4.1 also shows the CVs of bare ITO (black trace) and ITO|Pyr (yellow trace) in 100 mM Na_2SO_4. Both CVs lack the redox couple at 0.32 V vs SCE and the large increase in current at 0.65 V vs SCE, confirming these features are attributed to Ru(bda)(pypyr)$_2$ in the CV of ITO|Pyr|Ru(bda)(pypyr)$_2$. The CV of bare ITO soaked in a solution of Ru(bda)(pypyr)$_2$ (denoted as ITO|Ru(bda)(pypyr)$_2$) is shown in the blue trace of Figure 4.1. ITO|Ru(bda)(pypyr)$_2$ exhibits an irreversible oxidation at 0.33 V vs SCE and a slight increase in current at 0.70 V vs SCE. These results suggest adsorption of Ru(bda)(pypyr)$_2$ without the pyrene layer, likely due to hydrogen bonding between the pypyr ligand and the hydroxyl groups that terminate the electrode surface.[10] However, the irreversibility of the oxidative

feature at 0.33 V vs SCE suggests that Ru(bda)(pypyr)$_2$ falls off of the bare ITO surface during voltammetry and highlights the superior stability of ITO|Pyr|Ru(bda)(pypyr)$_2$ due to π-π interactions between Ru(bda)(pypyr)$_2$ and the surface-bound pyrene layer.

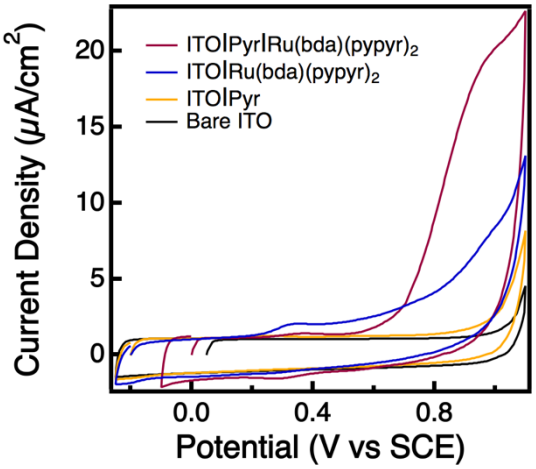

Figure 4.1. Cyclic voltammetry of ITO, ITO | Pyr, and ITO | Pyr | Ru(bda)(pypyr)$_2$ in 100 mM Na_2SO_4 performed under N_2.

Figure 4.2 displays the variable scan rate cyclic voltammetry of the $Ru^{III/II}$ couple of ITO | Pyr | Ru(bda)(pypyr)$_2$ in 100 mM Na_2SO_4 (left) and the corresponding peak current density vs square root of scan rate plot (right). Surprisingly, the peak current density varies linearly with the square root of scan rate, indicating a diffusion-limited electrochemical process. The insolubility of Ru(bda)(pypyr)$_2$ in water however, suggests that the catalyst remains on the surface throughout voltammetry. Multiple reports studying ferrocene attached to gold electrodes through polymeric linkers demonstrate diffusion-limited current dependence on scan rate when sufficiently long linkers are utilized.[11-15] Therefore, it is reasonable to conclude that electron transfer to Ru(bda)(pypyr)$_2$ is diffusion-limited despite attachment of Ru(bda)(pypyr)$_2$ to the surface due to the long pypyr linker separating the Ru metal center from the electrode.

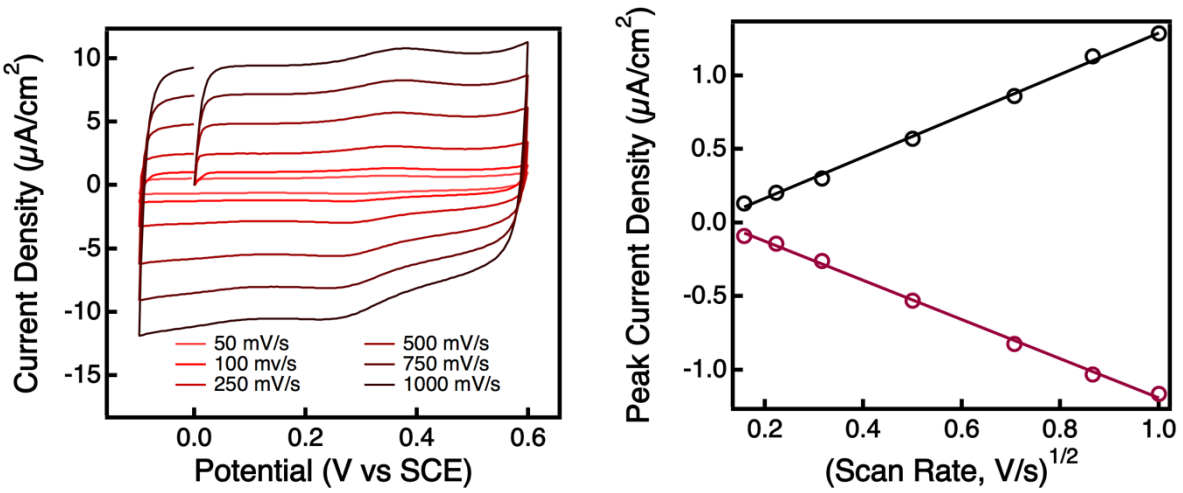

Figure 4.2. Variable scan rate cyclic voltammetry of the $Ru^{III/II}$ couple of ITO | Pyr | $Ru(bda)(pypyr)_2$ in 100 mM Na_2SO_4 performed under N_2 (left) and the corresponding peak current vs square root of scan rate plot (right).

In order to probe the viability of ITO | Pyr | $Ru(bda)(pypyr)_2$ as an electrode for catalytic water oxidation, controlled potential electrolysis was performed in 100 mM Na_2SO_4 at 0.8 V vs SCE. As shown in the current density vs time plot in Figure 4.3 (left), current density decreases to negligible values within 60 s. Cyclic voltammetry of the electrode before and after electrolysis is displayed in Figure 4.5 (right). After electrolysis, the $Ru^{III/II}$ couple is no longer present and the onset of increased current density attributed to water oxidation shifts anodically to 0.95 V vs SCE. These results suggest loss of catalyst from the electrode surface due to either decomposition or desorption from the electrode under electrocatalytic conditions. $Ru(bda)(pypyr)_2$ adsorbed onto multi-walled carbon nanotubes through π-π interactions was previously shown to retain its molecular character throughout 10 h of sustained electrolysis.[7] However, a diazonium derivative of $Ru(bda)(L)_2$ electrochemically grafted onto glassy carbon electrodes demonstrated gradual decomposition to RuO_2 under electrocatalytic conditions. The RuO_2 film remained catalytically active for water oxidation, albeit at higher overpotentials than $Ru(bda)(L)_2$.[8] The CV of ITO | Pyr | $Ru(bda)(pypyr)_2$ after

electrolysis exhibits a large increase in current at 0.95 V vs SCE which is not exhibited in the CVs of bare ITO or ITO | Pyr. This large increase in current suggests the presence of a catalytically competent species on the electrode surface after electrolysis, such as RuO_2.[8, 16-17] Attempts were made to spectroscopically characterize the catalyst before and after electrolysis using X-ray photoelectron spectroscopy. Unfortunately, the low coverage of Ru(bda)(pypyr)$_2$ on the electrode surface prevented resolution of Ru 3d peaks in the XPS spectrum.

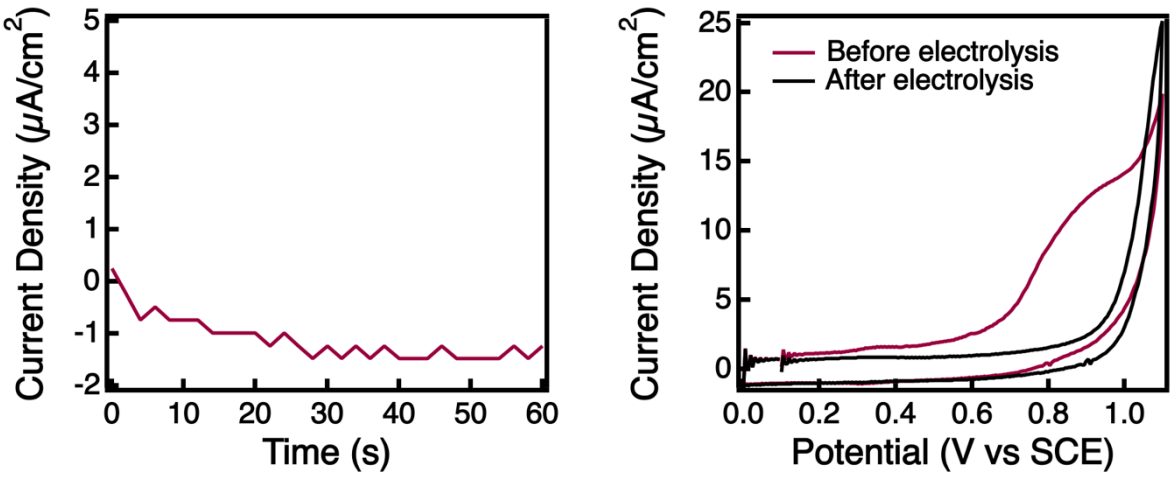

Figure 4.3. Controlled potential electrolysis of ITO | Pyr | Ru(bda)(pypyr)$_2$ performed in 100 mM Na_2SO_4 under N_2 at 0.8 V vs SCE (left) and the cyclic voltammetry before and after electrolysis.

4.3 Conclusions

A molecular water oxidation catalyst, Ru(bda)(pypyr)$_2$, was immobilized onto pyrene-bound indium tin oxide electrodes through π-π interactions. Cyclic voltammetry confirmed the presence of the catalyst on the surface. Interestingly, Ru(bda)(pypyr)$_2$ undergoes diffusion-limited electron-transfer despite its attachment to the electrode surface. During electrolysis, activity from the molecular electrocatalyst is lost, likely due to decomposition to RuO_2 which remains catalytically active on the surface of the electrode.

4.4 Experimental Details

General Procedures

All reactions and manipulations were performed under an atmosphere of N_2 unless otherwise specified. Solvents were degassed by sparging with argon. Non-aqueous solvents were dried by passing through columns of neutral alumina or molecular sieves in an inert atmosphere. ITO on boro-aluminosilicate glass with a thickness of 0.5 mm and a sheet resistance of 5–15 Ω/sq was purchased from Delta Technologies. 1-Vinylpyrene[9] and $Ru(bda)(pypyr)_2$ (bda = 2,2'-bipyridine-6,6'-dicarboxylic acid, pypyr = 4-(pyren-1-yl)-N-(pyridine-4-ylmethyl)butanamide)[7] were prepared using previously published procedures. All other materials and reagents were purchased from commercial suppliers and used without purification (Aldrich and Fisher).

Electrochemical Experiments

Three-electrode electrochemical experiments were performed with a Pine Wavedriver 10 potentiostat and Aftermath software (Version 1.4.7881). All experiments were performed in 100 mM Na_2SO_4. A glassy carbon rod and was used as the counter electrode and an SCE electrode was used as the reference. All reported peak current densities are corrected for capacitive currents using the Regression baseline mode in Aftermath software.

Substrate Modification

ITO electrodes were cleaned by immersing samples in a series of solvents at 50 °C for 10 minutes each. The order of solvents was as follows: trichloroethylene, acetone, and methanol. The electrodes were rinsed with H_2O and dried under a stream of air after each solvent. Electrodes were functionalized immediately after cleaning. Clean ITO samples were

placed in vial, ITO side facing up, and immersed in a 1 mM solution of 1-vinylpyrene in anhydrous toluene. The solution was heated to 65 °C for 24 h. The samples were removed from the vial and rinsed with anhydrous toluene and CH_2Cl_2 to yield pyrene-modified ITO (ITO|Pyr). ITO|Pyr samples were placed in a 2.5 mM solution of Ru(bda)(pypyr)$_2$ in anhydrous CH_3OH for 12 h. The samples were removed from the solution, rinsed with anhydrous CH_3OH to remove loosely bound species, and dried to give non-covalently modified ITO|Pyr|Ru(bda)(pypyr)$_2$.

4.5 References

1. Blakemore, J. D.; Crabtree, R. H.; Brudvig, G. W., Molecular Catalysts for Water Oxidation. *Chem. Rev.* **2015,** *115*, 12974-13005.

2. Duan, L.; Bozoglian, F.; Mandal, S.; Stewart, B.; Privalov, T.; Llobet, A.; Sun, L., A molecular ruthenium catalyst with water-oxidation activity comparable to that of photosystem II. *Nat. Chem.* **2012,** *4*, 418-423.

3. Nyhlén, J.; Duan, L.; Åkermark, B.; Sun, L.; Privalov, T., Evolution of O2 in a Seven-Coordinate RuIV Dimer Complex with a [HOHOH]− Bridge: A Computational Study. *Angew. Chem. Int. Ed.* **2010,** *49*, 1773-1777.

4. Duan, L.; Wang, L.; Inge, A. K.; Fischer, A.; Zou, X.; Sun, L., Insights into Ru-Based Molecular Water Oxidation Catalysts: Electronic and Noncovalent-Interaction Effects on Their Catalytic Activities. *Inorg. Chem.* **2013,** *52*, 7844-7852.

5. Wang, L.; Duan, L.; Wang, Y.; Ahlquist, M. S. G.; Sun, L., Highly efficient and robust molecular water oxidation catalysts based on ruthenium complexes. *Chem. Comm.* **2014,** *50*, 12947-12950.

6. Zhang, B.; Sun, L., Ru-bda: Unique Molecular Water-Oxidation Catalysts with Distortion Induced Open Site and Negatively Charged Ligands. *J. Am. Chem. Soc.* **2019,** *141*, 5565-5580.

7. Li, F.; Zhang, B.; Li, X.; Jiang, Y.; Chen, L.; Li, Y.; Sun, L., Highly Efficient Oxidation of Water by a Molecular Catalyst Immobilized on Carbon Nanotubes. *Angew. Chem. Int. Ed.* **2011,** *50*, 12276-12279.

8. Matheu, R.; Francàs, L.; Chernev, P.; Ertem, M. Z.; Batista, V.; Haumann, M.; Sala, X.; Llobet, A., Behavior of the Ru-bda Water Oxidation Catalyst Covalently Anchored on Glassy Carbon Electrodes. *ACS Catal.* **2015,** *5*, 3422-3429.

9. Albagli, D.; Bazan, G. C.; Schrock, R. R.; Wrighton, M. S., New functional polymers prepared by ring-opening metathesis polymerization: study of the quenching of luminescence of pyrene end groups by ferrocene or phenothiazine centers in the polymers. *J. Phys. Chem.* **1993,** *97*, 10211-10216.

10. Hotchkiss, P. J.; Jones, S. C.; Paniagua, S. A.; Sharma, A.; Kippelen, B.; Armstrong, N. R.; Marder, S. R., The Modification of Indium Tin Oxide with Phosphonic Acids: Mechanism of Binding, Tuning of Surface Properties, and Potential for Use in Organic Electronic Applications. *Acc. Chem. Res.* **2012,** *45*, 337-346.

11. Steentjes, T.; Jonkheijm, P.; Huskens, J., Electron Transfer Processes in Ferrocene-Modified Poly(ethylene glycol) Monolayers on Electrodes. *Langmuir* **2017,** *33*, 11878-11883.

12. Hüsken, N.; Gębala, M.; La Mantia, F.; Schuhmann, W.; Metzler-Nolte, N., Mechanistic Studies of Fc-PNA(·DNA) Surface Dynamics Based on the Kinetics of Electron-Transfer Processes. *Chem.: Eur. J.* **2011,** *17*, 9678-9690.

13. Anne, A.; Bouchardon, A.; Moiroux, J., 3'-Ferrocene-Labeled Oligonucleotide Chains End-Tethered to Gold Electrode Surfaces: Novel Model Systems for Exploring Flexibility of Short DNA Using Cyclic Voltammetry. *J. Am. Chem. Soc.* **2003,** *125*, 1112-1113.

14. Anne, A.; Demaille, C., Dynamics of Electron Transport by Elastic Bending of Short DNA Duplexes. Experimental Study and Quantitative Modeling of the Cyclic Voltammetric Behavior of 3'-Ferrocenyl DNA End-Grafted on Gold. *J. Am. Chem. Soc.* **2006,** *128*, 542-557.

15. Anne, A.; Demaille, C., Electron Transport by Molecular Motion of redox-DNA Strands: Unexpectedly Slow Rotational Dynamics of 20-mer ds-DNA Chains End-Grafted onto Surfaces via C6 Linkers. *J. Am. Chem. Soc.* **2008,** *130*, 9812-9823.

16. Das, S. K.; Dutta, P. K., Synthesis and characterization of a ruthenium oxide–zeolite Y catalyst for photochemical oxidation of water to dioxygen1Dedicated to Professor Lovat V.C. Rees in recognition and appreciation of his lifelong devotion to zeolite science and his outstanding achievements in this field.1. *Micro. Meso. Mater.* **1998,** *22*, 475-483.

17. Zhang, Y.; Judkins, E. C.; McMillin, D. R.; Mehta, D.; Ren, T., Mesoporous Silica-Supported Ruthenium Oxide Nanoparticulates as Efficient Catalysts for Photoinduced Water Oxidation. *ACS Catal.* **2013,** *3*, 2474-2478.

CHAPTER 5

Understanding Photoelectrochemical Proton Reduction at Nanoporous Si Electrodes Modified with a Cobalt Bis(benzenedithiolate) Catalyst via π-π Interactions

5.1 Introduction

The integration of small band gap semiconductors with highly selective molecular proton or CO_2 reduction electrocatalysts is a promising strategy for efficient storage of solar energy in the form of chemical bonds.[1-2] Molecular electrocatalysts are advantageous for fuel-forming catalysis due to their tunable reactivity (*via* ligand design) and high selectivity.[3-6] Several methods have been employed to immobilize molecular catalysts onto semiconductor surfaces including direct covalent attachment[7-8] covalent attachment to TiO_2 layers on the semiconductor surface,[9-10] and incorporation into surface-deposited polymers such as Nafion membranes,[11] polyvinylpyridine,[12-16] or coordination polymers.[17] Attachment of molecular catalysts to semiconductor surfaces and subsequent analysis of the kinetic and energetic effects of catalyst attachment remains at the forefront of photoelectrochemical fuel generation research.

5.1.1 Surface Modification and Band Bending

While catalyst attachment to semiconducting electrodes can improve the kinetics of photoelectrochemical fuel-forming processes, it is important to consider the effects of semiconductor surface modification on the thermodynamics of such interfacial charge-transfer reactions. The driving force for photoelectrochemical charge transfer across a semiconductor|liquid interface is dictated by the degree of band bending within the semiconductor: greater band bending yields a larger driving force for light-driven interfacial charge transfer.[2, 18-19] Surface treatments, including molecular attachment through covalent bonds and catalyst adsorption, are well-known to modulate band bending at semiconductor|liquid junctions. [20-31] For example, the Lewis[21, 25-26] and Rose[22] groups have both demonstrated band edge modulation of Si(111) through the introduction of molecular

monolayer surface dipoles. Thorough analysis of the energetic effects of surface modification is therefore imperative in the design of efficient photoelectrochemical cells.

When a p-type semiconductor comes in contact with a solvated redox couple with a potential ($E(A/A^-)$) that lies between the energies of the semiconductor's fermi level (E_f) and conduction band (E_{CB}), the semiconductor equilibrates into depletion; majority carriers (holes) are transferred to solution and E_F rises to match $E(A/A^-)$ (Scheme 5.1, left). Within the bulk of the semiconductor, E_{CB} and E_{VB} (energy of the valence band) shift with E_F, but at the interface, E_{CB} and E_{VB} do not change. This energy gradient is represented by downward bending of E_{CB} and E_{VB}. [2, 18-19]

When a dipole is introduced to the surface of the semiconductor, the potential drop across the semiconductor|solution interface and the magnitude of band bending is modulated. Scheme 5.1 (right) demonstrates the effect of a positive surface dipole on the band bending of a p-type semiconductor in depletion. The positive dipole increases the potential drop across the surface, resulting in a larger shift in E_F upon equilibration with $E(A/A^-)$. Consequently, the positive dipole induces a greater shift in E_{CB} and E_{VB} in the bulk of the semiconductor and thus results in greater band bending within the semiconductor. Alternatively, introduction of a negative dipole at the interface will decrease the potential drop and result in less bend bending.[2, 18, 20-21, 32]

Scheme 5.1. Band diagrams of a p-type semiconductor before and after equilibration with a redox couple in solution without (left) and with (right) a surface dipole.

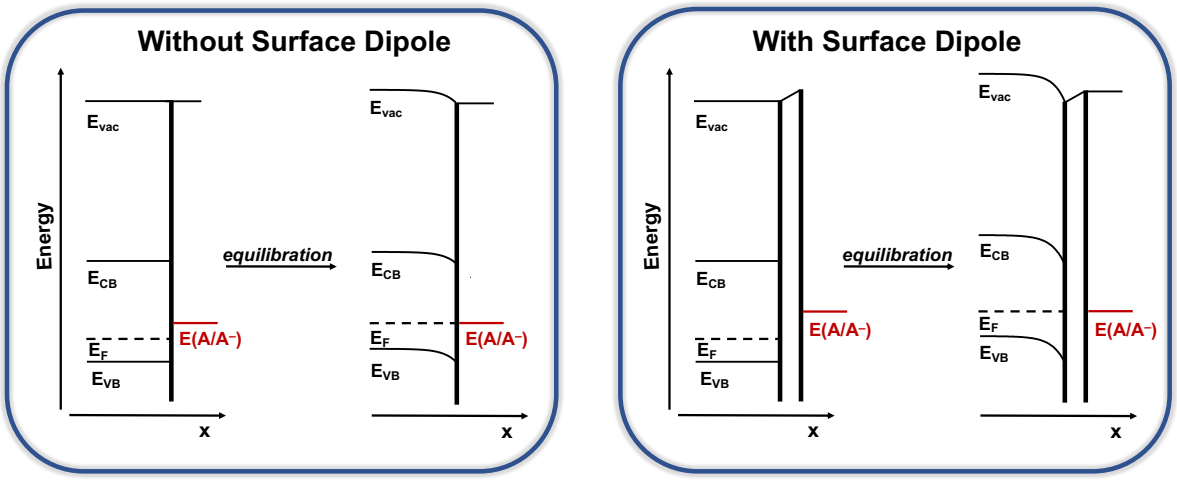

5.1.2 Intensity-Modulated High-Frequency Resistivity Impedance Spectroscopy

Intensity-modulated high-frequency resistivity (IMHFR) impedance spectroscopy is a recently developed technique that enables facile measurement of a semiconductor's flatband potential (V_{FB}).[23-24] V_{FB} is the potential at which a semiconductor's bands are no longer bent and marks the most positive potential (for p-type semiconductors) at which light-driven charge transfer from a semiconductor to solution is thermodynamically favored.[2, 18-19] The effects of surface modification on band bending can therefore be quantified by measuring V_{FB}: a change in V_{FB} upon surface modification indicates increased or decreased band bending within the semiconductor.

V_{FB} is most commonly measured using Mott-Schottky analysis. However, applying Mott-Schottky analysis to multijunction or nanoporous electrodes is challenging because separate resistive and capacitive components are required for each chemically distinct layer.[23] IMHFR impedance spectroscopy, on the other hand, can accurately measure V_{FB} for

complex nanostructured or multijunction electrodes. IMHFR impedance spectroscopy measures V_{FB} by comparing the resistance of a semiconductor's space-charge region (R_{SC}) in the dark and under illumination while sweeping the potential.[23-24] Measurement of only R_{SC} is achieved using a high frequency (100 kHz) which shorts all other circuit elements. R_{SC} is strongly correlated to the number of carriers at the electrode surface. Scheme 5.2 depicts the band energy effects of applying a positive potential to a p-type semiconductor in depletion (top) and relative light and dark R_{SC} at three potential regimes. Under depletion conditions (A), R_{SC} is large in the dark due to the lack of majority carriers, but drops significantly upon illumination as minority carriers are excited to the conduction band and driven toward the surface. Application of a positive potential increases the population of majority carriers in the space-charge region which effectively "unbends" the bands as shown in Scheme 5.2(B) and decreases the dark R_{SC}. When the flatband potential is reached (Scheme 5.2(C)), the population of majority carriers is restored and there is negligible difference between the light and dark R_{SC}. A plot of the difference in light and dark R_{SC} (ΔR_{SC}) vs applied potential thus enables measurement of V_{FB} where ΔR_{SC} approaches zero.[23-24]

Scheme 5.2. Band diagrams of a p-type semiconductor at three potential regimes (top) and the corresponding chopped-light resistivity measurements at the three potential regimes (bottom).

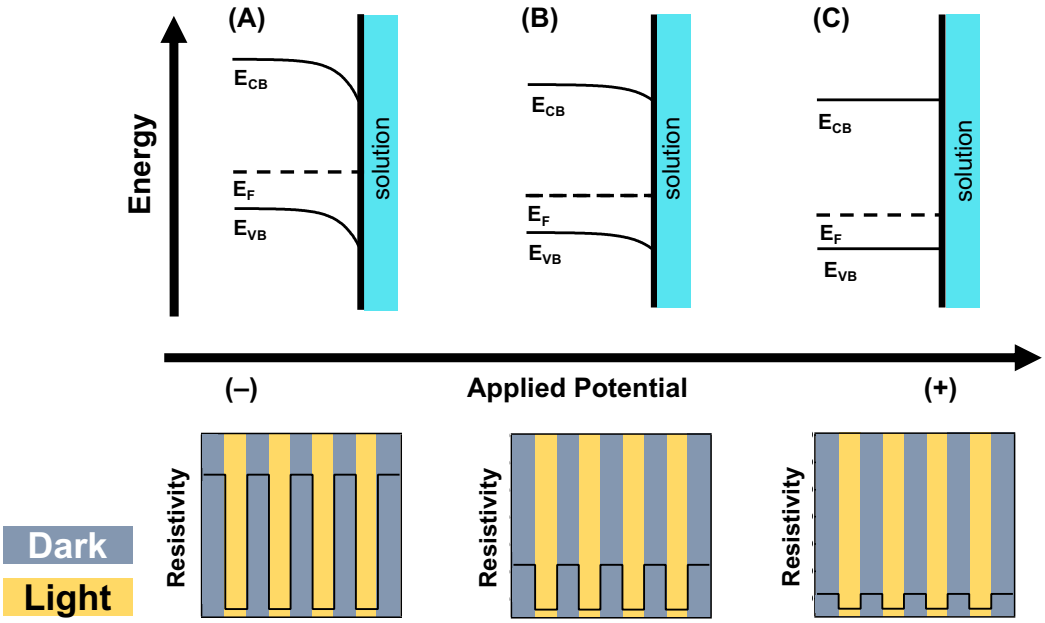

5.1.3 Catalyst Immobilization on Nanoporous Silicon Photoelectrodes

Nanoporous silicon (black silicon, b-Si) is commonly utilized in photoelectrochemical systems.[23-24, 33-37] b-Si is advantageous relative to planar Si due to its high surface area (~5 times its projected area resulting from its nanostructured surface) that enables high photocurrent densities and promotes gas bubble desorption during electrolysis.[23-24, 34, 38] Recent studies immobilized Pt nanoparticle catalysts onto b-Si photoelectrodes and analyzed the thermodynamics and hydrogen evolution kinetics of the Pt-decorated electrodes. These reports uncovered that deposition of Pt nanoparticle catalysts on a native oxide-terminated b-Si surface (Pt|SiO_x|b-Si) results in a negative shift in V_{FB} compared with a Pt-free electrode (V_{FB} is reported relative to the reversible hydrogen electrode, RHE).[23] Thus, while incorporation of Pt improves kinetics of proton reduction, it simultaneously

decreases the thermodynamic potential of photoelectrochemical charges across the interface. In other words, in this system the Pt catalyst is beneficial for the kinetics of the hydrogen evolution reaction (HER), but at the expense of both the photovoltage usable for water splitting and the semiconductor corrosion resistance (less positive V_{FB} relative to RHE).

It is logical that surface-adsorbed catalysts should reduce the activation energy of charge transfer in both the forward (HER) and reverse (surface oxidation) directions. In order to investigate whether this correlation between improved kinetics and less favorable thermodynamics are inexorably linked, the kinetics and thermodynamics of photoelectrochemical proton reduction by a molecular catalyst attached to b-Si are studied. The HER catalyst [TBA][$Co(bdt)_2$] (where TBA = tetrabutylammonium and bdt = 1,2-benzenedithiolate) is immobilized onto b-Si electrodes using π-π interactions with a variety of covalently attached aromatic molecules (pyrene, naphthalene, styrene, and 4-trifluoromethylstyrene; Scheme 5.3). The surface-bound aromatic species is varied to elucidate the effects of molecular size and electronics on photoelectrochemical proton reduction.

Scheme 5.3. General representation of the modification of b-Si electrodes (top) and pictorial representations of the various modified electrodes (bottom).

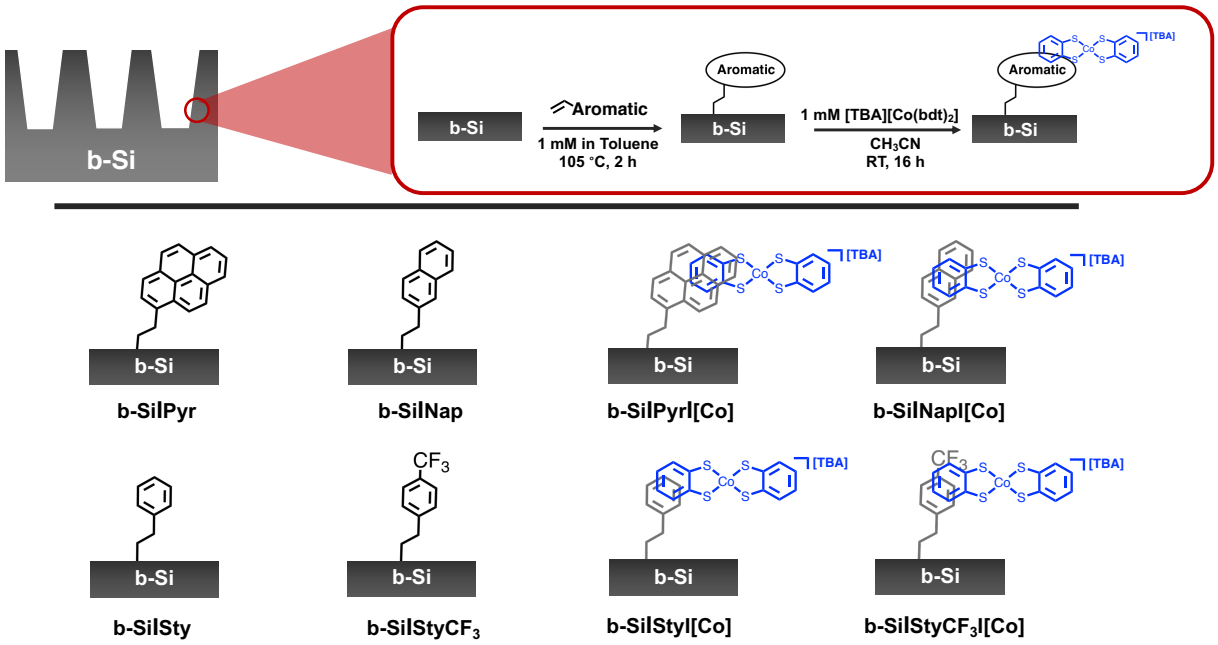

5.2 Results and Discussion

5.2.1 Preparation and Spectroscopic Characterization of Modified b-Si Surfaces

High surface area, H-terminated b-Si electrodes were prepared using a previously published metal-assisted chemical etch procedure.[23-24, 38] Covalent functionalization was achieved via hydrosilylation of H-terminated b-Si with the following vinyl-substituted aromatic molecules: 1-vinylpyrene (Pyr), 2-vinylnapthalene (Nap), styrene (Sty), and 4-trifluoromethylstyrene ($StyCF_3$). Briefly, freshly prepared b-Si wafers were submerged in a 1 mM toluene solution of the vinyl-substituted aromatic molecule of interest and heated to 105 °C for 2 h to yield aromatic-modified b-Si (b-Si|Aromatic). Non-covalently modified b-Si|Aromatic|[Co] were prepared by soaking b-Si|Aromatic electrodes in a 1 mM CH_3CN solution of $[TBA][Co(bdt)_2]$ for 16 h.

It should be noted that the aromatic molecules may polymerize on the surface under these attachment conditions. Unfortunately, the nanostructured nature of b-Si prevents measurement of the film thickness using X-ray photoelectron spectroscopy (XPS) tilt experiments. Analogous XPS tilt measurements on planar silicon electrodes cannot be extrapolated to b-Si silicon due to the non-linear correlation between surface area and surface coverage; a previous report studying ferrocene monolayers on planar and black Si demonstrated a 10-fold increase in ferrocene coverage on black Si relative to planar Si, despite black Si's 5-fold increase in surface area.[24] Quantifying surface coverage of the aromatic molecules is also challenging due to the lack of redox activity or elemental tags that would enable quantification *via* cyclic voltammetry or X-ray photoelectron spectroscopy. However, surface coverage has been shown to depend on molecular size.[39-40] Based on this assumption, we would expect b-Si|Pyr to have the smallest surface coverage, followed b-Si|Nap, b-Si|StyCF_3 and b-Si|Sty.

Covalent attachment of the aromatic molecules to b-Si was verified using infrared spectroscopy. FTIR spectra of the sp^2 C–H stretching frequency range for all b-Si|Aromatic samples are shown in Figure 5.1 and relevant parameters are tabulated in Table 5.1. As listed in Table 5.1, the sp^2 C–H stretching frequencies of b-Si|Pyr, b-Si|Nap, b-Si|Sty, and b-Si|StyCF_3 closely match those of the analogous free molecules, confirming attachment of Pyr, Nap, Sty, and StyCF_3 to the surface.

Table 5.1. sp^2 IR stretches for surface-bound and free aromatics

Sample	$\nu_{C\text{-}H}$ (cm^{-1}) *on b-Si surface*	$\nu_{C\text{-}H}$ (cm^{-1}) *free molecule*
Pyr	3046	3043[a]
Nap	3062	3054[41]
Sty	3065, 3031	3060, 3028[42]
StyCF_3	3047	3095[43]

[a]Figure 5.2

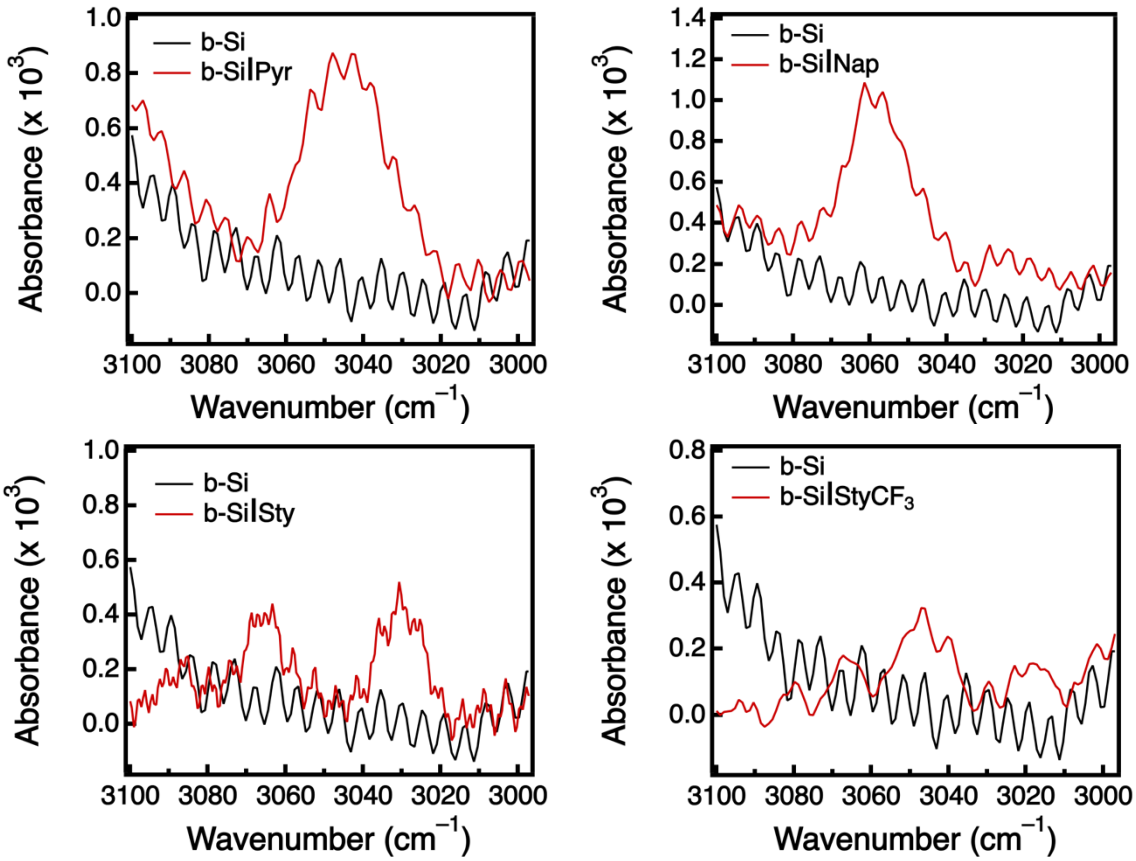

Figure 5.1. Transmission mode FTIR spectra of b-Si|Aromatic samples. Samples were illuminated at 75° off of the surface normal. All spectra were baseline corrected and smoothed using Spectragryph software. The periodic noise is attributed to interference fringes; the non-reflective nature of b-Si only applies to visible and near-IR regions thus infrared reflection remains present here.[33]

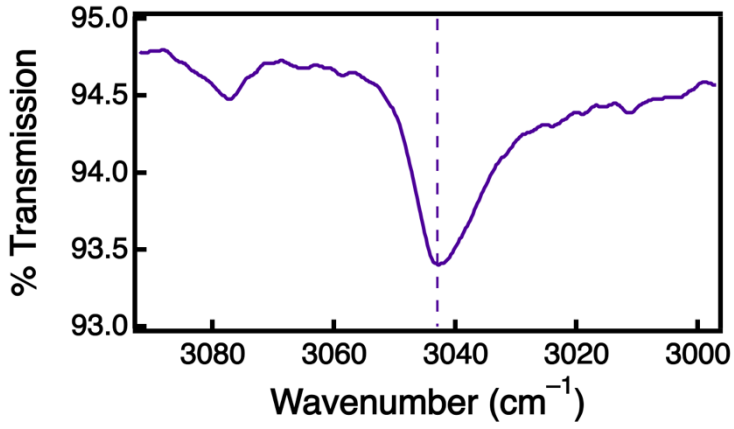

Figure 5.2. IR spectrum of 1-vinylpyrene.

XPS was used to characterize all modified b-Si electrodes. XPS compositional analysis is shown in Table 5.2. Catalyst attachment was confirmed by the presence of a Co 2p peak in the XPS spectra. High-resolution Co 2p XPS spectra for b-Si|Pyr|[Co], b-Si|Nap|[Co], b-Si|Sty|[Co], and b-Si|StyCF_3|[Co] are shown in Figure 5.3. All Co 2p spectra exhibit peaks at 780 and 795 eV which are attributed to Co $2p_{3/2}$ and Co $2p_{1/2}$ photoelectrons, respectively. The S:Co ratio for all samples (Table 5.3) is greater than the expected 4:1 value, which may be due to the presence of excess ligand on the surface. Slight surface oxidation is also found with each surface modification step as evidenced by the growth of the SiO_x peak at 104 eV in the high-resolution Si 2p XPS spectra (Figure 5.4).

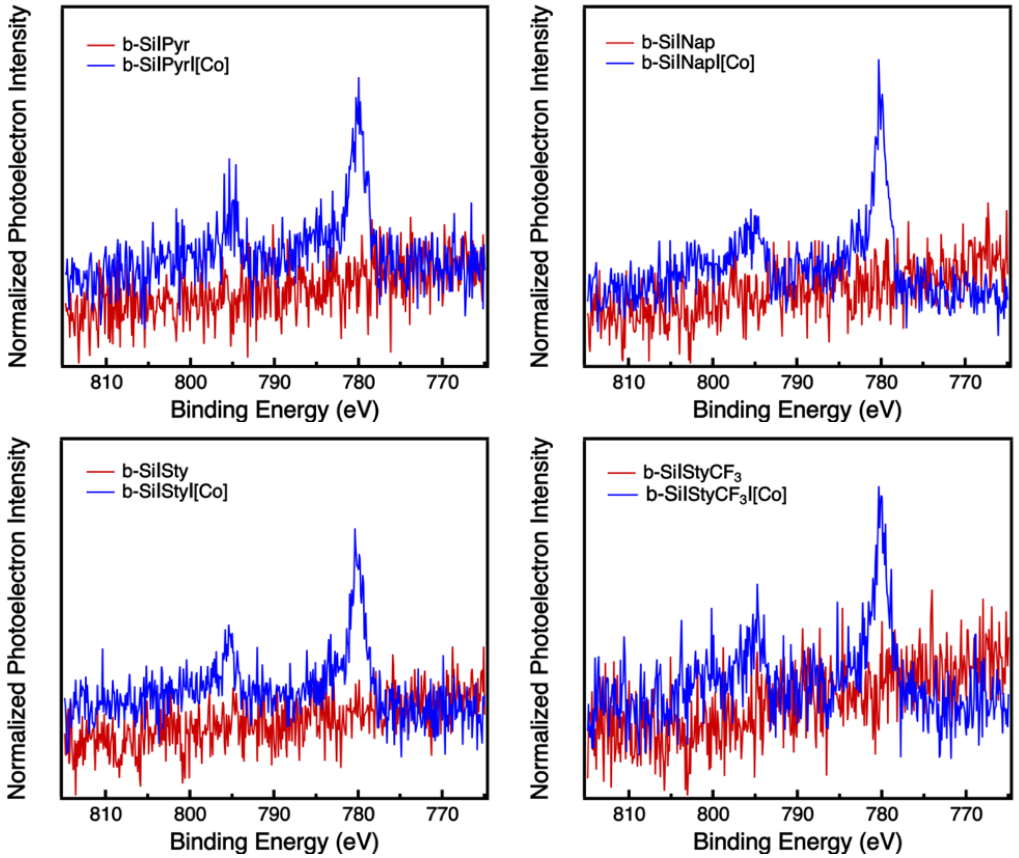

Figure 5.3. High-resolution Co 2p XPS spectra of all b-Si|Aromatic (red traces) and b-Si|Aromatic|[Co] (blue traces) electrodes.

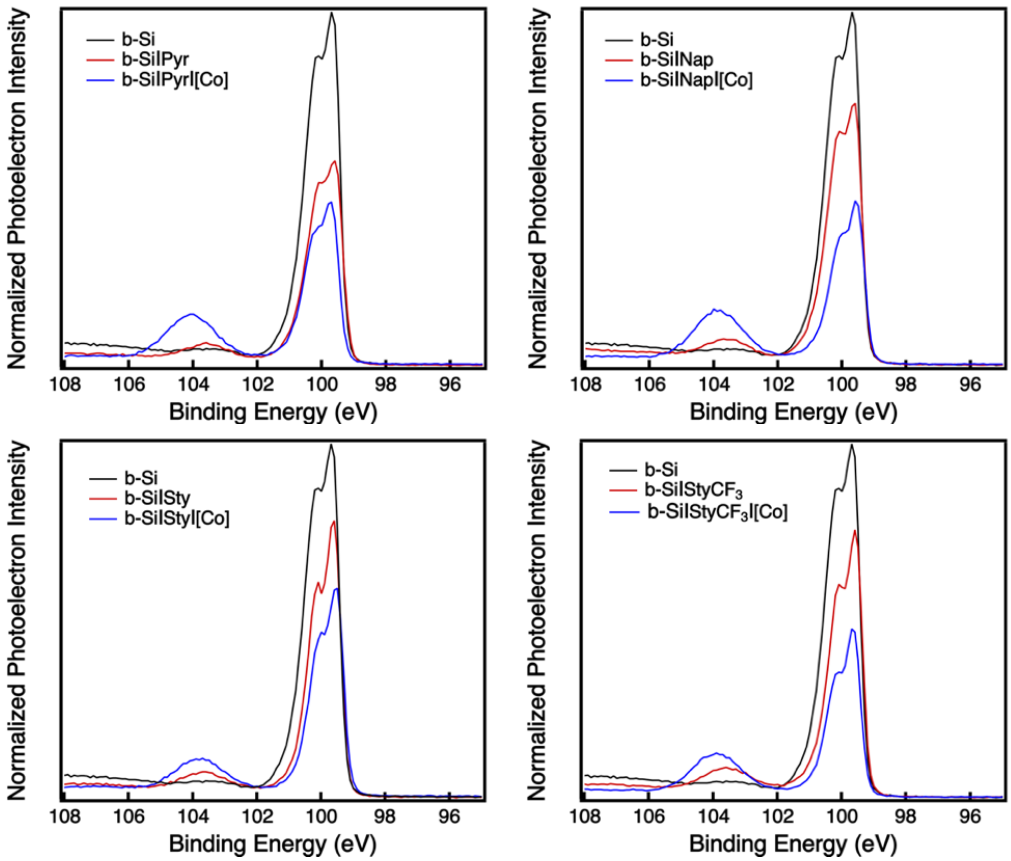

Figure 5.4. High-resolution Si 2p XPS spectra of b-Si (black traces), b-Si|Aromatic (red traces) and b-Si|Aromatic|[Co] (blue traces).

Table 5.2. Compositional analysis of b-Si, b-Si|Aromatic and b-Si|Aromatic|[Co].

Sample	Si	C	O	Co	S	N	F	%Si vs SiO_x
b-Si	70.8	16.7	10.4	0	0.5	0.5	1.0	99.6
b-Si|Pyr	40.7	45.7	13.1	0	0.2	0	0.4	93.8
b-Si|Nap	47.6	37.0	14.8	0	0.1	0	0.5	94.2
b-Si|Sty	47.0	36.7	15.3	0	0.2	0.1	0.8	92.9
b-Si|StyCF_3	41.8	36.3	16.7	0	0.1	0.4	4.5	89.8
b-Si|Pyr|[Co]	30.4	43.4	24.6	0.1	0.4	0.8	0.4	70.3
b-Si|Nap|[Co]	33.7	35.2	28.3	0.1	0.7	1.4	0.5	67.0
b-Si|Sty|[Co]	35.4	42.7	19.3	0.1	0.9	0.9	0.8	81.5
b-Si|StyCF_3|[Co]	33.1	32.7	24.2	0.1	0.7	0.8	3.8	72.1

The work function (ϕ, energy difference between the Fermi level and vacuum) is highly surface-dependent and can be modulated *via* molecular modification of a material's surface.[20-21, 32, 44] The ϕ of all modified b-Si samples was measured using XPS (Figure 5.5); ϕ

values are listed in Table 5.3. The data in Table 5.3 show that covalent attachment of Pyr and Nap result in small positive changes to ϕ (on the edge of the measurement error) relative to H-terminated b-Si, whereas a small negative shift to ϕ is found for Sty. Attachment of $StyCF_3$, on the other hand, increases the ϕ by a much larger value (200 meV) compared with H-terminated b-Si, attributed to the introduction of a strong, positive dipole at the b-Si surface that increases the potential drop across at the b-Si interface. The 260 meV difference in work function between samples with Sty and $StyCF_3$ is consistent with an identical 260 meV ϕ difference previously found between phenylacetylene- and 4-(trifluoromethyl)phenylacetylene-modified Si(100).[44] Attachment of the $[TBA][Co(bdt)_2]$ catalyst via non-covalent π-π interactions yields ϕ values around 3.9 eV for all b-Si|Aromatic|[Co] samples except b-Si|Pyr|[Co], which exhibits a slightly shallower ϕ at 3.73 eV. Once the [Co] catalyst is attached, the measured ϕ likely results from liberation of an electron from a catalyst-derived state, and thus the values all are very similar. A lower surface coverage of Pyr relative to the other aromatics may allow the $[TBA][Co(bdt)_2]$ catalyst to sit closer to the b-Si surface, changing the catalyst energetics slightly relative to that on b-Si|Nap, b-Si|Sty, and b-Si|$StyCF_3$ and resulting in a shallower ϕ.

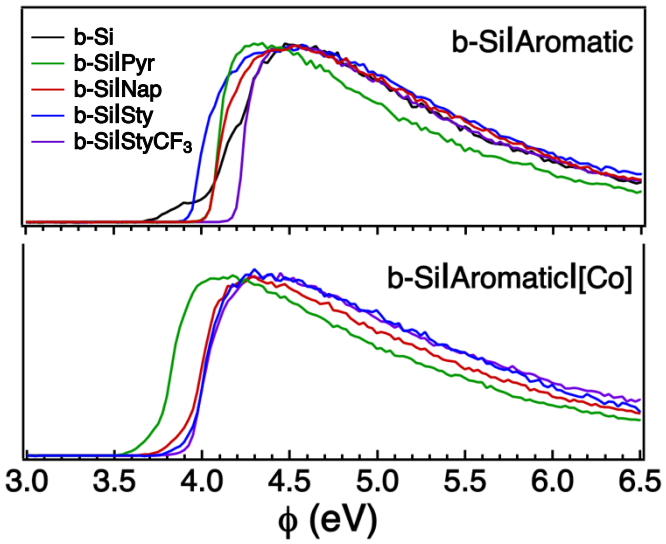

Figure 5.5. The secondary electron cut-off region for XPS measurements of b-Si|Aromatic (top) (red traces) and b-Si|Aromatic|[Co] (bottom).

Table 5.3. Summary of data extracted from XPS and voltammetric measurements.

Sample	S:Co	ϕ (eV)[a]	V_{onset} (vs RHE)	$V_{flatband}$ (vs RHE)
b-Si	-	3.99	−0.31 ± 0.01	0.18 ± 0.01
b-Si|Pyr	-	4.04	−0.38 ± 0.01	0.25 ± 0.01
b-Si|Nap	-	4.03	−0.40 ± 0.02	0.21 ± 0.01
b-Si|Sty	-	3.93	−0.52 ± 0.01	0.26 ± 0.02
b-Si|StyCF$_3$	-	4.19	−0.61 ± 0.02	0.23 ± 0.02
b-Si|Pyr|[Co]	5:1	3.73	−0.21 ± 0.02	0.24 ± 0.01
b-Si|Nap|[Co]	8:1	3.89	−0.19 ± 0.02	0.22 ± 0.01
b-Si|Sty|[Co]	8:1	3.93	−0.27 ± 0.04	0.20 ± 0.01
b-Si|StyCF$_3$|[Co]	7:1	3.92	−0.21 ± 0.02	0.20 ± 0.01

[a]Energy uncertainty is ±0.05 eV

5.2.2 Linear Sweep Voltammetry of Modified Electrodes

Linear sweep voltammograms of b-Si and b-Si|Aromatic samples in 0.1 M H_2SO_4 under 100 mW/cm^2 white-light illumination and in the dark are displayed in Figure 5.6 (black and red traces). Upon covalent modification of b-Si, the onset potential (defined as the potential at which current reaches −1 mA/cm^2) shifts cathodically for all molecular layers (Figure 5.7). Pyr and Nap result in a small (<100 mV) shift in onset potential whereas Sty and $StyCF_3$ shift the onset potential significantly (>200 mV). b-Si|Pyr and b-Si|Nap reach their light-limited photocurrent density (−35 mA/cm^2) within the measured potential range,

whereas b-Si|Sty and b-Si|StyCF_3 are approaching this value at the most negative potential (−1.7 V vs RHE).

Linear sweep voltammograms of b-Si|Aromatic|[Co] samples in 0.1 M H_2SO_4 under 100 mW/cm^2 white-light illumination and in the dark are displayed in the blue traces of Figure 5.6. Attachment of [TBA][Co(bdt)$_2$] results in significant positive shifts in onset potential by 160, 210, 250, and 400 mV for b-Si|Pyr and b-Si|Nap, b-Si|Sty, and b-Si|StyCF_3, respectively, relative to the b-Si|Aromatic sample that additionally confirms the presence of non-covalently bound catalyst. All b-Si|Aromatic|[Co] samples reach light-limited photocurrent density within the potential range measured.

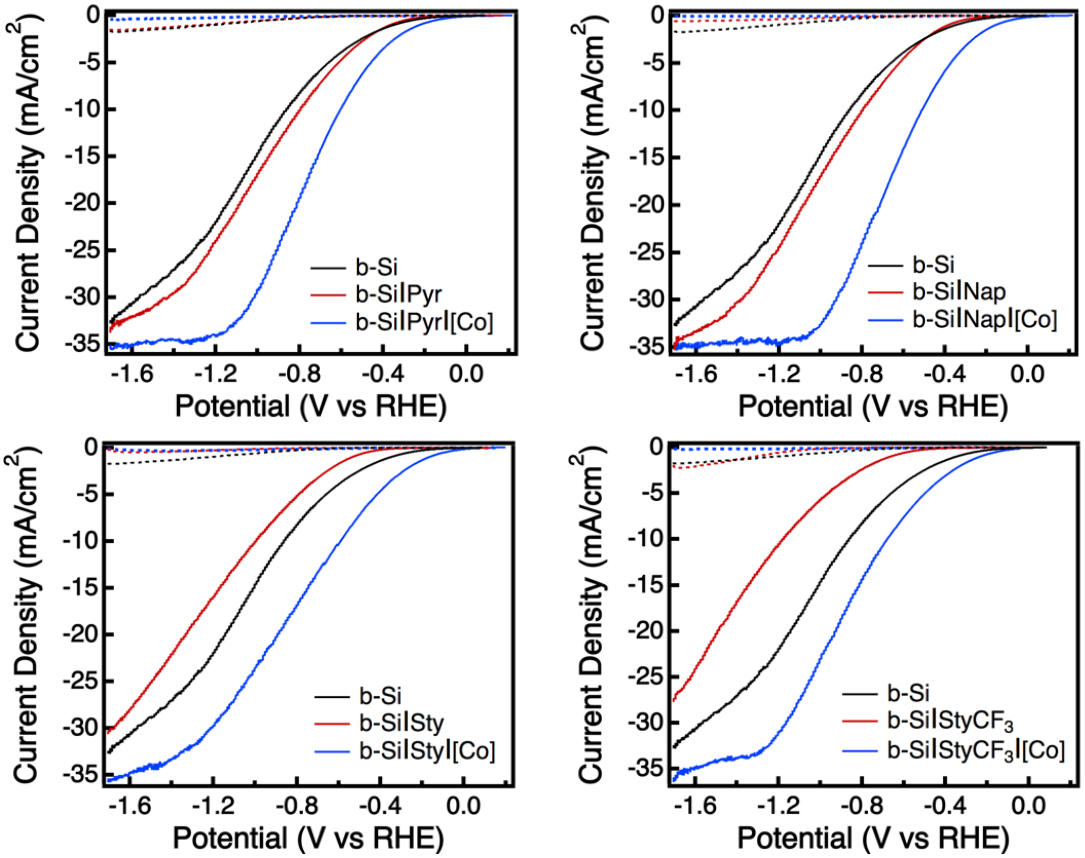

Figure 5.6. Linear sweep voltammograms of b-Si, b-Si|Aromatic, and b-Si|Aromatic|[Co] samples in 0.1 M H_2SO_4 under 100 mW/cm^2 white-light illumination (solid traces) and in the dark (dashed traces).

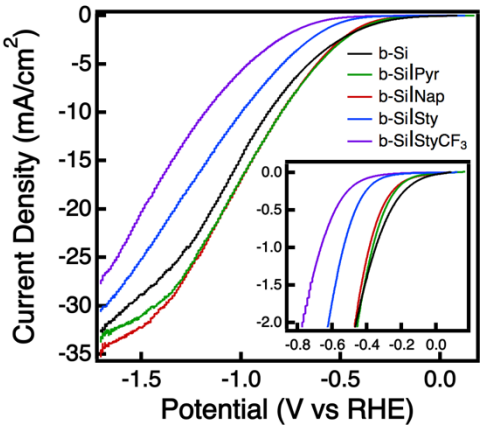

Figure 5.7. Linear sweep voltammograms of b-Si and b-Si|Aromatic samples in 0.1 M H_2SO_4 under 100 mW/cm^2 white-light illumination. The inset shows the region near the onset potential of –1 mA/cm^2.

Figure 5.8 displays the onset potential for proton reduction as a function of molecular layer for b-Si|Aromatic electrodes (red bars) and b-Si|Aromatic|[Co] (blue bars). In the absence of catalyst, proton reduction is likely occurring at the b-Si surface. The molecular layer hinders proton migration toward the electrode surface and therefore shifts the onset potential negative upon b-Si modification. As discussed in section 5.2.1, the surface coverage of the aromatic layers is likely a function of molecular size (i.e. the smaller aromatic molecules should yield higher surface coverage).[39-40] b-Si|Sty and b-Si|StyCF_3 may therefore exhibit more negative onset potentials than b-Si|Pyr and b-Si|Nap because the larger surface coverage results in greater hindrance of proton migration toward the electrode surface. Notably, onset potential is independent of molecular layer identity when the catalyst is present, as depicted in the blue bars in Figure 5.8. This result suggests facile electron transfer between the b-Si and the immobilized catalyst regardless of the molecular layer identity.

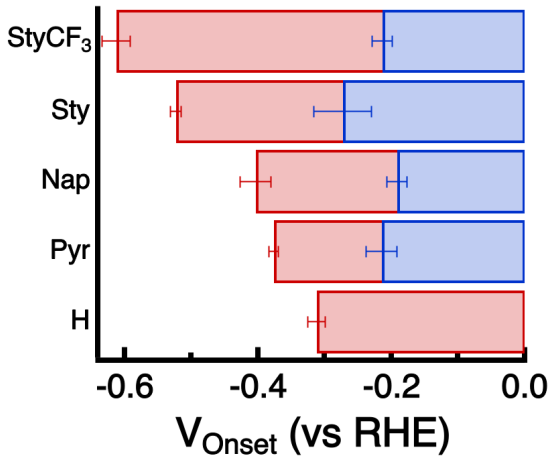

Figure 5.8. Bar chart of onset potential a function of molecular layer identity for b-Si|Aromatic (red bars) and b-Si|Aromatic|[Co] samples (blue bars).

Attaching the catalyst to the surface via π-π interactions suggests that the [Co] catalysts are outside of the Helmholtz layer, which might exhibit different kinetics than within the double-layer.[45-46] Proton reduction by cobalt bis(benzenedithiolate) catalysts in solution is well studied; mechanistic analysis indicates that the complex undergoes two-electron reduction followed by two ligand-based protonation steps.[47-50] Studies on proton-coupled electron transfer (PCET) at indium tin oxide electrodes modified with a pyrene-appended anthraquinone derivative through π-π interactions showed that the surface-bound molecules undergo PCET processes consistent with their water-soluble, homogeneous analogs.[51] The surface-bound [TBA][Co(bdt)$_2$] catalyst is therefore expected to reduce protons by a similar mechanism to cobalt bis(benzenedithiolate) catalysts studied in solution. To gain further understanding of the activity of the catalyst on the electrode surface, current densities from the linear sweep voltammograms of b-Si|Aromatic were subtracted from those of b-Si|Aromatic|[Co] (ΔI) and plotted vs potential in Figure 5.9. All ΔI traces exhibit a reduction peak between –0.97 and –1.23 V vs RHE with current densities between –12 and –20 mA/cm^2. The variations in peak potential and current density across

electrodes may be due to changes in catalyst coverage and electron transfer kinetics. Despite these variations, the peak potentials are close to those reported for proton reduction in water by [TBA][Co(bdt)$_2$] immobilized onto HOPG electrodes (≈0.9 V vs RHE), suggesting retention of the molecular nature of the catalyst under voltammetric conditions.[52]

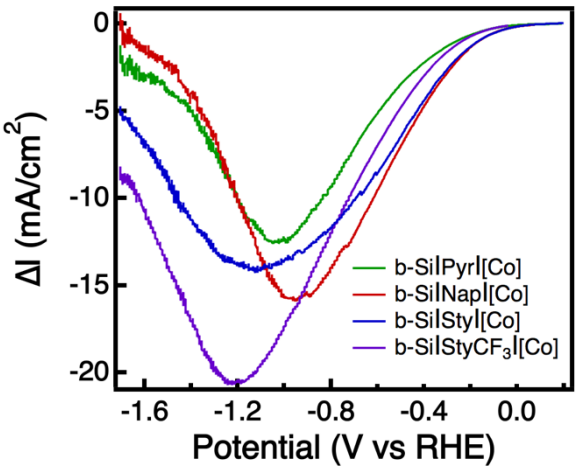

Figure 5.9. ΔI vs potential for all b-Si|Aromatic|[Co] electrodes. ΔI is obtained by subtracting the current densities from the linear sweep voltammograms of b-Si|Aromatic from those of b-Si|Aromatic|[Co].

5.2.3 IMHFR Impedance Spectroscopy of Modified Electrodes

IMHFR impedance spectroscopy was employed to understand the thermodynamic effects of b-Si surface modification on photoelectrochemical proton reduction. IMHFR impedance spectroscopy plots for b-Si and b-Si|Aromatic samples are displayed in Figure 5.10 (left) and V_{FB} is plotted as a function of molecular layer identity in Figure 5.11. Interestingly, V_{FB} only varies by <100 mV upon covalent modification of b-Si, regardless of the molecular layer identity. This narrow range in V_{FB} suggests that the stronger changes to work function ($\Delta\phi$ = 260 meV, Table 5.3) observed under vacuum do not translate to solution. As has been observed previously, siginficant charge screening by ions in the Helmholtz layer is expected to mitigate the dipolar effects on the space-charge region of the

semiconductor. [20, 27-28] This result indicates that these surface chemistry modifications have a minimal impact on the thermodynamics for photoelectrochemical proton reduction across all b-Si samples, highlighting the importance of the aforementioned kinetic factors on the changes in onset potential for proton reduction at b-Si|Aromatic electrodes.

IMHFR impedance spectroscopy plots for b-Si|Aromatic|[Co] samples are displayed in Figure 5.10 (right) and Figure 5.11 displays V_{FB} as a function of molecular layer identify (blue bars). As seen for covalent modification of b-Si, V_{FB} varies by <100 mV upon catalyst attachment. This result indicates that our π-π attachment scheme enhances the proton reduction onset potential without modulating V_{FB}, decoupling the kinetics of proton reduction from the thermodynamics of the supporting b-Si electrode.

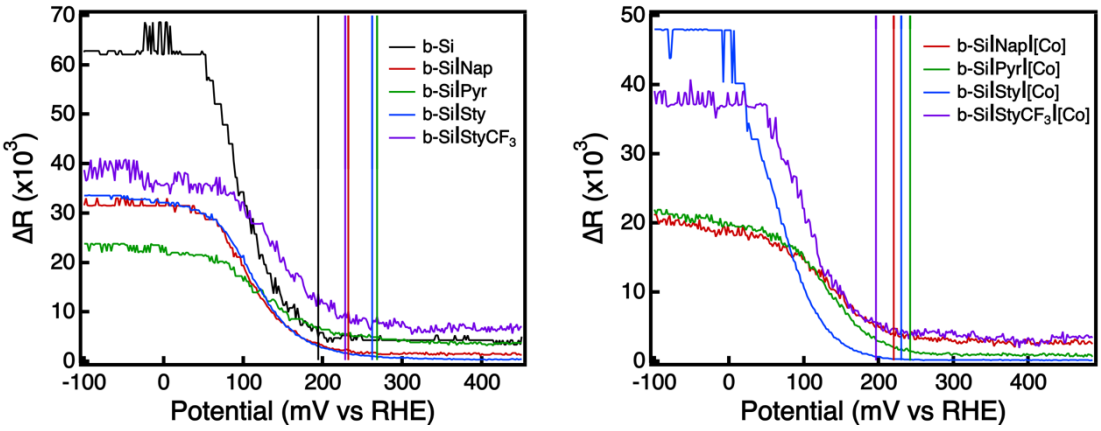

Figure 5.10. IMHFR plots for b-Si|Aromatic and b-Si|Aromatic|[Co]. The vertical lines represent the flatband potential which is taken as the potential where the ΔR value deviated significantly (> 4 standard deviations) from the average value of the flat region of the curve for two consecutive points.

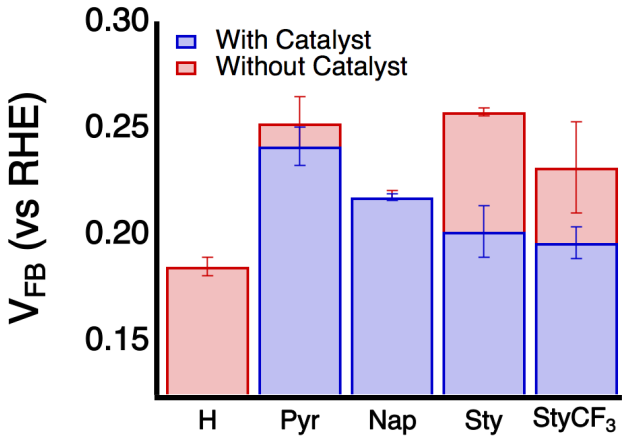

Figure 5.11. Bar chart of V_{FB} as a function of molecular layer identity for b-Si|Aromatic (red bars) and b-Si|Aromatic|[Co] (blue bars).

5.2.4 Photoelectrochemical Stability of Modified Electrodes

Chronoamerperometry of b-Si|Aromatic and b-Si|Aromatic|[Co] electrodes at –0.4 V vs RHE under 1 sun illumination was performed in order to probe the stability of the modified silicon electrodes under sustained photoelectrolysis. Figure 5.12 (left) displays the current vs time plots for b-Si and b-Si|Aromatic electrodes at –0.4 V vs RHE. Over 25 minutes, the current of b-Si slowly increases, likely due to some deleterious side reaction that changes the nature of the b-Si photocathode.[53] b-Si|Aromatic electrodes, however, maintain constant current throughout the 25 minutes of electrolysis. These results suggest improved stability upon covalent attachment of the aromatic molecule to b-Si, similar to reported systems in which methyl[31, 54] or graphene[55] monolayers improve photoelectrode stability under extended aqueous photoelectrolysis. Current vs time plots for b-Si|Aromatic|[Co] electrodes at –0.4 V vs RHE are shown in Figure 5.12 (right). All b-Si|Aromatic|[Co] electrodes exhibit a gradual decrease in current throughout photoelectrolysis, suggesting loss of the [Co] catalyst during photoelectrocatalysis. These results indicate that while the aromatic layer improves

the stability of the b-Si electrode, the b-Si|Aromatic|[Co] electrodes are unstable under sustained photoelectrolysis due to loss of the catalyst.

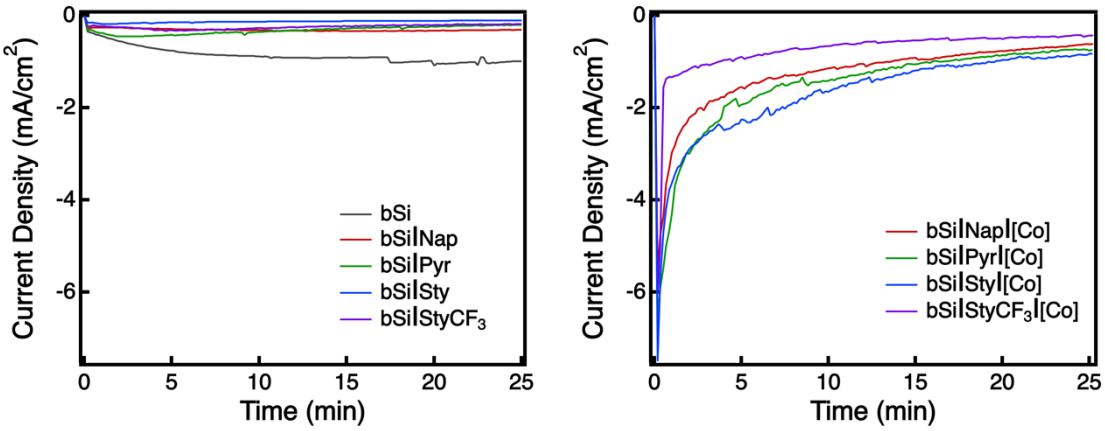

Figure 5.12. Current vs time plots for photoelectrolysis of b-Si|Aromatic (left) and b-Si|Aromatic|[Co] (right) at –0.4 V vs RHE in 0.1 M H_2SO_4 under 1 sun illumination.

5.3 Conclusions

A molecular cobalt bis(benzenedithiolate) proton reduction catalyst was attached to nanoporous b-Si photoelectrodes through π-π interactions with a series of covalently attached aromatic molecules. Infrared and X-ray photoelectron spectroscopy confirm attachment of the covalently bound aromatic molecules and the physisorbed catalyst. Measurement of the work function indicates changes induced by the surface dipole on the b-Si surface, but IMHFR impedance spectroscopy shows that V_{FB} under photoelectrochemical conditions remains unchanged, likely due to Helmholtz layer dipole screening. A correlation was established between the size of the aromatic surface-linker and the corresponding electrode's onset potential for proton reduction. In contrast, identical experiments conducted upon subsequent catalyst attachment demonstrate similar thermodynamics (V_{FB}) and proton reduction activity (onset potential) for all samples, with no dependence on the identity of the aromatic species covalently attached to the b-Si surface. Attachment of

[TBA][Co(bdt)$_2$] via π-π interactions therefore improves the kinetics of catalysis without adversely affecting the thermodynamics of photoelectrochemical charge-transfer across the interface. These results demonstrate the ability of this π-π attachment scheme to decouple kinetics of interfacial catalytic reactions from the thermodynamics of the underlying semiconductor electrode, providing a route for rational design of efficient photoelectrochemical interfaces for fuel-forming reactions.

5.4 Experimental Details

General Procedures

Isopropanol (electronic grade, Fisher) and acetone (ACS grade, VWR) were used without further purification. Toluene (ACS grade, Acros) and CH_3CN (HPLC grade, Fisher) were purified by stirring over CaH_2 overnight and distilling under N_2. Silicon wafers (boron-doped Si(100), 1–5 Ω cm, 255–305 μm thick) were purchased from Topsil. Styrene and 4-trifluoromethylstyrene were dried by stirring over CaH_2 in an inert atmosphere for 3 hours and subsequently purified via vacuum transfer. 1-Vinylpyrene[56] and [TBA][Co(bdt)$_2$][57] were prepared using previously published procedures and dried under vacuum using P_2O_5 as a desiccant. All other reagents were purchased from commercial suppliers and used without further purification.

Sample Preparation

Silicon wafers were cut into 1 cm x 10 cm strips with a diamond scribe. The strips were sonicated in acetone and isopropanol for 10 minutes each, drying under a stream of compressed air after each solvent. Kapton tape was applied to the backside of the strips. The strips were sonicated in deionized water for 10 minutes and blown dry. Strips were then

etched by immersing in an aqueous 2 M HF solution for 60 seconds, rinsed with deionized water, and dried under a stream of N_2.

Black silicon wafers were prepared using a previously published metal-assisted chemical etch procedure.[23-24, 38] Clean and etched silicon strips were soaked in 1 mM $AgNO_3$/0.4 M HF for 30 seconds to deposit Ag nanoparticles on the surface. The strips were then immersed in a freshly prepared MACE solution (1.25 M HF/0.16 M H_2O_2) for 6 minutes while tapping on the bench top approximately once per second with the etched side of the strip facing up to release bubbles from the surface. Next, the strips were soaked in 35 % HNO_3 for 6 minutes, 55 M $(CH_3)_4NOH$ for 2 seconds, and finally 2 M HF for 30 seconds. The strips were rinsed with deionized water and dried under a stream of N_2 between each step and brought into an Ar filled glovebox immediately after preparation.

Black silicon strips for surface functionalization were cut into approximately 1 cm x 1 cm wafers with a diamond scribe inside an Ar filled glovebox. Covalent functionalization with the various aromatic molecules was achieved by placing freshly etched planar silicon or freshly prepared black silicon wafers at the bottom of a scintillation vial with 1 mL of a 1 mM solution in toluene. The vials were then sealed and placed on a preheated hotplate at 105 ˚C for 2 h. The solution was removed from the vials and the wafers sonicated in toluene for 10 minutes. Pyrene-modified wafers were then dried and stored in an Ar-filled glovebox until further use. Catalyst attachment was achieved by soaking pyrene-modified wafers in 1 mM CH_3CN solutions of $[TBA][Co(bdt)_2]$ for 16 h.

Electrodes for electrochemical analysis were prepared according to the following procedure: copper tape was applied to a glass microscope slide and a drop of Ag paint was applied to the copper tape. The backside of a b-Si sample was scratched and coated with

Ga/In eutectic. The sample was pressed onto the copper tape over the drop of Ag paint. Kapton tape was used to cover exposed copper tape and epoxy (Loctite EA 615) was used to seal the electrode. Samples were cured at room temperature for 2 h before analysis.

Physical Methods

FTIR spectra were recorded using a Nicolett 6700 spectrometer. Spectra were recorded in transmission mode and samples were illuminated at 75° off of the surface normal. All spectra were baseline corrected and smoothed using Spectragryph software.

X-Ray Photoelectron Spectroscopy measurements were obtained on a Physical Electronics 5600 system using Al Kα radiation. The raw atomic concentration has a 5% error due to surface inhomogeneities, surface roughness, literature sensitivity values for peak integration, etc. For the work function measurements, the XPS setup was calibrated with Au metal, which was cleaned via Ar-ion sputtering. The work function measurements have an uncertainty of ± 50 meV.

Photoelectrochemical experiments were performed using a Biologic SP-300 potentiostat and EC-Lab software. Experiments were performed in 0.1 M H_2SO_4 (pH = 1.5) under 1 sun illumination (ABET Technologies Sun 3000 Solar Simulator) with a Ag/AgCl reference electrode and an iridium oxide counter electrode at a scan rate of 100 mV/s. The onset potential was recorded as the potential at which current reached –1 mA/cm^2. Potentials were converted to RHE using the following equation: $E_{RHE} = E_{Ag/AgCl} + 0.197 + 0.059*pH$. [58]

The flatband potential was determined by measuring the difference in the dark and illuminated sample resistivity (R) via intensity-modulated high frequency resistivity (IMHFR) spectroscopy. As previously described,[23-24] a lock-in amplifier (SR 830) introduced

an AC frequency (100 kHz, 10 mV amplitude) to a potential applied by a potentiostat (PAR 283). A Labview program was used to set the potential and read the R values from the lock-in amplifier. The sample was subjected to light/dark cycles using a Uniblitz chopper set to 5 Hz and a broadband light source (41720-series Cole Parmer, 150 W tungsten halogen lamp). The LabView program bins light and dark R values, then calculates the difference between them (ΔR). The measurement was made using the same electrochemical cell described above for acidic J–V data collection (unless otherwise stated). The potential was stepped at 2 mV intervals throughout the potential range. The flatband potential was taken as the potential where the ΔR value deviated significantly (> 4 standard deviations) from the average value of the flat region of the curve for two consecutive points.

5.5 References

1. Gratzel, M., Photoelectrochemical cells. *Nature* **2001,** *414*, 338-344.

2. Walter, M. G.; Warren, E. L.; McKone, J. R.; Boettcher, S. W.; Mi, Q.; Santori, E. A.; Lewis, N. S., Solar Water Splitting Cells. *Chem. Rev.* **2010,** *110*, 6446-6473.

3. Blakemore, J. D.; Crabtree, R. H.; Brudvig, G. W., Molecular Catalysts for Water Oxidation. *Chem. Rev.* **2015,** *115*, 12974-13005.

4. Rakowski DuBois, M.; DuBois, D. L., The roles of the first and second coordination spheres in the design of molecular catalysts for H2 production and oxidation. *Chem. Soc. Rev.* **2009,** *38*, 62-72.

5. Thammavongsy, Z.; Mercer, I. P.; Yang, J. Y., Promoting proton coupled electron transfer in redox catalysts through molecular design. *Chem. Comm.* **2019,** *55*, 10342-10358.

6. Barlow, J. M.; Yang, J. Y., Thermodynamic Considerations for Optimizing Selective CO2 Reduction by Molecular Catalysts. *ACS Cent. Sci.* **2019,** *5*, 580-588.

7. Seo, J.; Pekarek, R. T.; Rose, M. J., Photoelectrochemical operation of a surface-bound, nickel-phosphine H2 evolution catalyst on p-Si(111): a molecular semiconductor|catalyst construct. *Chem. Comm.* **2015,** *51*, 13264-13267.

8. Lattimer, J. R. C.; Blakemore, J. D.; Sattler, W.; Gul, S.; Chatterjee, R.; Yachandra, V. K.; Yano, J.; Brunschwig, B. S.; Lewis, N. S.; Gray, H. B., Assembly, characterization, and electrochemical properties of immobilized metal bipyridyl complexes on silicon(111) surfaces. *Dalton Trans.* **2014,** *43*, 15004-15012.

9. Leung, J. J.; Warnan, J.; Nam, D. H.; Zhang, J. Z.; Willkomm, J.; Reisner, E., Photoelectrocatalytic H2 evolution in water with molecular catalysts immobilised on p-Si via a stabilising mesoporous TiO2 interlayer. *Chem. Sci.* **2017,** *8*, 5172-5180.

10. Gu, J.; Yan, Y.; Young, J. L.; Steirer, K. X.; Neale, N. R.; Turner, J. A., Water reduction by a p-GaInP2 photoelectrode stabilized by an amorphous TiO2 coating and a molecular cobalt catalyst. *Nat. Mater.* **2015,** *15*, 456-460.

11. Gulati, S.; Hietsoi, O.; Calvary, C. A.; Strain, J. M.; Pishgar, S.; Brun, H. C.; Grapperhaus, C. A.; Buchanan, R. M.; Spurgeon, J. M., Photocatalytic hydrogen evolution on Si photocathodes modified with bis(thiosemicarbazonato)nickel(ii)/Nafion. *Chem. Comm.* **2019,** *55*, 9440-9443.

12. Cedeno, D.; Krawicz, A.; Doak, P.; Yu, M.; Neaton, J. B.; Moore, G. F., Using Molecular Design to Control the Performance of Hydrogen-Producing Polymer-Brush-Modified Photocathodes. *J. Phys. Chem. Lett.* **2014,** *5*, 3222-3226.

13. Beiler, A. M.; Khusnutdinova, D.; Jacob, S. I.; Moore, G. F., Solar Hydrogen Production Using Molecular Catalysts Immobilized on Gallium Phosphide (111)A and (111)B Polymer-Modified Photocathodes. *ACS Appl. Mater. Interfaces* **2016,** *8*, 10038-10047.

14. Khusnutdinova, D.; Beiler, A. M.; Wadsworth, B. L.; Jacob, S. I.; Moore, G. F., Metalloporphyrin-modified semiconductors for solar fuel production. *Chem. Sci.* **2017,** *8*, 253-259.

15. Beiler, A. M.; Khusnutdinova, D.; Wadsworth, B. L.; Moore, G. F., Cobalt Porphyrin–Polypyridyl Surface Coatings for Photoelectrosynthetic Hydrogen Production. *Inorg. Chem.* **2017,** *56*, 12178-12185.

16. Beiler, A. M.; Khusnutdinova, D.; Jacob, S. I.; Moore, G. F., Chemistry at the Interface: Polymer-Functionalized GaP Semiconductors for Solar Hydrogen Production. *Ind. Eng. Chem. Res.* **2016,** *55*, 5306-5314.

17. Downes, C. A.; Marinescu, S. C., Efficient Electrochemical and Photoelectrochemical H2 Production from Water by a Cobalt Dithiolene One-Dimensional Metal–Organic Surface. *J. Am. Chem. Soc.* **2015,** *137*, 13740-13743.

18. Nozik, A. J.; Memming, R., Physical Chemistry of Semiconductor−Liquid Interfaces. *J. Phys. Chem.* **1996,** *100*, 13061-13078.

19. Lewis, N. S., Photoeffects at the Semiconductor/Liquid Interface. *Annu. Rev. Mater. Sci.* **1984,** *14*, 95-117.

20. Li, Y.; O'Leary, L. E.; Lewis, N. S.; Galli, G., Combined Theoretical and Experimental Study of Band-Edge Control of Si through Surface Functionalization. *J. Phys. Chem. C* **2013,** *117*, 5188-5194.

21. Gleason-Rohrer, D. C.; Brunschwig, B. S.; Lewis, N. S., Measurement of the Band Bending and Surface Dipole at Chemically Functionalized Si(111)/Vacuum Interfaces. *J. Phys. Chem. C* **2013,** *117*, 18031-18042.

22. Seo, J.; Kim, H. J.; Pekarek, R. T.; Rose, M. J., Hybrid Organic/Inorganic Band-Edge Modulation of p-Si(111) Photoelectrodes: Effects of R, Metal Oxide, and Pt on H2 Generation. *J. Am. Chem. Soc.* **2015,** *137*, 3173-3176.

23. Anderson, N. C.; Carroll, G. M.; Pekarek, R. T.; Christensen, S. T.; van de Lagemaat, J.; Neale, N. R., Silicon Photoelectrode Thermodynamics and Hydrogen Evolution Kinetics Measured by Intensity-Modulated High-Frequency Resistivity Impedance Spectroscopy. *J. Phys. Chem. Lett.* **2017,** *8*, 5253-5258.

24. Pekarek, R. T.; Christensen, S. T.; Liu, J.; Neale, N. R., Energetic effects of hybrid organic/inorganic interfacial architecture on nanoporous black silicon photoelectrodes. *Sustain. Energy Fuels* **2019,** *3*, 1660-1667.

25. Johansson, E.; Boettcher, S. W.; O'Leary, L. E.; Poletayev, A. D.; Maldonado, S.; Brunschwig, B. S.; Lewis, N. S., Control of the pH-Dependence of the Band Edges of Si(111) Surfaces Using Mixed Methyl/Allyl Monolayers. *J. Phys. Chem. C* **2011,** *115*, 8594-8601.

26. Grimm, R. L.; Bierman, M. J.; O'Leary, L. E.; Strandwitz, N. C.; Brunschwig, B. S.; Lewis, N. S., Comparison of the Photoelectrochemical Behavior of H-Terminated and Methyl-Terminated Si(111) Surfaces in Contact with a Series of One-Electron, Outer-Sphere Redox Couples in CH3CN. *J. Phys. Chem. C* **2012,** *116*, 23569-23576.

27. MacLeod, B. A.; Steirer, K. X.; Young, J. L.; Koldemir, U.; Sellinger, A.; Turner, J. A.; Deutsch, T. G.; Olson, D. C., Phosphonic Acid Modification of GaInP2 Photocathodes Toward Unbiased Photoelectrochemical Water Splitting. *ACS Appl. Mater. Interfaces* **2015,** *7*, 11346-11350.

28. Garner, L. E.; Steirer, K. X.; Young, J. L.; Anderson, N. C.; Miller, E. M.; Tinkham, J. S.; Deutsch, T. G.; Sellinger, A.; Turner, J. A.; Neale, N. R., Covalent Surface Modification of Gallium

Arsenide Photocathodes for Water Splitting in Highly Acidic Electrolyte. *ChemSusChem* **2017,** *10*, 767-773.

29. Peczonczyk, S. L.; Mukherjee, J.; Carim, A. I.; Maldonado, S., Wet Chemical Functionalization of III–V Semiconductor Surfaces: Alkylation of Gallium Arsenide and Gallium Nitride by a Grignard Reaction Sequence. *Langmuir* **2012,** *28*, 4672-4682.

30. Peczonczyk, S. L.; Brown, E. S.; Maldonado, S., Secondary Functionalization of Allyl-Terminated GaP(111)A Surfaces via Heck Cross-Coupling Metathesis, Hydrosilylation, and Electrophilic Addition of Bromine. *Langmuir* **2014,** *30*, 156-164.

31. Brown, E. S.; Peczonczyk, S. L.; Wang, Z.; Maldonado, S., Photoelectrochemical Properties of CH3-Terminated p-Type GaP(111)A. *J. Phys. Chem. C* **2014,** *118*, 11593-11600.

32. Arefi, H. H.; Fagas, G., Chemical Trends in the Work Function of Modified Si(111) Surfaces: A DFT Study. *J. Phys. Chem. C* **2014,** *118*, 14346-14354.

33. Oh, J.; Deutsch, T. G.; Yuan, H.-C.; Branz, H. M., Nanoporous black silicon photocathode for H2 production by photoelectrochemical water splitting. *Energy Environ. Sci.* **2011,** *4*, 1690-1694.

34. Aguiar, J. A.; Anderson, N. C.; Neale, N. R., Revealing the semiconductor–catalyst interface in buried platinum black silicon photocathodes. *J. Mater. Chem. A* **2016,** *4*, 8123-8129.

35. Oh, I.; Kye, J.; Hwang, S., Enhanced Photoelectrochemical Hydrogen Production from Silicon Nanowire Array Photocathode. *Nano Lett.* **2012,** *12*, 298-302.

36. Yuan, G.; Aruda, K.; Zhou, S.; Levine, A.; Xie, J.; Wang, D., Understanding the Origin of the Low Performance of Chemically Grown Silicon Nanowires for Solar Energy Conversion. *Angew. Chem. Int. Ed.* **2011,** *50*, 2334-2338.

37. Foley, J. M.; Price, M. J.; Feldblyum, J. I.; Maldonado, S., Analysis of the operation of thin nanowire photoelectrodes for solar energy conversion. *Energy Environ. Sci.* **2012,** *5*, 5203-5220.

38. Zhao, Y.; Anderson, N. C.; Zhu, K.; Aguiar, J. A.; Seabold, J. A.; Lagemaat, J. v. d.; Branz, H. M.; Neale, N. R.; Oh, J., Oxidatively Stable Nanoporous Silicon Photocathodes with Enhanced Onset Voltage for Photoelectrochemical Proton Reduction. *Nano Lett.* **2015,** *15*, 2517-2525.

39. Pekarek, R. T.; Celio, H.; Rose, M. J., Synthetic Insights into Surface Functionalization of Si(111)–R Photoelectrodes: Steric Control and Deprotection of Molecular Passivating Layers. *Langmuir* **2018,** *34*, 6328-6337.

40. Nemanick, E. J.; Hurley, P. T.; Brunschwig, B. S.; Lewis, N. S., Chemical and Electrical Passivation of Silicon (111) Surfaces through Functionalization with Sterically Hindered Alkyl Groups. *J. Phys. Chem. B* **2006,** *110*, 14800-14808.

41. Gordillo, A.; Ortuño, M. A.; López-Mardomingo, C.; Lledós, A.; Ujaque, G.; de Jesús, E., Mechanistic Studies on the Pd-Catalyzed Vinylation of Aryl Halides with Vinylalkoxysilanes in Water: The Effect of the Solvent and NaOH Promoter. *J. Am. Chem. Soc.* **2013,** *135*, 13749-13763.

42. Schwartz, M. P.; Ellison, M. D.; Coulter, S. K.; Hovis, J. S.; Hamers, R. J., Interaction of π-Conjugated Organic Molecules with π-Bonded Semiconductor Surfaces: Structure, Selectivity, and Mechanistic Implications. *J. Am. Chem. Soc.* **2000,** *122*, 8529-8538.

43. Wilkerson-Hill, S. M.; Sawano, S.; Sarpong, R., Bis(1-cyanovinyl acetate) Is a Linear Precursor to 3-Oxidopyrylium Ions. *J. Org. Chem.* **2016,** *81*, 11132-11144.

44. Cooper, A. J.; Keyvanfar, K.; Deberardinis, A.; Pu, L.; Bean, J. C., Dopant passivation and work function tuning through attachment of heterogeneous organic monolayers on silicon in ultrahigh vacuum. *Appl. Surf. Sci.* **2011,** *257*, 6138-6144.

45. Jackson, M. N.; Oh, S.; Kaminsky, C. J.; Chu, S. B.; Zhang, G.; Miller, J. T.; Surendranath, Y., Strong Electronic Coupling of Molecular Sites to Graphitic Electrodes via Pyrazine Conjugation. *J. Am. Chem. Soc.* **2018,** *140*, 1004-1010.

46. Jackson, M. N.; Pegis, M. L.; Surendranath, Y., Graphite-Conjugated Acids Reveal a Molecular Framework for Proton-Coupled Electron Transfer at Electrode Surfaces. *ACS Cent. Sci.* **2019,** *5*, 831-841.

47. McNamara, W. R.; Han, Z.; Alperin, P. J.; Brennessel, W. W.; Holland, P. L.; Eisenberg, R., A Cobalt–Dithiolene Complex for the Photocatalytic and Electrocatalytic Reduction of Protons. *J. Am. Chem. Soc.* **2011,** *133*, 15368-15371.

48. McNamara, W. R.; Han, Z.; Yin, C.-J.; Brennessel, W. W.; Holland, P. L.; Eisenberg, R., Cobalt-dithiolene complexes for the photocatalytic and electrocatalytic reduction of protons in aqueous solutions. *Proc. Natl. Acad. Sci.* **2012,** *109*, 15594-15599.

49. Lee, K. J.; McCarthy, B. D.; Rountree, E. S.; Dempsey, J. L., Identification of an Electrode-Adsorbed Intermediate in the Catalytic Hydrogen Evolution Mechanism of a Cobalt Dithiolene Complex. *Inorg. Chem.* **2017,** *56*, 1988-1998.

50. Solis, B. H.; Hammes-Schiffer, S., Computational Study of Anomalous Reduction Potentials for Hydrogen Evolution Catalyzed by Cobalt Dithiolene Complexes. *J. Am. Chem. Soc.* **2012,** *134*, 15253-15256.

51. Hanna, C. M.; Luu, A.; Yang, J. Y., Proton-Coupled Electron Transfer at Anthraquinone Modified Indium Tin Oxide Electrodes. *ACS Appl. Energy Mater.* **2019,** *2*, 59-65.

52. Eady, S. C.; MacInnes, M. M.; Lehnert, N., Immobilized Cobalt Bis(benzenedithiolate) Complexes: Exceptionally Active Heterogeneous Electrocatalysts for Dihydrogen Production from Mildly Acidic Aqueous Solutions. *Inorg. Chem.* **2017,** *56*, 11654-11667.

53. Sun, K.; Shen, S.; Liang, Y.; Burrows, P. E.; Mao, S. S.; Wang, D., Enabling Silicon for Solar-Fuel Production. *Chem. Rev.* **2014,** *114*, 8662-8719.

54. Hamann, T. W.; Lewis, N. S., Control of the Stability, Electron-Transfer Kinetics, and pH-Dependent Energetics of Si/H2O Interfaces through Methyl Termination of Si(111) Surfaces. *J. Phys. Chem. B* **2006,** *110*, 22291-22294.

55. Nielander, A. C.; Bierman, M. J.; Petrone, N.; Strandwitz, N. C.; Ardo, S.; Yang, F.; Hone, J.; Lewis, N. S., Photoelectrochemical Behavior of n-Type Si(111) Electrodes Coated With a Single Layer of Graphene. *J. Am. Chem. Soc.* **2013,** *135*, 17246-17249.

56. Albagli, D.; Bazan, G. C.; Schrock, R. R.; Wrighton, M. S., New functional polymers prepared by ring-opening metathesis polymerization: study of the quenching of luminescence of pyrene end groups by ferrocene or phenothiazine centers in the polymers. *J. Phys. Chem.* **1993,** *97*, 10211-10216.

57. Baker-Hawkes, M. J.; Billig, E.; Gray, H. B., Characterization and Electronic Structures of Metal Complexes Containing Benzene-1,2-dithiolate and Related Ligands. *J. Am. Chem. Soc.* **1966,** *88*, 4870-4875.

58. Faulkner, A. J. B. a. L. R., *Electrochemical Methods*. Second ed.; John Wiley & Sons, Inc.: 2001.

Appendix A

Attachment of Various Aromatic Molecules to Indium Tin Oxide Through Covalent and Non-Covalent Interactions

A.1 Introduction

In the efforts to expand upon and improve the Yang lab's hybrid method for molecular attachment to electrode surfaces, various additional aromatic molecules were attached to indium tin oxide through covalent and non-covalent interactions. The first section of this appendix describes the covalent attachment of a phosphonic acid derivative of pyrene to indium tin oxide (ITO). Phosphonic acids are commonly used for the modification of metal oxides due to their simple synthesis and robust surface attachment.[1-2] The phosphonic acid derivative of pyrene did not enable subsequent physisorption of 1-pyrenylferrocene on ITO electrodes, but it may be useful in future studies on different electrode materials, such as high surface area metal oxide electrodes.

The remainder of this appendix describes attempts to improve the strength of the π-π interaction in the Yang lab's hybrid technique for molecular attachment to electrode surfaces. The π-π interaction attachment method is robust under aqueous conditions but is unstable in solvents in which the pyrene-appended molecule is soluble due to dissolution from the surface. Pairing electron-deficient aromatics with electron-rich aromatics (such as pyrene) has been shown to improve π-π interaction strength.[3-8] For example, the strong π-π interactions between electron-rich 1,5-dialkoxynaphthalene and electron-deficient 1,4,5,8-naphthalenetetracarboxylic diimide moieties were exploited to control folding in macromolecular systems.[7] By substituting one of the pyrene molecules in the hybrid attachment system with an electron-deficient aromatic molecule, the interaction between the surface-bound aromatic and the complex-bound aromatic could be enhanced. It is hypothesized that strengthening the π-π interaction will allow for more versatile systems that can be run in any solvent, not just those in which the attached molecule is insoluble in.

A.2 Results and Discussion

A.2.1 Covalent Attachment of PyrPA to Indium Tin Oxide

Initial efforts to covalently attach pyrene to indium tin oxide (ITO) electrodes were achieved using a phosphonic acid derivative of pyrene, pyren-1-yl methyl phosphonic acid (PyrPA). PyrPA was synthesized through the hydrolysis of diethyl (pyren-1-ylmethyl)phosphonate and was characterized with NMR spectroscopies and high resolution mass spectrometry (HRMS) as described in the experimental section. PyrPA was covalently attached to the ITO surface by immersing a clean ITO sample in $(CH_3)_2SO$ solutions at 100 °C for 24 hours to yield ITO | PyrPA (Scheme A.1).

Scheme A.1. Pictorial representation of the covalent attachment of PyrPA to ITO.

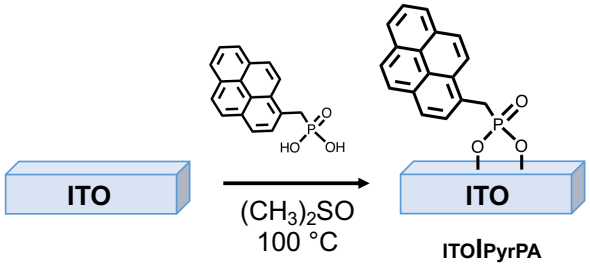

X-ray photoelectron spectroscopy (XPS) was used to characterize ITO | PyrPA. The high-resolution P 2p XPS spectrum of ITO | PyrPA displays a peak centered at 133 eV (Figure A.1, left). The component fits of the $2p_{3/2}$ and $2p_{1/2}$ peaks exhibit a 2:1 branching ratio which is expected for P 2p electrons. The effect of concentration of the PyrPA solutions used for attachment to ITO on the final surface coverage was also probed using XPS. Figure A.1 (right) plots the P/In ratio, obtained from the area of the P and In peaks in the XPS spectra, against the adsorbate concentration. Attachment of PyrPA follows a typical Langmuir isotherm model where full coverage is obtained using 1 mM PyrPA solutions. Additionally, the data confirms the lack of multilayer formation within the concentration range studied.[9-10]

Attempts to non-covalently attach 1-pyrenylferrocene to ITO|PyrPA were unsuccessful. However, PyrPA may be useful for subsequent physisorption of pyrene-appended molecules on different electrode surfaces, such as high-surface area metal oxides.

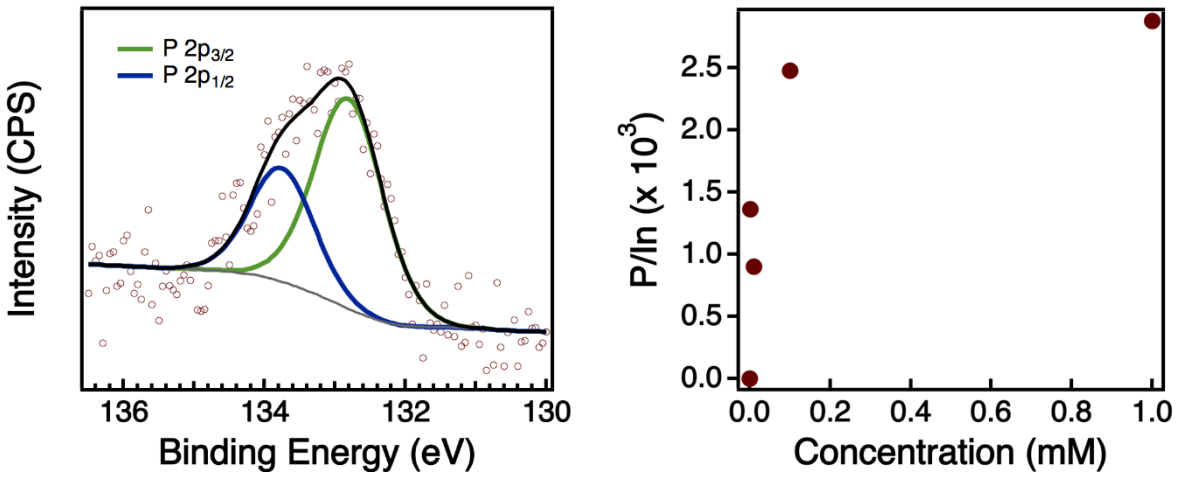

Figure A.1. P 2p XPS spectrum of ITO|PyrPA (left) and the plot of P/In ratio vs PyrPA concentration used for attachment to ITO (right).

A.2.2 Covalent Attachment of NDI to Indium Tin Oxide

N-N'-bis(2-propenyl)-1,4,5,8-napthalene tetrcarboxylic acid (NDI) is an electron-deficient aromatic molecule with vinyl groups that facilitate covalent attachment to ITO electrodes. NDI was prepared using a previously published procedure[11] and covalently attached to ITO by immersing a freshly cleaned ITO sample in a toluene solution of NDI at 65 °C for 24 hours, yielding a NDI-modified ITO electrode (Scheme A.2). It should be noted that while ITO|NDI is drawn in Scheme A.2 with a single point of surface attachment, it is possible that NDI binds in a bidentate fashion with both vinyl groups participating in attachment.

Scheme A.2. Pictorial representation of the covalent attachment of NDI to ITO.

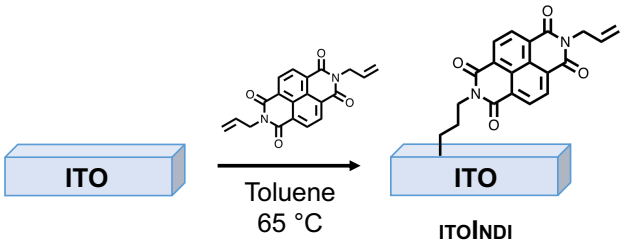

XPS was used to confirm attachment of NDI on the ITO substrate. The high-resolution N 1s XPS spectrum of ITO | NDI, shown in Figure A.2, displays a peak at 400 eV, confirming the attachment of NDI to the electrode surface. The cyclic voltammetry of ITO | NDI in aqueous conditions is displayed in Figure A.3. The first CV of ITO | NDI exhibits an irreversible oxidation at 0.26 V vs. SCE. This oxidation is no longer present in subsequent CVs. It is unclear whether this oxidation is due to breaking of the ITO-vinyl linkage, polymerization of NDI, or another cause. The oxidation at 0.26 V impedes electrochemical analysis of 1-pyrenylferrocene physisorbed to ITO | NDI through π-π interactions. Therefore, subsequent immobilization of redox-active species (e.g. catalysts) that require operation at potentials higher than 0.26 V vs SCE may not be feasible when using NDI as the surface-bound aromatic. However, NDI may still be useful for attachment of molecules that require operation at potentials less than 0.26 V vs SCE.

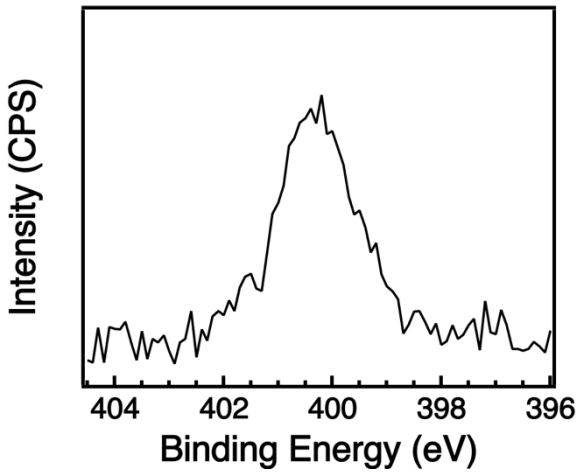

Figure A.2. N 1s XPS spectrum of ITO | NDI.

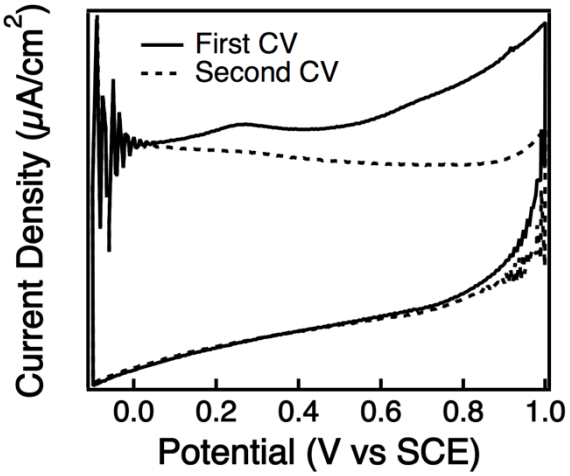

Figure A.3. Cyclic voltammograms of ITO | NDI performed in 100 mM pH 7 phosphate buffer.

A.2.3 Non-covalent Attachment of PDI to Indium Tin Oxide

Perylene diimides are extended aromatic molecules with rich electrochemical and photochemical properties.[12] The π-system of perylene diimides is electron-deficient; attachment of perylene diimides to pyrene-bound electrodes is therefore a route toward increasing the π-π interactions between the surface-bound and non-covalently physisorbed aromatic.[3] N-N'-bis(n-hexyl)-perylene-3,4:9,10-bis(dicarboximide) (PDI) was synthesized through the condensation of perylene-3,4:9,10-tetracarboxylic dianhydride with n-

hexylamine using a modified literature procedure.[13] PDI is sparingly soluble in most solvents but it is sufficiently soluble in CH_2Cl_2 and $CHCl_3$ for spectroscopic (UV-Visible, NMR) and electrochemical analysis. The ^1H NMR and UV-vis spectra of PDI (Figures A.10 and A.11) match those reported in literature.[14] The cyclic voltammetry of a saturated CH_2Cl_2 solution of PDI is shown in Figure A.4 (left). At slow scan rates (< 0.5 V/s), two distinct quasi-reversible reduction events are observed, corresponding to the reduction of PDI to its radical anion and dianion. At faster scan rates, the two redox features overlap with one another. Figure A.4 (right) displays the peak current vs square root of scan rate for scan rates at which the two redox events are distinguishable from one another. Peak current varies linearly with the square root of scan rate, indicating a diffusion-limited electrochemical process.

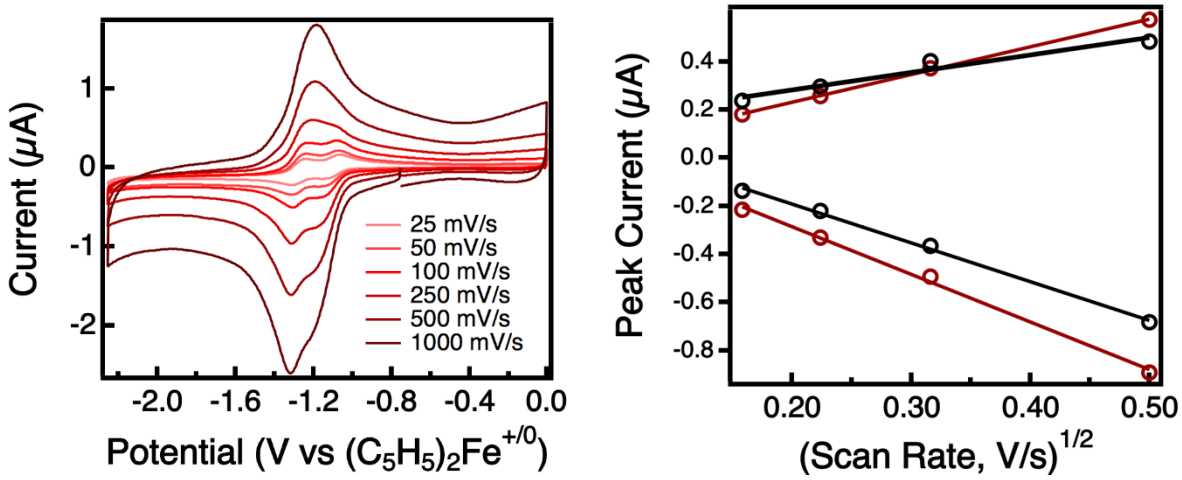

Figure A.4. Variable scan rate cyclic voltammetry of saturated PDI performed in 100 mM $TBAPF_6$ in CH_2Cl_2 (left) and the corresponding peak current vs square root of scan rate plot for scan rates at which the two redox events are distinguishable from one another (right).

Scheme A.3. Pictorial representation of the non-covalent attachment of PDI to ITO | Pyr.

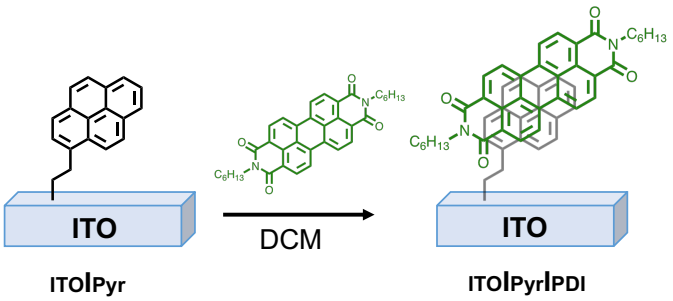

PDI was physisorbed to ITO | Pyr by soaking ITO | Pyr samples in saturated solutions of PDI for 12 h followed by rinsing with CH_3CN to remove loosely bound species (Scheme A.3). The cyclic voltammetry of ITO | Pyr | PDI is displayed in Figure A.5 (left). The voltammograms display a reversible reduction event at –0.76 V vs SCE. Peak current varies linearly with scan rate, confirming a surface-bound electrochemical process. Cyclic voltammetry of ITO | Pyr | PDI was also performed in acetonitrile (Figure A.6). The first cycle exhibits a large reduction feature followed by two small oxidation features. The second cycle displays a small reduction feature but lacks oxidation events and subsequent cycles are free of any faradaic features. These results indicate loss of PDI from the surface due to dissolution into the electrolyte solution. The loss of PDI from the surface in CH_3CN solution suggests that the strength of the π-π interaction between the surface-bound pyrene and PDI is not strong enough to overcome dissolution. However, the strength of the pyrene-PDI interaction may be stronger than that of a pyrene-pyrene interaction.

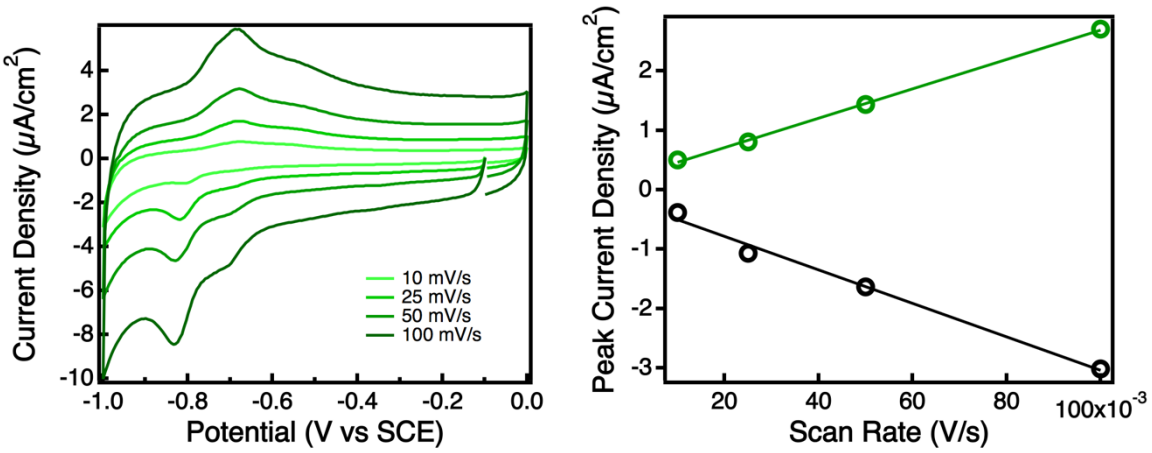

Figure A.5. Variable scan rate cyclic voltammetry of ITO | Pyr | PDI performed in 100 mM pH 7 HEPES buffer with 100 mM KCl as the supporting electrolyte (left) and the corresponding peak current vs scan rate plot (right).

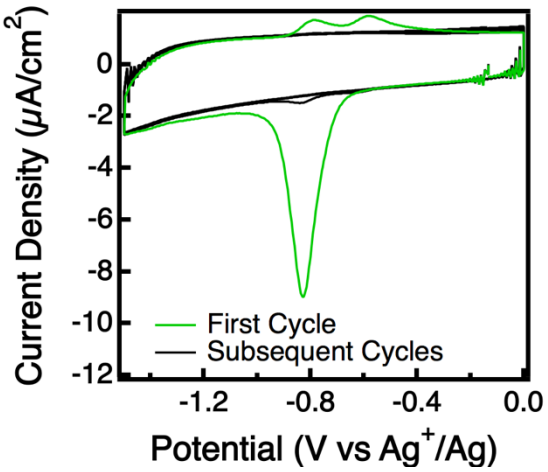

Figure A.6. Consecutive cyclic voltammograms of ITO | Pyr | PDI performed in 100 mM $TBAPF_6$ in CH_3CN.

A.3 Conclusions

PyrPA was covalently attached to ITO as confirmed by XPS. Subsequent attachment of 1-pyrenylferrocene to ITO | PyrPA was unsuccessful but PyrPA may be useful on other electrode surface. Electron-deficient aromatic molecules, NDI and PDI, were covalently and non-covalently attached to ITO in order to improve the strength of the π-π interaction on the electrode surface. NDI was covalently attached to ITO and characterized *via* XPS. However,

an irreversible oxidation in the CV of ITO|NDI prevents electrochemical analysis of 1-pyrenylferrocene on the ITO|NDI surface. PDI was therefore non-covalently attached to ITO|Pyr. CVs of ITO|Pyr|PDI in water display a reversible reduction event at –0.76 V vs SCE. However, CVs in CH_3CN indicate the loss of PDI from the surface due to dissolution of PDI into the electrolyte solution.

A.4 Experimental

General Procedures

All reactions and manipulations were performed under an atmosphere of N_2 unless otherwise specified. Solvents were degassed by sparging with argon. Non-aqueous solvents were dried by passing through columns of neutral alumina or molecular sieves in an inert atmosphere. ITO on boro-aluminosilicate glass with a thickness of 0.5 mm and a sheet resistance of 5–15 Ω/sq was purchased from Delta Technologies. Diethyl (pyren-1-ylmethyl)phosphonate,[15] and N-N'-bis(2-propenyl)-1,4,5,8-napthalene tetrcarboxylic diimide (NDI)[11] were prepared using previously published procedures. All other materials and reagents were purchased from commercial suppliers and used without purification (Aldrich and Fisher).

Physical Methods

X-ray photoelectron spectra were acquired with a Kratos Analytical AXIS Supra spectrometer utilizing monochromatic Al Kα radiation (1486.7 eV, 250 W) under ultra-high vacuum (UHV) conditions (~10–9 Torr). The binding energies were referred to the C 1s signal at 285 eV. Spectral data was analyzed using Computer Aided Surface Analysis for X-ray Photoelectron Spectroscopy (CasaXPS). Shirley or linear backgrounds and Gaussian-

Lorentzian lineshapes were used to model peaks. UV-Visible spectra were collected in using an Agilent Technologies Cary 60 UV−Vis spectrophorometer.

Electrochemical Experiments

Three-electrode cyclic voltammetry experiments were performed with a Pine Wavedriver 10 potentiostat and Aftermath software (Version 1.4.7881). Experiments were performed in 100 mM electrolyte solutions using the electrolyte and solvent specified in the main text. Solution-phase experiments were performed using a 1 mm diameter glassy carbon disk working electrode. A glassy carbon rod was used as the counter electrode in all electrochemical experiments. Aqueous potentials are referenced to SCE and non-aqueous potentials are referenced to $Fe(C_5H_5)_2^{+/0}$. All reported peak current densities are corrected for capacitive currents using the Regression baseline mode in Aftermath software.

Substrate Modification

ITO electrodes were cleaned by immersing samples in a series of solvents at 50 °C for 10 minutes each. The order of solvents was as follows: trichloroethylene, acetone, and methanol. The electrodes were rinsed with H_2O and dried under a stream of air after each solvent. Electrodes were functionalized immediately after cleaning. Clean ITO samples were functionalized with PyrPA by immersing the sample in a 1 mM solution of PyrPA in $(CH_3)_2SO$ and heating at 100 °C for 24 h. The samples were removed from the vial and rinsed with $(CH_3)_2SO$ to yield PyrPA-modified ITO (ITO|PyrPA). Clean ITO samples were functionalized with NDI by immersing the sample in a 1 mM solution of NDI in toluene and heating at 65 °C for 24 h. The samples were removed from the vial and rinsed with toluene to yield NDI-modified ITO (ITO|NDI). ITO|Pyr samples were functionalized with PDI by immersing the

sample in a saturated solution of PDI in CH_2Cl_2 for 12 h. The samples were removed from the vial and rinsed with CH_3CN to yield PDI-modified ITO|Pyr (ITO | Pyr | PDI).

Synthesis

Synthesis of pyren-1-yl methyl phosphonic acid (PyrPA). Diethyl (pyren-1-ylmethyl)phosphonate (216 mg, 0.613 mmol) was dissolved in 15 mL dioxane. Excess concentrated HCl (882 mg, 24.2 mmol) was added and the solution was stirred at 100° C for 24 h. The reaction mixture was cooled to 0° C and H_2O was added until a precipitate formed. The solid was removed from the filtrate to give a pure, light brown powder (146 mg, 0.492 mmol, 80% yield). ^{1}H NMR (500 MHz, DMSO-d_6): δ = 8.40–7.98 (m, 9H, Pyr-H), 3.77 (s, 1H, CH_{2a}), 3.72 (s, 1H, CH_{2b}), 3.48 (b, OH). ^{13}P NMR (400 MHz, DMSO-d_6): δ = 21.77. ^{13}C NMR (500 MHz, DMSO-d_6): δ = 130.89, 130.45, 129.41, 129.22, 128.84, 127.43, 126.80, 126.15, 124.92, 124.83, 124.74, 124.65, 124.20, 124.18, 33.60, 32.56. HR-MS: m/z calc. for $[C_{17}H_{13}PO_3]$H-: 295.0524; found: 295.0525.

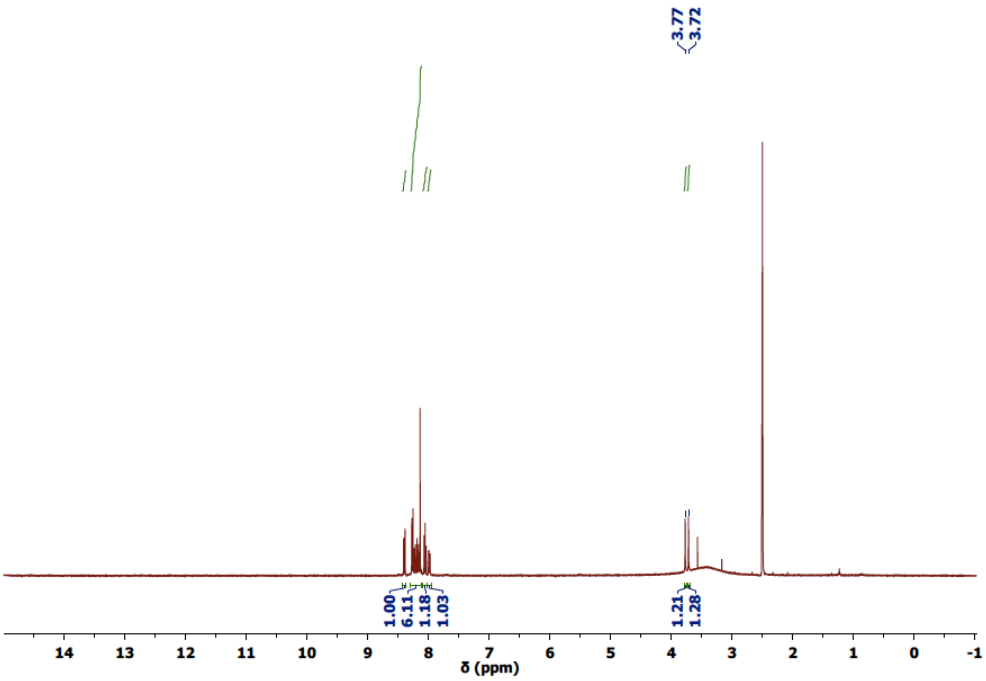

Figure A.7. ^{1}H NMR of PyrPA in DMSO-d_6

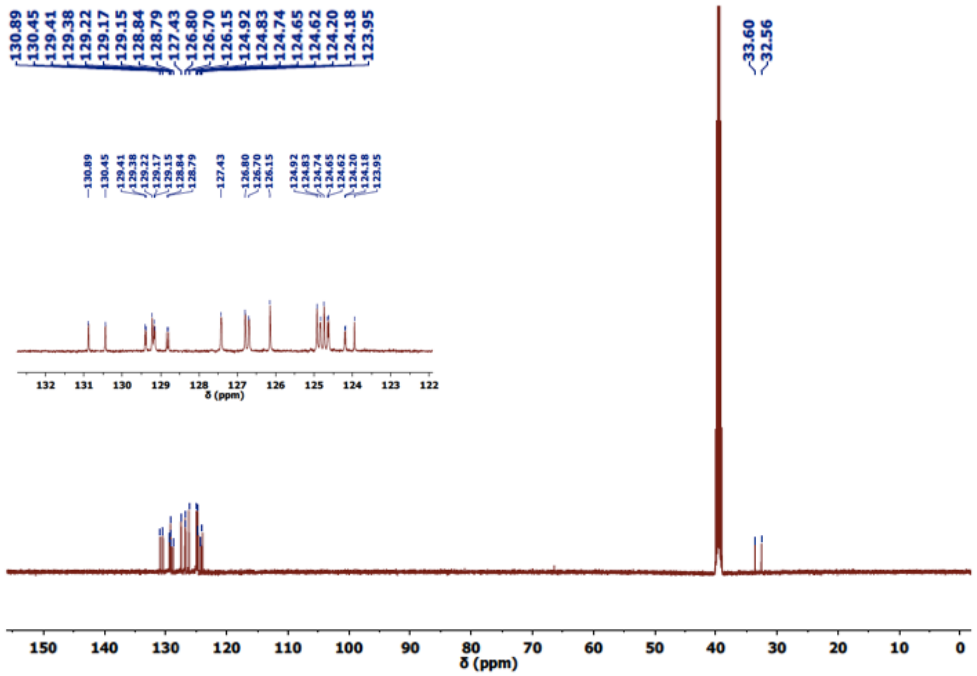

Figure A.8. $^{13}C\{^{1}H\}$ NMR of PyrPA in DMSO-d_6

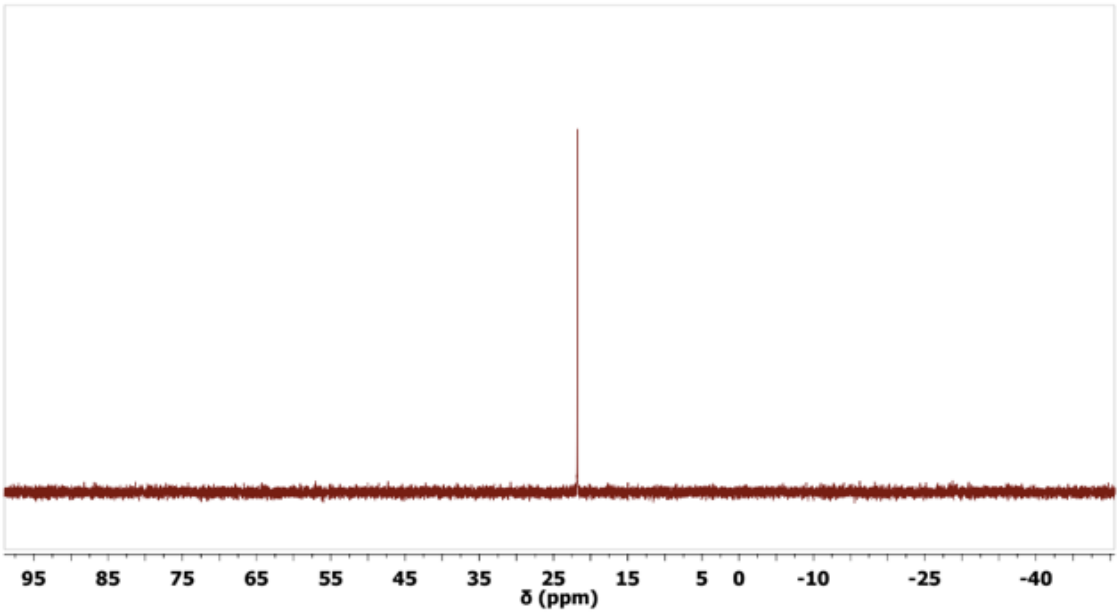

Figure A.9. $^{31}P\{^{1}H\}$ NMR of PyrPA in DMSO-d_6

Synthesis of N-N'-bis(n-hexyl)-perylene-3,4:9,10-bis(dicarboximide) (PDI). Perylene-3,4:9,10-tetracarboxylic dianhydride (363 mg, 0.926 mmol), n-hexylamine (0.25 mL, 1.9 mmol), and imidazole (384 mg, 5.63 mmol) were added to a Schlenk flask with 20 mL anhydrous toluene. After refluxing under N_2 for 16 h, the reaction was cooled to room temperature followed by addition of 20 mL ethanol and 10 mL of 1 mM HCl. The mixture was stirred for 4 h during which time a dark purple precipitate formed. The precipitate was isolated via vacuum filtration, rinsed with ethanol, and dried under vacuum to yield the dark purple, pure product (462 mg, 87% yield). ^{1}H NMR (500 MHz, $CDCl_3$): δ = 8.71 (d, 4H, Ph), 8;65 (4, 4H, Ph), 4.21 (m, 4H, -N-CH_2), 1.76 (m, 4H, -CH_2-), 1.46 (m, 4H, -CH_2-), 1.36 (m, 4H, -CH_2-), 0.91 (m, 6H, -CH_3). UV-visible (CH_2Cl_2): λ_{max} = 524 nm, 488 nm, 457 nm.

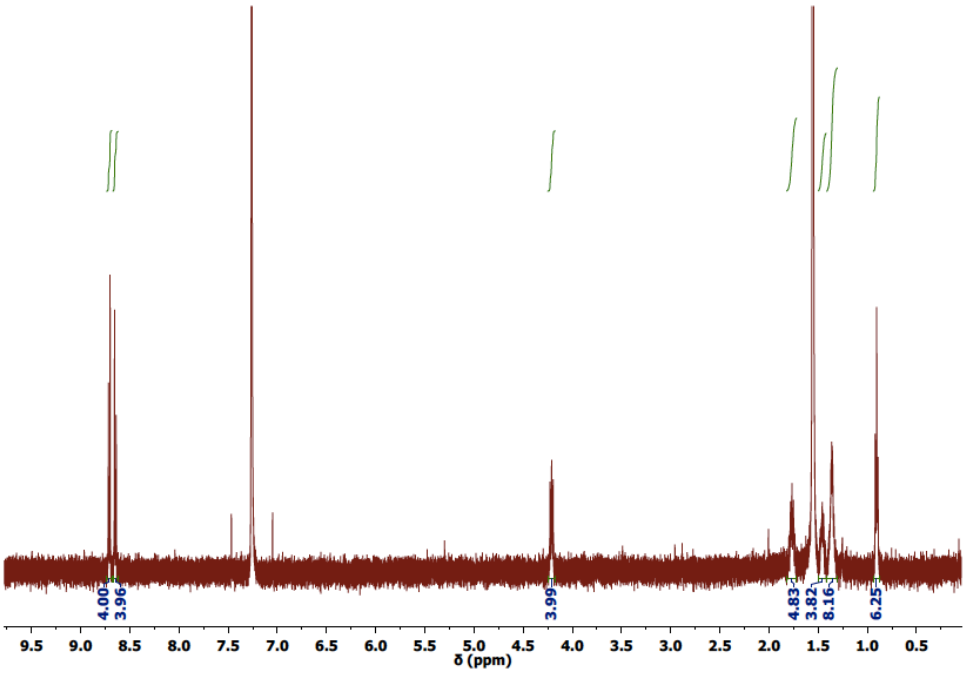

Figure A.10. ^{1}H NMR of PDI in $CDCl_3$.

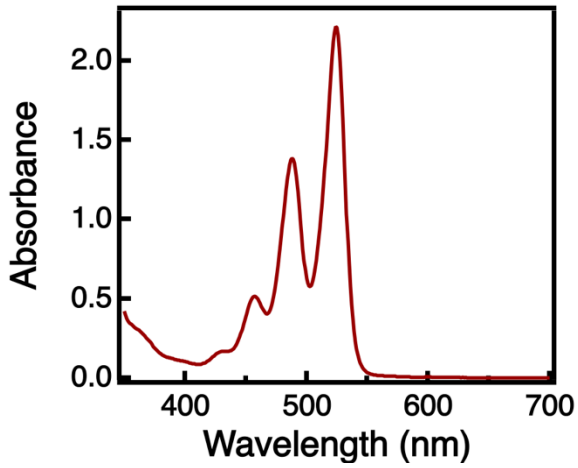

Figure A.11. UV-visible absorption spectrum of saturated PDI in CH_2Cl_2.

A.5 References

1. Hotchkiss, P. J.; Jones, S. C.; Paniagua, S. A.; Sharma, A.; Kippelen, B.; Armstrong, N. R.; Marder, S. R., The Modification of Indium Tin Oxide with Phosphonic Acids: Mechanism of

Binding, Tuning of Surface Properties, and Potential for Use in Organic Electronic Applications. *Acc. Chem. Res.* **2012,** *45*, 337-346.

2. Pujari, S. P.; Scheres, L.; Marcelis, A. T. M.; Zuilhof, H., Covalent Surface Modification of Oxide Surfaces. *Angew. Chem. Int. Ed.* **2014,** *53*, 6322-6356.

3. Martinez, C. R.; Iverson, B. L., Rethinking the term "pi-stacking". *Chem. Sci.* **2012,** *3*, 2191-2201.

4. Williams, J. H.; Cockcroft, J. K.; Fitch, A. N., Structure of the Lowest Temperature Phase of the Solid Benzene–Hexafluorobenzene Adduct. *Angewandte Chemie International Edition in English* **1992,** *31*, 1655-1657.

5. Claessens, C. G.; Stoddart, J. F., π–π INTERACTIONS IN SELF-ASSEMBLY. *Journal of Physical Organic Chemistry* **1997,** *10*, 254-272.

6. Petitjean, A.; Cuccia, L. A.; Schmutz, M.; Lehn, J.-M., Naphthyridine-Based Helical Foldamers and Macrocycles: Synthesis, Cation Binding, and Supramolecular Assemblies. *J. Org. Chem.* **2008,** *73*, 2481-2495.

7. Reczek, J. J.; Villazor, K. R.; Lynch, V.; Swager, T. M.; Iverson, B. L., Tunable Columnar Mesophases Utilizing C2 Symmetric Aromatic Donor−Acceptor Complexes. *J. Am. Chem. Soc.* **2006,** *128*, 7995-8002.

8. Reczek, J. J.; Iverson, B. L., Using Aromatic Donor Acceptor Interactions to Affect Macromolecular Assembly. *Macromolecules* **2006,** *39*, 5601-5603.

9. Paniagua, S. A.; Hotchkiss, P. J.; Jones, S. C.; Marder, S. R.; Mudalige, A.; Marrikar, F. S.; Pemberton, J. E.; Armstrong, N. R., Phosphonic Acid Modification of Indium−Tin Oxide Electrodes: Combined XPS/UPS/Contact Angle Studies. *J. Phys. Chem. C* **2008,** *112*, 7809-7817.

10. Paniagua, S. A.; Li, E. L.; Marder, S. R., Adsorption studies of a phosphonic acid on ITO: film coverage, purity, and induced electronic structure changes. *Phys. Chem. Chem. Phys.* **2014,** *16*, 2874-2881.

11. Sotiriou-Leventis, C.; Mao, Z.; Rawashdeh, A.-M. M., A Convenient Synthesis and Spectroscopic Characterization of N,N'-Bis(2-propenyl)-2,7-diazapyrenium Quaternary Salts. *J. Org. Chem.* **2000,** *65*, 6017-6023.

12. Lee, S. K.; Zu, Y.; Herrmann, A.; Geerts, Y.; Müllen, K.; Bard, A. J., Electrochemistry, Spectroscopy and Electrogenerated Chemiluminescence of Perylene, Terrylene, and Quaterrylene Diimides in Aprotic Solution. *J. Am. Chem. Soc.* **1999,** *121*, 3513-3520.

13. Jones, B. A.; Facchetti, A.; Wasielewski, M. R.; Marks, T. J., Tuning Orbital Energetics in Arylene Diimide Semiconductors. Materials Design for Ambient Stability of n-Type Charge Transport. *J. Am. Chem. Soc.* **2007,** *129*, 15259-15278.

14. Baumgartner, B.; Svirkova, A.; Bintinger, J.; Hametner, C.; Marchetti-Deschmann, M.; Unterlass, M. M., Green and highly efficient synthesis of perylene and naphthalene bisimides in nothing but water. *Chem. Comm.* **2017,** *53*, 1229-1232.

15. Matsunaga, Y.; Takechi, K.; Akasaka, T.; Ramesh, A. R.; James, P. V.; Thomas, K. G.; Kamat, P. V., Excited-State and Photoelectrochemical Behavior of Pyrene-Linked Phenyleneethynylene Oligomer. *J. Phys. Chem. B* **2008,** *112*, 14539-14547.